RHO PRIME ELECTROPRODUCTION AT HERA

STUART PETER COCKS

Ph. D. 1998

Rho Prime Electroproduction at HERA

Thesis submitted in accordance with the requirements of the University of Liverpool for the degree of Doctor of Philosophy

by

Stuart Peter Cocks

September 1998

Oliver Lodge Laboratory
University of Liverpool

Rho Prime Electroproduction at HERA

Stuart Peter Cocks

Abstract

Measurements on ρ' and ρ electroproduction are presented using data collected by the H1 experiment at HERA. The data were taken during 1994 and correspond to an integrated luminosity of $\sim 2\,\mathrm{pb}^{-1}$. The observed properties of the resonance signals are as expected for vector meson electroproduction. The ratio of the ρ' cross-section to the ρ cross-section is presented at an average Q^2 of 11 GeV^2. It is found to be significantly larger than that measured in photoproduction and at very low Q^2. The ratio is in agreement with QCD based calculations.

Contents

The Author's Contribution

The contribution of the author to the work presented in this thesis comprises the selection of diffractive events, including the study of noise in the forward muon system and proton remnant tagger and the efficiency and purity of the selection, the study of hadronic selection criteria and the definition of 2 and 4 track event samples and the study of the properties of the ρ' and ρ events identified in these samples. In addition, the author helped in the running of the forward tracker, conducted Monte Carlo studies as part of the design team for the Very Low Q^2 Calorimeter and was librarian for the H1 event display software.

Acknowledgments

First and foremost I would like to thank my supervisor, Tim Greenshaw, who has never failed to be helpful, encouraging and knowledgeable throughout my PhD. I could not have had a better supervisor.

Thanks must also go to Erwin Gabathuler for allowing me to pursue this research and for always keeping a keen interest in my work.

I must also thank the H1 diffractive group for providing such a fruitful working environment. In particular I must thank John Dainton for lots of help and encouragement and Andy Mehta and Julian Phillips for their utmost competence and lots of guidance and answers on diffractive physics. I must also thank Pierre Marage and Barbara Clerbaux for their insight into vector meson production.

The work for this thesis would not have been possible without the financial support of the Particle Physics and Astronomy Research Council and the hospitality of the DESY laboratory.

Thanks also to all the Liverpool H1 group and everyone else I have had the pleasure to work and/or share an office with in Hamburg and Liverpool. In particular Pete Sanders, Roly Martin, Dave Milstead, Chris Cormack, Theo Holtom and Mark Smith.

Thank also to the other fellow students in my year at Liverpool - Hugh Tallini, Angela Benelli, Julia Cowell and Chris Green.

I must thank all the people who made my stay in Hamburg so enjoyable. In particular Molly Anderson, Rob Waugh, Kirstie Hewitt, Paul Sutton, Paul Thompson, Chris Hilton, Ben Waugh, Brian Cox, Lee and Rachel West and Bianca Luta.

I would also like to thank the people in Liverpool for making writing up less depressing and daunting than it otherwise would have been. In particular Roger Allatt, Dominic Duxbury, Ali Sheridan, Alex Keenan and anyone else I've had the pleasure of playing football and cricket (badly) with.

Finally I would like to thank my family for all the support they have always given me.

Chapter 1

Introduction

The majority (>99 %) of hadron-hadron interactions involve very low momentum transfers and cannot be described using perturbative quantum chromo-dynamics (QCD). These interactions are often referred to as diffractive, as the distribution of scattering angles is reminiscent of that seen when coherent light is scattered off an absorbent disc of dimensions similar to that of the wavelength of the light. Diffractive processes have been described phenomenologically within Regge theory, using the exchange of a vacuum state termed the pomeron. The relationship of the pomeron to QCD has, until recently, been somewhat mysterious. It has been speculated that the pomeron, which must have the quantum numbers of the vacuum, could be formed from two gluons.

Recently, studies of events in which there is a large rapidity gap at the HERA *ep* collider at DESY in Hamburg, Germany have led to a deepening of our understanding of diffraction. It has been shown in inclusive cross-section measurements that most of the pomeron's momentum is indeed carried by gluons. Measurements of the event shape and energy flow in the final state of rapidity gap events have confirmed this observation. In this thesis, the evidence leading to the conclusion that the pomeron is largely composed of gluons is discussed. This is followed by a description of a study of a particular diffractive final state for which there exist models based upon perturbative QCD. This study confirms the picture of the pomeron as a gluon dominated object and shows how QCD calculations are becoming useful in the description of some aspects of diffraction.

Exclusive vector meson production of heavy mesons has provided a useful test

of the available diffractive QCD models. HERA results on the photoproduction of J/ψ mesons at high energy have been shown to be incompatible with Regge theory predictions and have shown good agreement with QCD models based upon 2 gluon exchange. The HERA collider has reached values of the momentum squared of the virtual photon, Q^2, in ep collisions such that predictions of some properties of light vector meson electroproduction are possible within the framework of QCD. Several models, described in this thesis, have shown good agreement with the limited light meson electroproduction results available thus far. They also make interesting predictions for the characteristics of the excited states of the light mesons. HERA results on light meson excitations will provide a further test of these models.

This thesis presents the characteristics of ρ' and ρ events and a measurement of the ρ' to ρ cross-section ratio in 1994 H1 electroproduction data. The implications for the available QCD models and the future potential of HERA for such measurements are discussed.

Chapter 2

Theory

This chapter gives an overview of the theory relevant to the study of high Q^2 vector meson production. Firstly, Deep-Inelastic Scattering (DIS) is discussed. Secondly, a discussion of the diffractive interpretation of large rapidity gap events at HERA is presented. Following this, diffractive vector meson production is discussed in more detail, as are existing Regge and QCD inspired models of vector meson production and their application to data. The current understanding of the ρ' resonance follows. The chapter is concluded by a discussion of the Monte Carlo generator used in the analysis.

2.1 Deep Inelastic Scattering

The main purpose of the HERA collider is to study the structure of the proton using the point-like electron to probe the extended proton. The leptonic initial state provides a "clean" probe, ensuring that the final state is simpler to interpret than that in hadron-hadron scattering.

Figure 2.1 shows a schematic view of a DIS event. The following discussion follows a similar line to that in [1]. A beam lepton with momentum k interacts with a quark from the proton with momentum p via the exchange of a virtual boson. In Neutral Current (NC) DIS the exchanged boson is a virtual photon or Z^0 boson. In the case of Charged Current (CC) scattering, the exchanged boson is a $W^{\pm}$ and the scattered lepton is a neutrino.

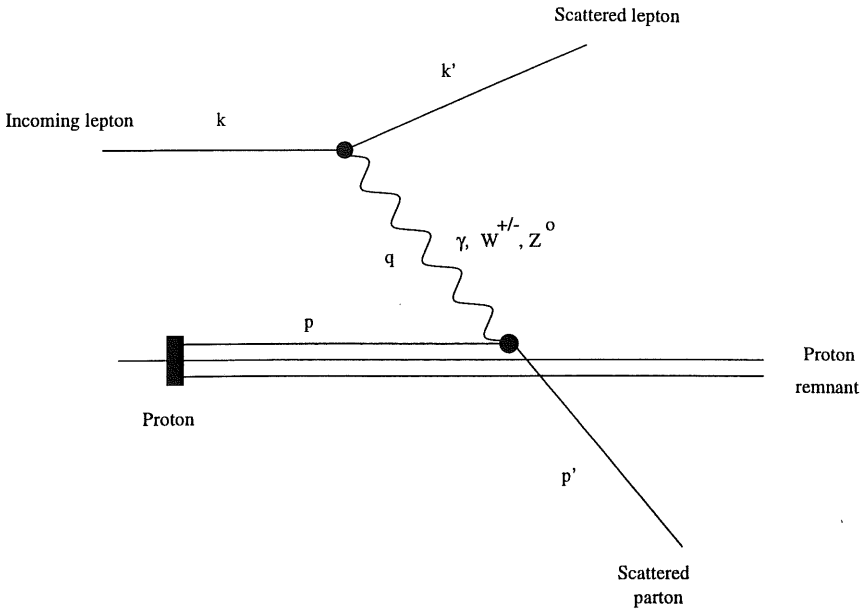

Figure 2.1: A schematic picture of a DIS event showing the kinematic variables used to describe the scattering process.

The kinematics of DIS events are described by the Lorentz invariant quantities Q^2, x, W^2 and y. Q^2 is the negative square of the 4-momentum of the exchanged boson:

$$Q^2 = -q^2 = -(k - k')^2 \tag{2.1}$$

and determines the transverse size resolved by the virtual boson. The Bjorken scaling variable, x, is defined by

$$x = \frac{Q^2}{2P \cdot q}, \tag{2.2}$$

where P is the incident proton's 4-momentum. In the frame in which the proton has infinite momentum, x can be considered to be the fraction of the proton's momentum carried by the struck parton. The variable y is defined by

$$y = \frac{P \cdot q}{P \cdot k}, \tag{2.3}$$

which is the fractional energy loss of the incoming lepton in the rest frame of the proton. Finally, W^2 is the invariant mass squared of the hadronic final state:

$$W^2 = (q + P)^2. \tag{2.4}$$

Only two of these variables are independent. They are related by:

$$Q^2 = sxy, \tag{2.5}$$

$$W^2 = Q^2(\frac{1}{x} - 1). \tag{2.6}$$

Here, s is the squared total centre-of-mass energy of the ep collision.

2.2 Structure of the Proton

The total neutral current DIS cross-section can be expressed in terms of three structure functions, $F_1(x, Q^2)$, $F_2(x, Q^2)$ and $F_3(x, Q^2)$.

$$\frac{d^2\sigma_{ep\to eX}}{dx\,dQ^2} = \frac{4\pi\alpha_{em}^2}{xQ^4}\Big[y^2xF_1(x,Q^2) + (1-y)F_2(x,Q^2) \pm (y - \frac{y^2}{2})xF_3(x,Q^2)\Big]. \tag{2.7}$$

Here the upper signs refer to electron-proton and the lower to positron-proton scattering. The structure functions describe the structure of the proton. The parity violating term, $F_3(x, Q^2)$, which arises due to Z^0 exchange, is negligible for the kinematic range considered here, namely $Q^2 \ll M_Z^2$ and it can be assumed that only photon exchange is present.

In this approximation, the cross-section can be written

$$\frac{d^2\sigma_{ep\to eX}}{dx\,dQ^2} = \frac{4\pi\alpha_{em}^2}{xQ^4}\Big[(1 - y + \frac{y^2}{2})F_2(x,Q^2) - \frac{y^2}{2}F_L(x,Q^2)\Big], \tag{2.8}$$

where $F_L(x, Q^2) = F_2(x, Q^2) - 2xF_1(x, Q^2)$ is related to the cross-section for the scattering of longitudinally polarised photons from the quarks, the cross-section for the scattering of transversely polarised photons being given by $F_2(x, Q^2)$. Defining the ratio of the longitudinal to the transverse photon scattering cross-sections to be $R(x, Q^2) = \frac{F_L(x,Q^2)}{F_2(x,Q^2) - F_L(x,Q^2)}$, equation 2.8 becomes

$$\frac{d^2\sigma_{ep\to eX}}{dxdQ^2} = \frac{4\pi\alpha_{em}^2}{xQ^4}\Big(1 - y + \frac{y^2}{2(1 + R(x,Q^2))}\Big)F_2(x,Q^2). \tag{2.9}$$

In the *quark-parton model* (QPM) [2] [3] the proton consists of non-interacting point-like particles. If these *partons* have spin $\frac{1}{2}$ (in units of $\hbar$), the contribution to the cross-section from longitudinally polarised photons is zero and the Callan-Gross [4] relation is obtained:

$$2xF_1(x, Q^2) = F_2(x, Q^2). \tag{2.10}$$

The experimental verification of this relationship confirmed the existence of the spin-$\frac{1}{2}$ partons, the *quarks*. In addition, the QPM relates the structure function $F_2(x, Q^2)$ directly to the momentum distribution of the quarks in the nucleon:

$$F_2(x) = \Sigma e_i^2 x q_i(x),$$

where e_i is the charge of the quark and $q_i(x)\,dx$ the number of quarks of flavour i carrying a fraction of the proton's momentum between x and $x+dx$. Note that F_2 is now dependent only on x, not on Q^2. This is referred to as *Bjorken scaling* [5] and was found to hold in early *ep* experiments [6], providing justification for the QPM. However, from the experimentally measured proton and neutron structure functions it was shown that quarks only account for around half of the momentum of the proton [7]. The rest of the proton's momentum must be carried by neutral partons which do not couple to the photon. Another failing of the QPM is its inability to describe the observation of *scaling violations*, the Q^2 dependence of F_2.

The theory of *quantum chromodynamics* was developed in the 1970s. This provided a solution to the problems of the simple QPM. In QCD, the strong force between quarks is carried by electrically neutral vector bosons called gluons. These account for the missing momentum of the proton and also explain scaling violations. Valence quarks in the proton can radiate gluons which in turn can split into quark-antiquark pairs and gluon-gluon pairs. As Q^2 increases, smaller and smaller distance scales can be probed in the proton. Thus, at large Q^2, a large number of small-x partons are seen resulting in an increase of F_2 with Q^2 at low x. At large x, the valence quarks lose momentum by radiating gluons resulting in a decrease in F_2 with Q^2.

The strong coupling constant, α_s, which describes the strength of the interaction between the colour charged quarks and gluons, is dependent on the momentum scale. At high momentum transfer (high Q^2 in DIS) α_s is small and the interaction is relatively weak. This behaviour is known as "asymptotic freedom" and explains the success of the QPM in the high Q^2 limit. At low momentum transfers, α_s becomes much larger and the quarks and gluons interact very strongly. This results in quark *confinement*; free quarks are never seen. For example, as the quark struck in DIS and those in the proton remnant separate, there comes a point at which it is energetically favourable to create a new quark-antiquark pair, rather than increase the energy stored in the field between the

quark and the proton remnant. Hence, the space between the struck quark and the proton remnant is filled with new quark-antiquark pairs which combine to form hadrons (largely mesons).

If the relevant momentum scale is large enough then $\alpha_s \ll 1$ and accurate predictions can be made in QCD using perturbation theory. If no "hard scale" is present, phenomenological methods are used. The Q^2 evolution of F_2 can be well described in QCD by the Dokshitzer, Gribov, Lipatov, Altarelli and Parisi (DGLAP) [8] [9] evolution equations.

$F_2(x, Q^2)$ has been measured at HERA at much higher Q^2 and smaller x than was possible at fixed target experiments [10]. At fixed Q^2, F_2 is found to increase steeply with decreasing x. A natural explanation of this is an increasing gluon density at low x [10].

2.3 Photoproduction

From equation 2.9 it can be seen that the total differential ep cross-section has a $1/Q^4$ dependence. This cross-section is therefore dominated by interactions at very low Q^2. In the limit in which $Q^2 \approxeq 0$ the electron is scattered through very small angles and the interaction can be thought of as occurring between a "quasi-real" photon, emitted from the electron, and the proton. This process is known as *photoproduction.* In this way HERA can be used as a high energy γp collider. The flux of photons produced by the electron can be calculated [11] [12], enabling the conversion of ep cross-sections into γp cross-sections for comparison to theory and previous measurements.

If the transverse momentum squared of the parton entering a γp collision from the proton side is large enough, much larger than Q^2, the hadronic structure of the photon can be probed in a way analogous to the proton structure being probed in DIS. Here the photon can be considered as fluctuating into a quark-antiquark pair before interacting with the proton. Gluons can be exchanged between this pair, leading to the formation of an object with hadronic structure. This object typically behaves like a meson with the quantum numbers of the photon, i.e. a vector meson such as the ρ, ω or ϕ. This is referred to as vector meson dominance (VMD). These photons with hadronic structure undergo what are termed *resolved*

photon interactions, in contrast to *direct photon* interactions, in which the photon acts as a point-like object. Photon structure measurements for both quasi-real and low Q^2 virtual photons have been made at HERA [13].

Because of the lack of a hard scale from the exchanged photon, the majority of photoproduction events are *soft* and perturbative QCD calculations are not possible. However, if the transverse momentum of the outgoing partons is sufficient, this provides a hard scale for QCD calculations. A hard scale can also be provided by the mass of the charm quark in J/ψ photoproduction. The photoproduction of vector mesons is covered in more detail later in this thesis.

2.4 Diffractive Scattering

The term diffractive scattering was coined to describe the dominant part of the cross-section for hadron-hadron scattering. For example, if pp scattering is studied, the vast majority of interactions are found to involve very small momentum transfer squared $|t|$. Indeed about a quarter of these are elastic, i.e. leave the protons intact, $pp \rightarrow pp$. The angular distribution of the outgoing protons is reminiscent of the diffraction pattern obtained when a coherent light beam hits a black disc of radius about that of the wavelength of the light. This pattern persists even if either or both of the protons break up (dissociate) during the collision, provided the invariant mass of the hadronic systems produced remains much smaller then the total centre-of-mass energy of the collision, $\sqrt{s}$. Diffraction in hadron-hadron collisions has been successfully parameterised within the framework of Regge theory [14] in terms of the exchange of a colourless object termed the *pomeron*, $I\!P$.

As described in the previous section, photons can interact as though they have hadronic structure. It is, therefore, not surprising that many photoproduction interactions show properties similar to the diffractive interactions observed in hadron-hadron collisions [15]. The photon in such interactions often emerges as a meson with the quantum numbers of a photon, most commonly a ρ, ω or ϕ meson. The diffractive interaction can then be thought of as being the splitting of the photon into a quark-antiquark pair which develops into a vector meson and then scatters off the proton. This process is referred to as elastic scattering. As in hadron-hadron scattering, the proton and meson may dissociate in the scattering,

but the process is still termed diffractive if the masses of the resulting hadronic systems are much smaller than $\sqrt{s}$. This means that there is a large region in rapidity between the outgoing hadronic systems which contains no hadrons, referred to as a *rapidity gap*.

Early in HERA's operation, large rapidity gaps were also observed in a surprisingly high proportion of DIS events [16, 17]. It was suggested that these were due to the exchange of a colourless object in the interaction, as illustrated in figure 2.3. In terms of the picture in which the hadrons between the struck quark and the proton remnant are generated by the formation of quark-antiquark pairs using the energy in the colour field, the rapidity gap occurs because there is no colour force between objects which do not have colour charge. The hypothesis was made that the exchanged colourless object is the pomeron. In order to explain the concept of the pomeron in a little more detail, a brief introduction to Regge theory is necessary. This is followed below by a description of measurements of rapidity gap events in DIS which demonstrate that they can indeed be associated with pomeron exchange.

2.4.1 Regge Theory

Regge theory is a phenomenological model successful in describing many aspects of hadron-hadron interactions. Scattering processes are considered to occur via the exchange of virtual bound state hadrons, referred to in the model as *Regge poles* or *Reggeons*. To provide a good description of hadronic scattering amplitudes, all possible exchanges have to be taken into account. It was found from pion scattering on hydrogen targets that the resonances produced fall into patterns. When plotting the square of the mass of a resonance against its spin, resonances with otherwise identical quantum numbers fall approximately on straight lines, called *Regge trajectories*.

Regge theory is used to sum up the contributions from the exchange of mesons lying on the same trajectory. Regge theory relates the production of a resonance in the s-channel to the exchange of the resonance in the t-channel. Figure 2.2 shows, a) the production of an unstable ρ resonance, and b) the exchange of a Regge trajectory $\alpha(t)$ in the t channel.

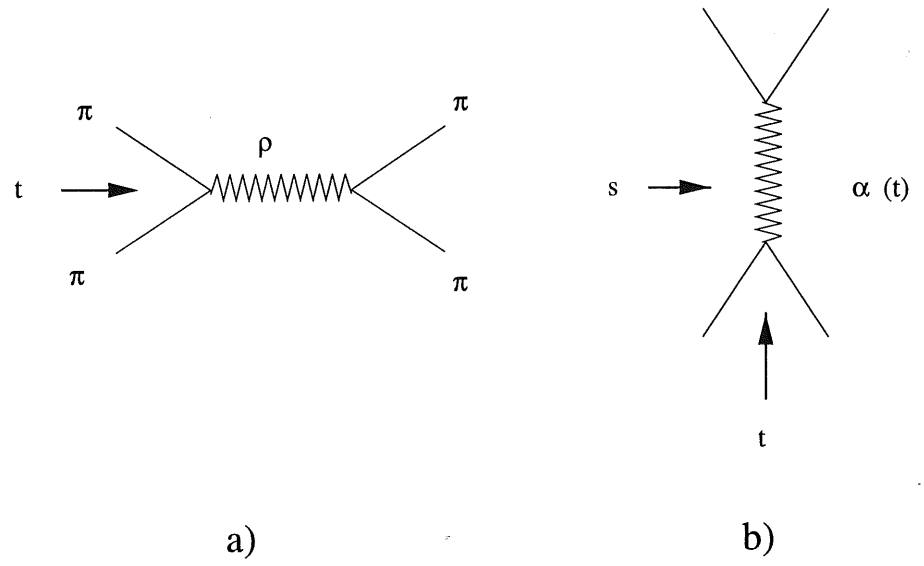

Figure 2.2: a) The s channel diagram for $\pi\pi \rightarrow \pi\pi$ scattering with the resonant production of a ρ meson. b) The same scattering process proceeding via the t channel exchange of a ρ meson.

The straight line describing a Regge trajectory is represented by [14]:

$$\alpha(t) = \alpha_0 + \alpha' t, \tag{2.11}$$

where t is the mass of the meson when positive and when negative is the square of the 4-momentum transfer in the virtual exchange. Adding up the contributions, the scattering amplitude is given by [14]:

$$A(s,t) \sim f(t) \left(\frac{s}{s_0}\right)^{\alpha(t)}, \tag{2.12}$$

where s_0 is a hadronic energy scale. The differential cross-section is then [14]:

$$\frac{d\sigma}{dt} = F(t) \left(\frac{s}{s_0}\right)^{2\alpha(t)-2}, \tag{2.13}$$

where $F(t)$ is the form factor for the interaction. The total cross-section is related to the forward ($t = 0$) amplitude for elastic scattering and is given by:

$$\sigma_{tot} \sim \left(\frac{s}{s_0}\right)^{\alpha_0 - 1}. \tag{2.14}$$

For elastic scattering reactions, Regge theory interpretations involve the exchange of neutral Reggeons which result in a predicted fall of the total cross-section with

increasing energy. This is seen at low energy but at higher centre-of-mass energies ($\sqrt{s} > 10\,\text{GeV}$) a slow rise with increasing energy is observed. All the known mesons have intercepts, α_0, less than around 0.6. The observed energy dependence of the elastic cross-sections corresponds in Regge theory to the exchange of a set of particles with even spin, the quantum numbers of the vacuum and an intercept, α_0, greater than one. The corresponding Regge trajectory is known as the *Pomeranchuk* trajectory or, alternatively, the pomeron. High energy elastic reactions, such as $ep \to epX$ in the case of HERA, are dominated by pomeron exchange in the Regge picture. In the case of elastic vector meson production, $ep \to eVp$, at HERA energies, the dominance of pomeron exchange means the cross-section can be expressed as:

$$\frac{d\sigma}{dt} \sim (\frac{W^2}{W_0^2})^{2\alpha_{I\!P}(0)-2} e^{bt}, \tag{2.15}$$

where b is referred to as the slope parameter and is defined as:

$$b = b_0 + 4\alpha'_{I\!P} ln(\frac{W}{W_0}). \tag{2.16}$$

The relevant centre-of-mass energy is now W and the typical hadronic energy scale S_0 has now been written as W_0. Donnachie and Landshoff [18] have fitted many hadronic total cross-sections using the sum of a contribution from meson exchange, dominating at low energies, and a contribution from pomeron exchange, dominating at high energies. They find good agreement with the data and obtain a value of $\alpha_0 = 1.0808$ for the pomeron intercept and an α_0 value of around 0.5 for the meson intercept.

2.4.2 Diffractive Kinematics

Figure 2.3 shows a schematic view of an ep scattering event. The hadronic final state is divided into two regions, X and Y, separated by the largest rapidity gap in the event. The cross-section can then be measured in clearly defined regions of M_X and M_Y, the respective masses of the two systems. This definition is general and does not pre-suppose that the process involved is diffraction. It is useful to define the following additional kinematic variables:

$$t = (P - Y)^2, \tag{2.17}$$

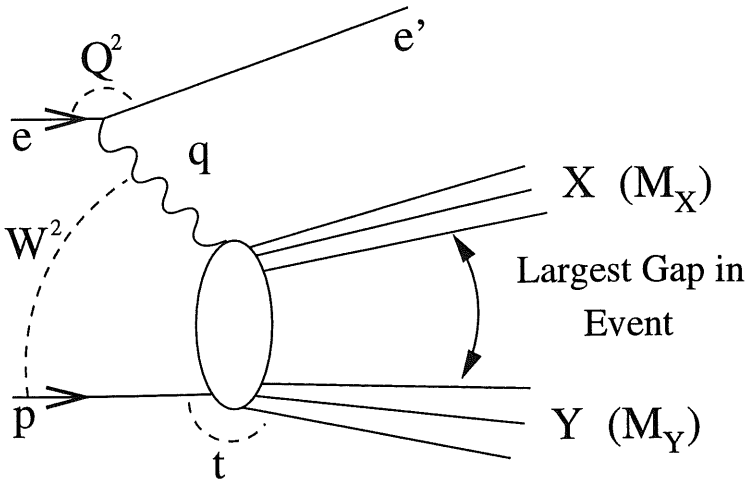

Figure 2.3: A schematic picture of a DIS event showing the definitions of the quantities used in the analysis of DIS rapidity gap events.

$$x_{I\!P} = \frac{q.(P-Y)}{q.P}, \tag{2.18}$$

$$\beta = \frac{x_{bj}}{x_{I\!P}}, \tag{2.19}$$

where Y is the 4-momentum of system Y, t is the squared 4-momentum exchanged at the proton vertex and $x_{I\!P}$ can be thought of as the fraction of the proton's momentum carried by the exchanged colourless object. The quantity β corresponds to the proportion of the momentum of the colourless object carried by the struck parton, i.e. it is analogous to x_{bj}.

2.4.3 The Structure of Diffractive Exchange

The structure of the colourless exchange leading to the production of large rapidity gap events at HERA in DIS can be studied by defining a structure function $F_2^{D(4)}$, analogous to $F_2(x, Q^2)$, in terms of which the cross-section for rapidity gap events is written

$$\frac{d^4(x_{I\!P}, t, x, Q^2)}{dx_{I\!P}\, dt\, dx\, dQ^2} = \frac{4\pi\alpha^2}{xQ^2}\Big(1 - y + \frac{y^2}{2(1+R^D)}\Big) F_2^{D(4)}(x, Q^2, x_{I\!P}, t), \tag{2.20}$$

where R^D accounts for the contribution from longitudinally polarised photons. This can be compared with equation 2.9. In the following, as measurements are made at relatively small y, it is assumed that $R^D \sim 0$. The discussion is not affected by allowing the variation of R^D over the maximum possible range.

If the process producing rapidity gap events is diffraction, Regge models predict that the structure function $F_2^{D(4)}(x, Q^2, x_{I\!P}, t)$ may be factorised into two components:

$$F_2^{D(4)}(x, Q^2, x_{I\!P}, t) = f_{I\!P/p}(x_{I\!P}, t) F_2^{I\!P}(\beta, Q^2), \tag{2.21}$$

where $f_{I\!P/p}(x_{I\!P}, t)$ is the flux factor describing the probability of finding a pomeron within the proton at $x_{I\!P}$ and t. Equation 2.21 may be interpreted as the statement that the pomeron has the same structure, described by $F_2^{I\!P}(\beta, Q^2)$, regardless of the fraction of the proton's momentum it carries. The first measurements on diffractive structure at HERA supported the hypothesis of factorisation [19], suggesting that rapidity gap events are indeed diffractive in origin.

Because the scattered proton cannot be detected in the H1 detector, t cannot be measured directly. Hence $F_2^{D(4)}(x, Q^2, x_{I\!P}, t)$ cannot be measured directly. An integration over t is performed and the quantity

$$F_2^{D(3)}(x, Q^2, x_{I\!P}) = \int_{t_{min}}^{1} F_2^{D(4)}(x, Q^2, x_{I\!P}, t)\, dt \tag{2.22}$$

is measured, where t_{min} is the minimum kinematically allowed value of t. Figure 2.4 shows the measurement of $F_2^{D(3)}(x, Q^2, x_{I\!P})$ made using data from the 1994 running period of H1 [20]. The lack of a universal $x_{I\!P}$ dependence over all bins of β and Q^2 shows a breaking of the factorisation hypothesis. The breaking of factorisation, which occurs at large values of $x_{I\!P}$ or small values of β, can be explained by allowing for a "sub-leading" Reggeon making an increasing contribution to the structure function at low β. A good fit to the data within the Regge picture is obtained by allowing a pomeron and a meson contribution plus possible interference between them. This fit is shown in figure 2.4. Under this hypothesis, $F_2^{D(3)}$ can be parameterised as follows:

$$F_2^{D(3)} = f_{I\!P/p}(x_{I\!P}) F_2^{I\!P}(\beta, Q^2) + f_{I\!R/p}(x_{I\!R}) F_2^{I\!R}(\beta, Q^2) + Int, \tag{2.23}$$

where $f_{I\!R/p}(x_{I\!R})$ describes the flux of Reggeons and $F_2^{I\!R}(\beta, Q^2)$ their structure. The term Int takes into account the interference between the pomeron and Reggeon exchanges.

Making the assumption that the purely diffractive component of $F_2^{D(3)}$ is factorisable, it is possible to treat the pomeron as a hadron with partonic structure. The pomeron structure function, $F_2^{I\!P}$, can then be interpreted in a similar way to F_2 in the QPM:

$$F_2^{I\!P}(\beta, Q^2) = \sum_i e_i^2 \beta f_i(\beta, Q^2), \tag{2.24}$$

where $f_i(\beta, Q^2)$ is the density of parton type i, in this case in the pomeron. To extract a physically measurable quantity, the following is defined:

$$\tilde{F}_2^D(\beta, Q^2) = \int_{0.0002}^{0.01} F_2^{D(3)}(\beta, Q^2, x_{I\!P}) dx_{I\!P}, \tag{2.25}$$

which is proportional to $F_2^{I\!P}$. Over the chosen $x_{I\!P}$ range, the contribution from the sub-leading Reggeon is negligible.

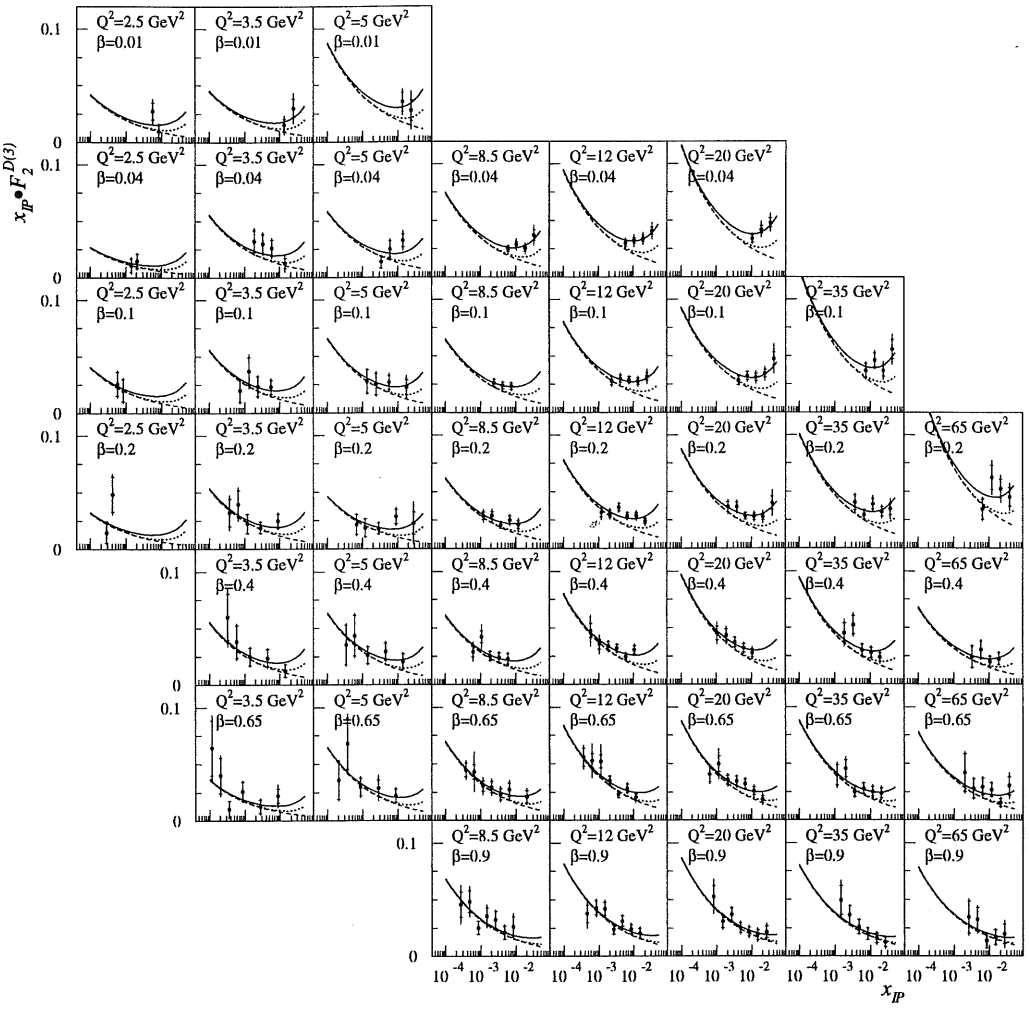

Figure 2.4: H1 measurements of the structure function $F_2^{D(3)}(\beta, Q^2, x_{I\!P})$ presented as a function of $x_{I\!P}$ in regions of β and Q^2; the dashed line shows the fitted pomeron exchange contribution, the dotted line shows the fitted meson exchange contribution and the solid line shows the total fit. This fit is described in detail in the text.

Figure 2.5 shows the H1 measurement of $\tilde{F}_2^{D(3)}(\beta, Q^2)$ in bins of β. In analogy

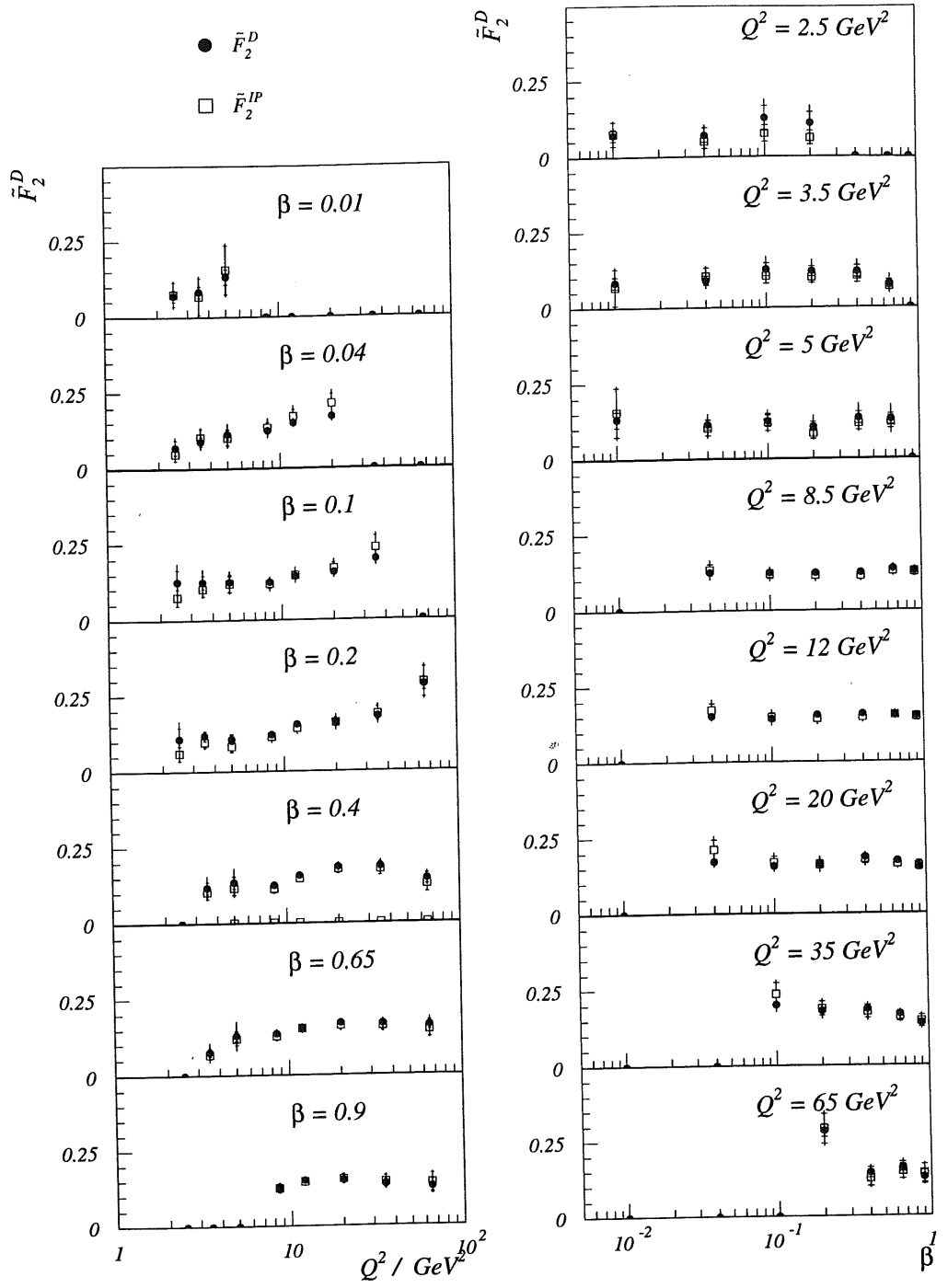

Figure 2.5: H1 measurements of the structure function $\tilde{F}_2^{D(3)}(\beta, Q^2)$ presented as a function of Q^2 in regions of β (left) and as a function of β for various Q^2 (right).

with the measurements of the proton structure function, scaling violations are observed with a significant positive slope with Q^2 at low β. This can be compared to the increase of F_2 with Q^2 at low x, indicating a large gluon content of the proton in this region. The measurement is thus an indication of significant gluon content in the framework of a partonic pomeron. Included in figure 2.6 are two fits

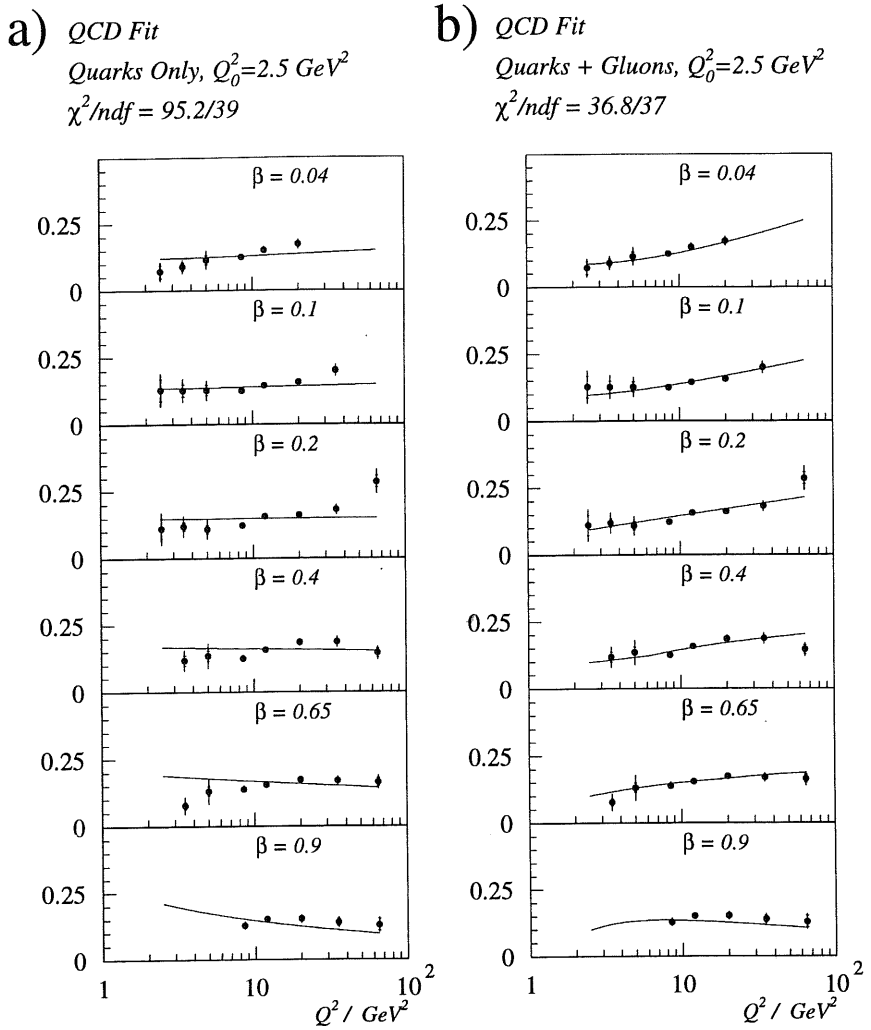

Figure 2.6: H1 measurements of the structure function $\tilde{F}_2^{D(3)}(\beta, Q^2)$ presented as a function of Q^2 in regions of β together with the results of two QCD based fits: a) allowing only quarks at the starting scale $Q_0^2 = 2.5\,\mathrm{GeV}^2$; b) allowing quarks and gluons at the starting scale.

to $\tilde{F}_2^{D(3)}(\beta, Q^2)$ based upon QCD parameterisations. The first allows only quark initiated processes at the starting scale, $Q_0^2 = 2.5$ GeV^2, with the Q^2 evolution being described by the DGLAP evolution equations. The fit shown in b) allows

for the presence of both quark and gluon initiated processes at the starting scale. In this QCD parameterisation, it is clear that the presence of gluon-initiated processes is required to describe the observed scaling violations. Figure 2.7 shows a diagram of each type of process.

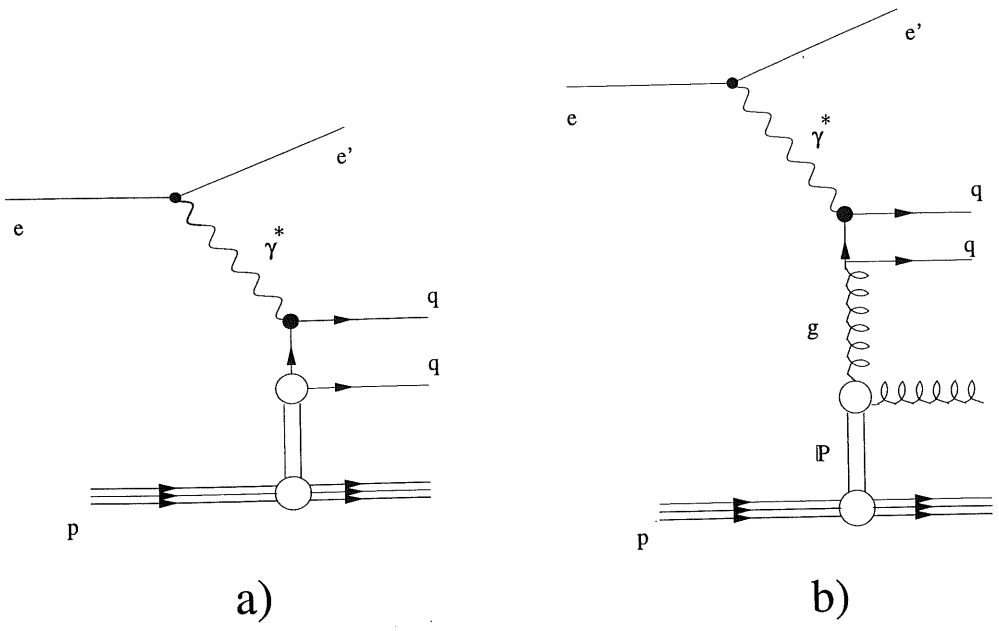

Figure 2.7: Diagrams of *ep* interactions involving: a) a quark dominated pomeron; b) a gluon dominated pomeron.

The parton densities extracted from the above QCD fits are shown in figure 2.8. As argued above from the observed scaling violations in $\tilde{F}_2^{D(3)}(\beta, Q^2)$, the pomeron's momentum is seen to be carried primarily by gluons.

Measurements of the hadronic final state in diffractive DIS have been made. The thrust [21] and energy-flow [22] distributions support the above evidence that diffractive events are gluon-initiated processes. A measurement of the D^* cross-section in diffractive DIS has proved to be inconsistent with a diffractive model in which only quark-initiated processes are present in the starting scale [23], but is compatible with expectations if a gluon dominated pomeron is assumed.

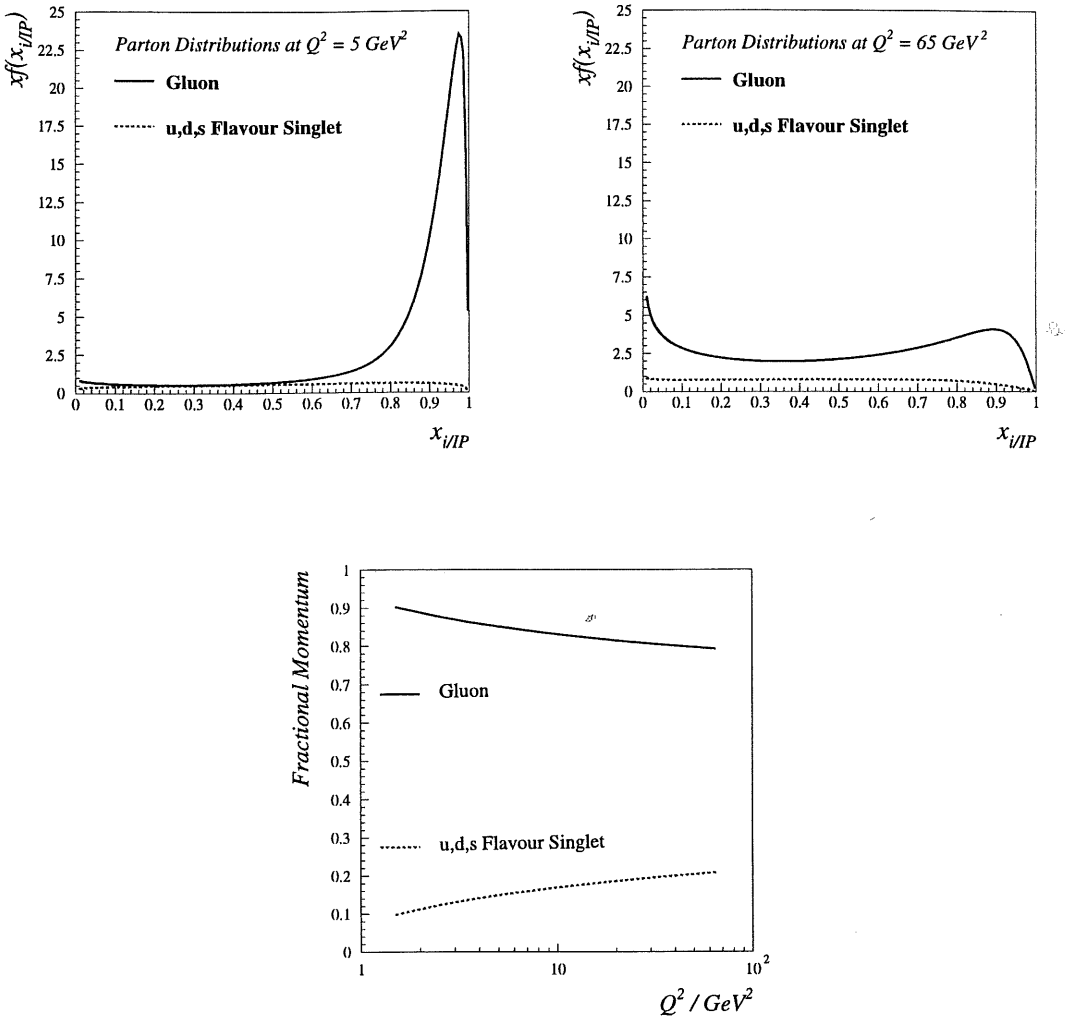

Figure 2.8: The densities of partons in the pomeron as a function of Q^2 extracted from QCD based fits to $\tilde{F}_2^{D(3)}(\beta, Q^2)$.

2.5 Diffractive Vector Meson Production

With the diffractive formalism defined in section 2.4.2, quasi-elastic vector meson production corresponds to system X being a bound state vector meson and system Y being the scattered proton. Figure 2.9 shows this along with the other possible diffractive processes.

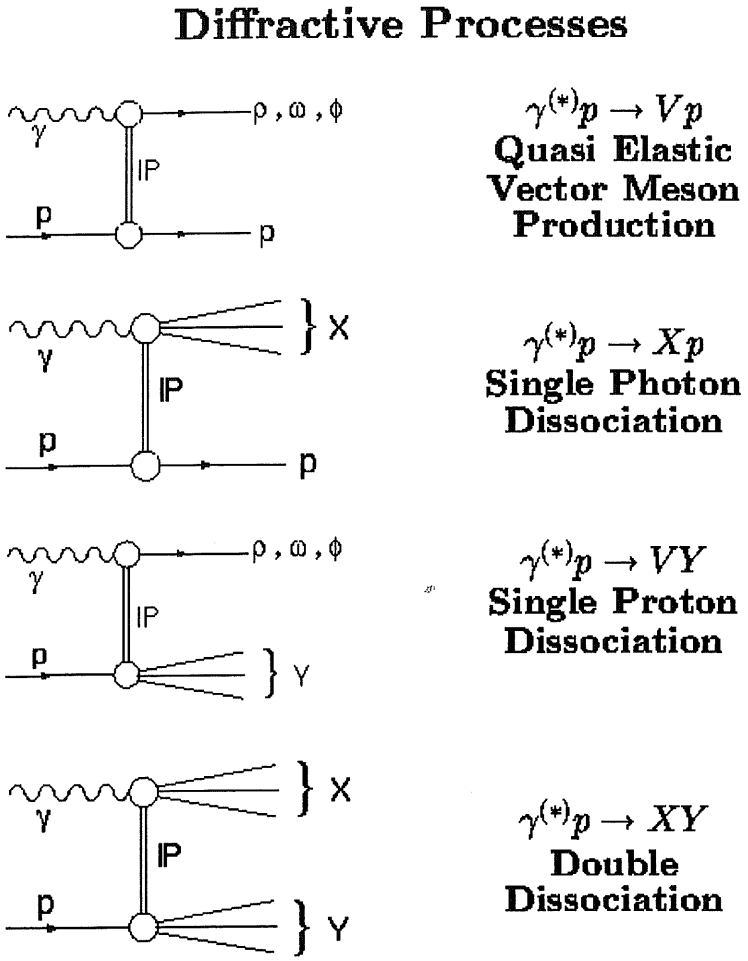

Figure 2.9: The possible diffractive processes involving dissociation at neither vertex, either vertex or both vertices.

HERA allows the Q^2 and W range of vector meson cross-section measurements to be greatly extended, thus allowing a far more detailed comparison with diffractive models than previously possible.

2.5.1 Vector Meson Photoproduction

Soft Phenomenological Models

The diffractive production of vector mesons in photoproduction has for a long time been interpreted using the couplings of Regge theory and the Vector Dominance Model (VDM) [24]. The VDM was developed to describe many aspects of soft processes in photoproduction. It was observed that many of the characteristics of photon-hadron scattering were similar to those of hadron-hadron scattering indicating that the photon can behave hadronically. This can be thought of as the photon fluctuating into a $q\bar{q}$ pair which subsequently develops into a hadronic state. This state must have the same quantum numbers as the photon, $J^{PC} = 1^{--}$. In the basic VDM, the hadronic component of the photon is treated as being the superposition of the lightest vector mesons, ρ, ω and ϕ. Photoproduction processes $\gamma p \to X$ can then be described in the VDM as the coupling of the photon to the meson followed by the scattering process $Vp \to X$. In the case of elastic vector meson production, the process $Vp \to Vp$ at high energy is described in Regge theory by the exchange of a single pomeron. At the energies available at fixed target experiments, the dependence of the lowest lying vector meson cross-sections on the centre-of-mass energy, W, follows that expected from Regge theory with a pomeron intercept of 1.08, as determined by Donnachie and Landshoff.

Figure 2.10 shows the W dependence of the lowest lying meson cross-sections combining HERA data with fixed target data. At the higher energies of the HERA data, the energy dependence of the light vector mesons, ρ, ω and ϕ, follows that observed at lower energy. The J/ψ data, however, tell a different story at high energy. The W dependence is too steep to be reconciled with a Regge picture involving the Donnachie-Landshoff pomeron intercept. This so-called "soft pomeron" prediction is shown on the figure as a dotted line.

Hard QCD Based Models

The steep energy dependence of the J/ψ photoproduction data is incompatible with the soft pomeron models. Comparison can, however, be made with so called "hard" pomeron models based upon perturbative QCD. Various models [25] [26]

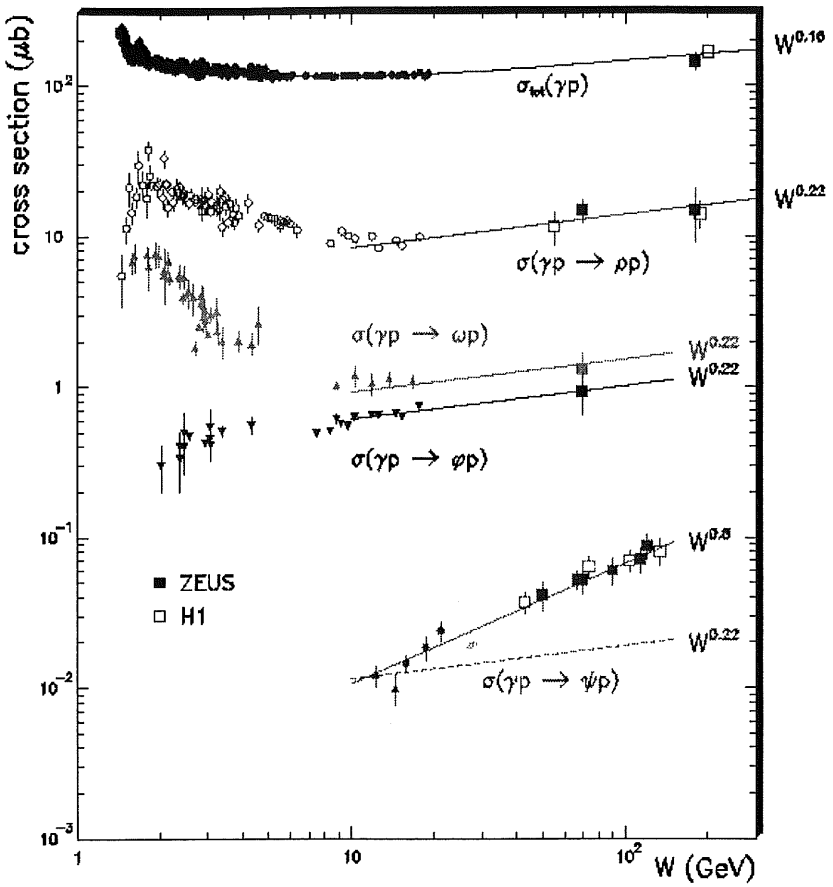

Figure 2.10: Cross-section measurements in photoproduction as a function of γp centre-of-mass energy, W, combining ZEUS and H1 data with lower energy fixed target data. Shown are the total γp cross-section and the ρ, ϕ, ω and J/ψ cross-section measurements. The fits performed are described in the text.

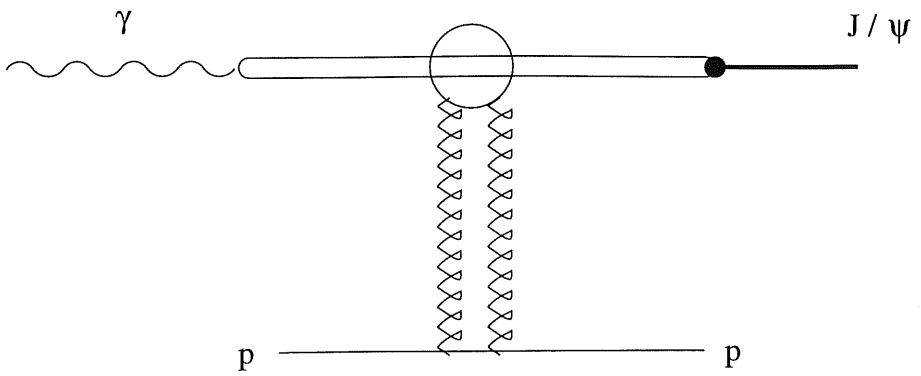

Figure 2.11: Illustration of the QCD based model of Ryskin et al. and Brodsky et al. The photon fluctuates into a $q\bar{q}$ pair which, after subsequent interaction with the two-gluon pomeron, becomes a J/ψ meson.

treat the pomeron as a two-gluon system, the simplest colour singlet state. Figure 2.11 shows the process modelled. The interaction is broken down into 3 separate sub-processes. Firstly, the photon fluctuates into a $c\bar{c}$ pair which subsequently interacts with the proton via two-gluon exchange. Finally, the $c\bar{c}$ pair forms a J/ψ meson. The process can be factorised due to the short time scale of the interaction between the quark pair and the proton in comparison to the other two processes. The mass of the $c\bar{c}$ pair provides the hard scale for the calculation.

In these models, the differential cross-section for J/ψ photoproduction is proportional to the squared gluon density of the proton:

$$\frac{d\sigma}{dt} \sim \left[xg(x,Q^2)\right]^2, \tag{2.26}$$

hence measurements of diffractive J/ψ photoproduction are sensitive to the gluon density in the proton. The much steeper energy dependence of the J/ψ can be reconciled in this model with the known increase in the gluon distribution at low x (high W) responsible for the rise of the proton structure function F_2 in this region. The solid line fit to the J/ψ data in figure 2.10 shows a prediction from the Ryskin model [25]. This provides a good fit. It should be noted that, due to the input to the model from the gluon density of the proton, the exact shape of the prediction is dependent upon the choice of input parton density distributions.

2.5.2 Angular Decay Correlations

The angular distributions of the decay products of a resonance can be used to establish information on the production mechanism. The polarisation of the produced meson can be inferred from the relevant decay angles.

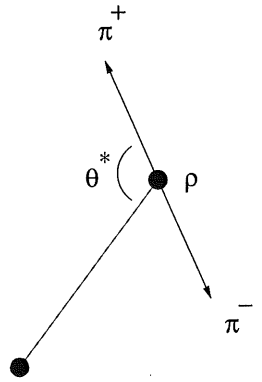

Figure 2.12: Defined decay axes in the case of a two particle decay.

To define the decay axes, the rest frame of the meson is used. In the case of a two particle decay, for example $\rho \rightarrow \pi^+\pi^-$, the direction of the positive pion is used to define the angle θ^*, although, in this frame, the direction of the negative meson would yield the same result. As the axis for the angular definitions, the direction of the outgoing meson in the $\gamma^{(*)}p$ frame is used. Figure 2.12 shows this definition for the decay $\rho \rightarrow \pi^+\pi^-$.

In the case of a three particle decay, for example $\omega \rightarrow \pi^+\pi^-\pi^0$, θ^* is defined by the normal to the decay plane. Again the direction of the outgoing meson is used as the axis. Figure 2.13 shows this definition for the ω decay.

Information on the exchange mechanism can be deduced from the $\cos\theta^*$ distribution. In the framework of Regge theory, s-channel helicity conservation (SCHC) is predicted. SCHC predicts that in the production process $\gamma^{(*)}p \rightarrow Vp$ the meson adopts the polarisation of the incoming (virtual) photon. In other words, longitudinally polarised photons result in longitudinally polarised mesons and transverse photons result in transverse mesons. In the case of a vector meson decaying into two or three spinless particles ($\rho \rightarrow \pi^+\pi^-$ or $\omega \rightarrow \pi^+\pi^-\pi^0$) the

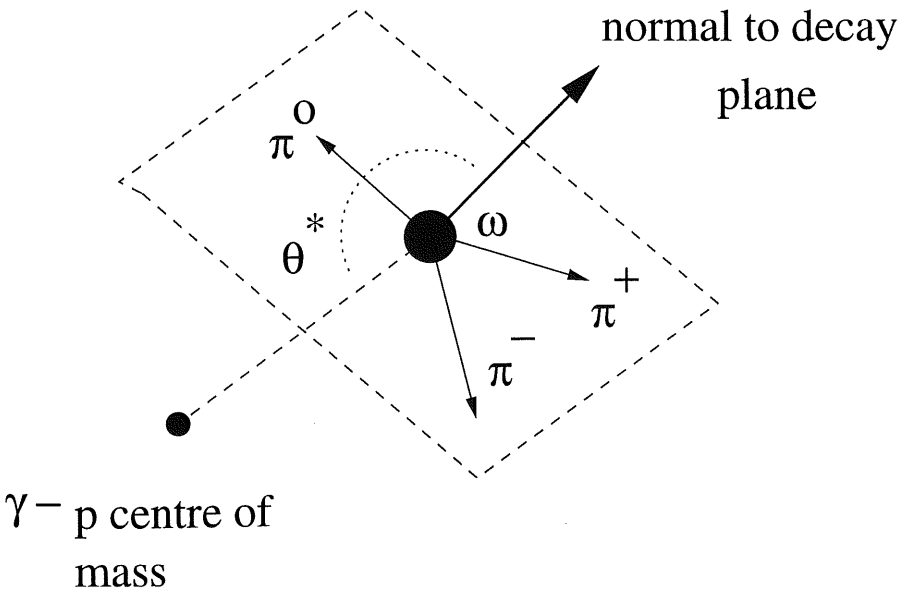

Figure 2.13: Defined decay axes in the case of a three particle decay.

following $\cos\theta^*$ distribution is obtained [27]:

$$\frac{d\sigma}{d\cos\theta^*} \sim (3r_{00}^{04} - 1)\cos^2\theta^* + (1 - r_{00}^{04}), \tag{2.27}$$

where r_{00}^{04} is the spin density matrix element which specifies the probability that the vector meson is longitudinally polarised. Results form HERA on vector meson photoproduction [28] [29] [30] have yielded r_{00}^{04} values consistent with 0. Hence real photons only produce transversely polarised mesons, consistent with the hypothesis of SCHC.

At high Q^2, the angular decay distributions of the mesons can be used to measure the respective ratios of the transverse and longitudinal cross-sections. The results of such analyses at HERA are discussed later in this chapter.

2.6 Vector Meson Electroproduction

The Q^2 and W regions accessible at HERA have enabled detailed studies of the electroproduction of vector mesons at high energy. These processes are of great theoretical interest as they can be compared with calculations done in the framework of perturbative QCD. If Q^2 is high enough, the presence of a hard

scale enables predictions to be made even in the case of the production of light mesons. Some such models will be mentioned later.

Measurements of elastic ρ electroproduction have been presented by H1 [31] and ZEUS [32]. The observed properties are as follows:

- The 2π mass spectra obtained in the analyses show a significantly different form to those seen in photoproduction. No Ross-Stodolsky skewing term is required in describing the observed mass spectra and, allowing for a small amount of non-resonant background, the spectra are well described by p-wave Breit-Wigner distributions.

- The measured cross-sections in each case are found to approximately follow a $(Q^2)^{-2.5}$ form for the Q^2 dependence. This is consistent with the Q^2 dependence seen in the NMC [33] and EMC [34] ρ electroproduction measurements which are restricted to a much lower centre-of-mass energy ($W <$ 20 GeV).

- The angular decay distributions of the produced ρ mesons are found to be consistent with SCHC with the longitudinal cross-section dominating at higher Q^2. The ρ spin density matrix representing the probability that the ρ mesons are longitudinally polarised, r^{04}_{00}, is measured to be $0.73 \pm 0.05 \pm 0.02$ in the H1 data [31] with the ZEUS measurements yielding a similar result [32]. Both results are made at an average Q^2 of around 13 GeV^2.

- The b slope of the t-distribution ($\mathrm{d}\sigma/\mathrm{d}t \sim \mathrm{e}^{bt}$) is found to be significantly smaller than that seen in photoproduction. H1 and ZEUS measure b to be $7 \pm 0.8 \pm 0.4$ GeV^{-2} and $5.1 \pm 1.0 \pm 1.0$ GeV^{-2} respectively. This decrease in the slope is expected due to the smaller separation of the $q\bar{q}$ pair in the photon at high Q^2.

- Combining the HERA results with data from lower energy experiments, the rise of the cross-section with W is much steeper than that seen in photoproduction and incompatible with that predicted by the VDM and soft-pomeron model.

Results on the elastic electroproduction of ϕ mesons have also been presented by H1 [35] and ZEUS [36]. The Q^2, W and t distributions obtained are similar

to those seen in ρ production. The angular decay distribution over a similar Q^2 range supports SCHC, giving a similar result for the proportion of longitudinally polarised photons.

A study of ρ production in proton dissociation in a similar Q^2 range has been presented by H1 [35]. These measurements are interesting as they allow the testing of the factorisation hypothesis; what effect does the dissociation of the proton have on the ρ mesons produced at the virtual photon pomeron vertex? It is found that the ρ mesons produced exhibit the same properties as those produced in elastic electroproduction. The mass spectrum is well described by a p-wave Breit-Wigner distribution with mass and width at the same values as in electroproduction. The Q^2 dependence and the angular decay characteristics are also consistent with those in electroproduction. As expected, the t distribution is much flatter with a b value of around 2.1.

2.7 The ρ' Resonance

Unlike the well established and understood $\rho(770)$ meson, there has been much confusion over the nature of the ρ' resonance. The ρ' resonance was first observed as a broad enhancement in the 4 π mass spectra resulting from the reactions $e^+e^- \rightarrow 2\pi^+2\pi^-$ [37] and $\gamma p \rightarrow 2\pi^+2\pi^- p$ [38]. The parameters of the resonance were extracted in each case and found to be typically:

$$M_{\rho'} = 1.57 \pm 0.05 GeV$$

$$\Gamma_{\rho'} = 0.51 \pm 0.02 GeV$$

in e^+e^- scattering [37] and

$$M_{\rho'} = 1.52 \pm 0.05 GeV$$

$$\Gamma_{\rho'} = 0.40 \pm 0.02 GeV$$

in γp reactions [38]. The γp analyses had to contend with the significant non-resonant background present in the sample. Analysis of the 4 π system in both reactions showed evidence for a significant decay via $\rho' \rightarrow \rho\pi^+\pi^-$.

The 4 π data thus formed a consistent picture of a single broad resonance being present at around 1.6 GeV. This was attributed to a ρ' resonance, the

"$\rho'(1600)$". Subsequent measurements of the reactions $e^+e^- \to \pi^+\pi^-\pi^0\pi^0$ and $\gamma p \to \pi^+\pi^-\pi^0\pi^0 p$ supported this picture of the $\rho'(1600)$, with broad peaks observed in the 4 π invariant mass spectra in the 1600 MeV mass region. Analysis of this channel in photoproduction data [39] resulted in the following resonance parameters:

$$M_{\rho'} = 1.66 \pm 0.03 GeV$$

$$\Gamma_{\rho'} = 0.30 \pm 0.05 GeV.$$

A possible explanation of the differing masses and widths is the inclusion of interference terms between the resonance and non-resonant background. One such treatment of the then available $e^+e^- \to 2\pi^+2\pi^-$ data showed that interference between a ρ' resonance and a large background due to $A_1\pi$ production allows for a resonance of mass 1.5 GeV, significantly below the mass peak observed in the data.

Evidence for the decay $\rho' \to \pi^+\pi^-$ provided significant new information on the ρ' resonance. Data from experiments on $\gamma p \to \pi^+\pi^-$ [40] showed a peak at around 1600 MeV with a width significantly narrower than those in the 4 π data, around 0.23 ... 0.28 GeV. Information from the reaction $e^+e^- \to \pi^+\pi^-$ in the 1600 MeV region suggested, however, a very different structure to that seen in the photoproduction data [41]. Here a peak in the region of 1700 MeV is seen along, interestingly, with a dip at around 1600 MeV signifying interference. This observation is inconsistent with the $\rho'(1600)$ picture which fits in with the photoproduction data. To provide an overall consistent understanding of the data, the presence of two interfering ρ' resonances in the 1600 MeV mass region is required.

The conventional Particle Data Group (PDG) listings of the ρ' resonances were obtained by detailed fitting of the $e^+e^- \to \pi^+\pi^-$ data by Donnachie, Clegg and Mirzaie. These results are described in [42]. This data set is the most useful of the above due to the skewing of the ρ resonance in the photoproduction channel and the indication of large non-resonant background contributions in the $2\pi^+2\pi^-$ decay mode. A fit is performed using three interfering contributions to describe the tail of the ρ resonance, represented by a Breit-Wigner distribution with a mass-dependent width, and two ρ' resonances, ρ'_1 and ρ'_2, also represented by Breit-Wigner distributions. The data are well described if the relative phases of the ρ, ρ'_1 and ρ'_2 resonances are +, − and +, respectively. In this case the

dip in the data at 1600 MeV is produced due to a cancellation of the imaginary parts of the two ρ' resonances in this region. From fitting this data, the following resonance parameters are obtained :

$$M_{\rho'_1} = 1.465 \pm 0.025 GeV$$

$$\Gamma_{\rho'_1} = 0.235 \pm 0.025 GeV$$

and:

$$M_{\rho'_2} = 1.700 \pm 0.025 GeV$$

$$\Gamma_{\rho'_2} = 0.220 \pm 0.025 GeV.$$

The $\gamma p \rightarrow \pi^+\pi^- p$ data is complicated by the skewing of the ρ and the presence of the J^{PC} 3^{--} resonance, the $g(1690)$. The diffractive production of this resonance has been observed in the reaction $\gamma p \rightarrow \eta\pi^+\pi^- p$ [43]. When taking the measured $g(1690)$ production cross-section into account, the two resonance hypothesis fits the data well. The relative strengths of the two resonances are, however, dependent on the parameterisation of the tail of the skewed ρ contribution and the size of the $g(1690)$ subtraction.

In the 2 π^+ 2 π^- decay channel, the e^+e^- data can be well described using an interfering resonance picture and the fixed masses and widths extracted from the $e^+e^- \rightarrow \pi^+\pi^-$ channel. A small amount of non-resonant background, assumed to arise from $\rho \rightarrow A_1\pi$ production, is also necessary. An alternative description [44] can be provided by the interpretation of a single resonance interfering with a much larger background. The results can then be used to predict the relative contributions of the two resonances in $\gamma p \rightarrow 2\pi^+2\pi^- p$. The largest statistics data sample on this channel is presented in [38]. To extract the resonance signal from the large background contributions, the data is analysed in bins of 4 π mass assuming two differing models for the production channel, πA_1 and $\rho\epsilon$ with various assumed background distributions. In each case the major background contributions are found to follow $\rho\pi\pi$ p_t limited phase space and 4 π phase space. The signal contribution is shown to dominate in each case and the πA_1 and $\rho\epsilon$ peaks extracted follow a very similar shape. Taking the limits of the ratio of ρ'_1 to ρ'_2 cross-sections from the e^+e^- data combined with the $\gamma p \rightarrow \pi^+\pi^-$ data, the two resonance picture fits the data with a contribution from the $g(1690)$ the size of which varies depending on which ratio is used.

If the hypothesis of two ρ' resonances is indeed correct, it would be natural to interpret them as the lowest lying radial excitation $1^3S_1 \rightarrow 2^3S_1$ and lowest lying orbital excitation $1^3S_1 \rightarrow 1^3D_1$ respectively. Predictions from a model by Godfrey and Isgur [45] result in a radial excitation at around 1.45 GeV and an l-excitation at around 1.66 GeV. However, as detailed properties of the resonances are not yet available due to the lack of precision of ρ' data, it is not possible to unambiguously identify the ρ'_1 and ρ'_2 resonances with those predicted in this model.

2.8 Models of Exclusive Vector Meson Electroproduction

At high Q^2, predictions of light vector meson (ρ, ω, ϕ) electroproduction can be made in the framework of the two-gluon exchange models presented in [25]. One such model is presented in [26]. At sufficiently high Q^2, the momentum transfer provides the hard scale required to make predictions within QCD. This section includes alternative models of vector meson production which make interesting predictions on the production of excited vector meson states.

2.8.1 Vector Meson Electroproduction via Open $q\bar{q}$ Production

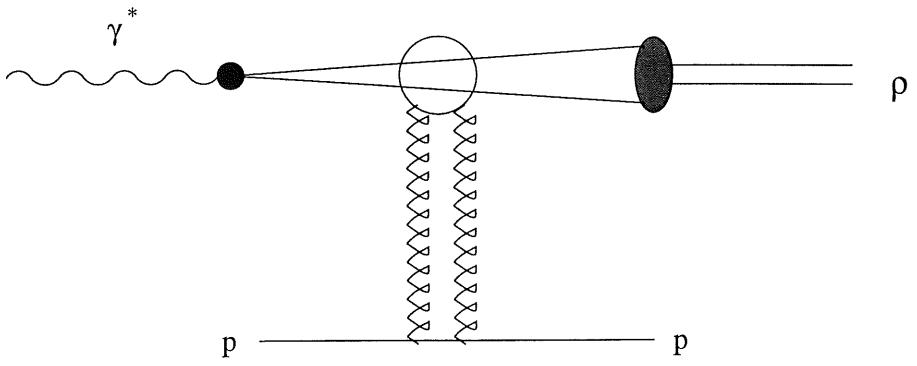

Figure 2.14: The process modelled in QCD by Martin et al. The virtual photon fluctuates into a $q\bar{q}$ pair which, after subsequent interaction with the two-gluon pomeron, becomes a vector meson, in this case a ρ.

One alternative QCD description of the electroproduction of ρ mesons is provided by Martin, Ryskin and Teubner [46]. This model describes the production mechanism by the production of "open" $q\bar{q}$ pairs. The diagram for this process is shown in figure 2.14. This model differs from the models in [25] and [26] in the way the resonance is formed from the $q\bar{q}$ pair. In [25] and [26] a convolution of the $q\bar{q}$ wave function with the meson wave function is used. In the open $q\bar{q}$ model the ρ is formed some time after the interaction between the $q\bar{q}$ pair and the proton. In the mass region ΔM around the ρ meson mass, the $q\bar{q}$ pair is assumed to form into a ρ or ω. The reasoning for this is based upon the hadron-parton duality hypothesis which gives the following relationship for the process $e^+e^- \rightarrow hadrons$:

$$\left(\sum_h \sigma(e^+e^- \rightarrow \gamma^* \rightarrow h)\right)_{\Delta M^2} \approx \left(\sum_h \sigma(e^+e^- \rightarrow \gamma^* \rightarrow q\bar{q})\right)_{\Delta M^2} \tag{2.28}$$

where the total hadron production ($h = \rho, \omega$ ..) rate is well described by that of the $q\bar{q}$ pair over a limited mass interval ΔM^2. The prediction of the theory is based on a mass squared region, ΔM^2, between 1 GeV^2 and 1.5 GeV^2 where the production of higher order states ($q\bar{q} + g$, $q\bar{q} + 2g$,$q\bar{q} + q\bar{q}$ ..) is strongly suppressed and phase space requires the final state to be dominantly 2π and, to a lesser extent, 3π. Hence, allowing for a contribution from ω production into 3 π states, the prediction of $J = 1$ open $u\bar{u}$ and $d\bar{d}$ electroproduction via pomeron exchange (a two gluon system in the QCD description) gives directly the ρ electroproduction cross-section. As in the models presented in [25] and [26], the predictions of this model are dependent on and therefore sensitive to the gluon distribution of the proton.

This model has been used to predict many features of ρ electroproduction. Its most interesting prediction is that of the Q^2 dependence of the ratio of longitudinal to transverse cross-sections. In standard perturbative QCD models [25], the transverse cross-section is predicted to have a much steeper Q^2 dependence than that of the longitudinal cross-section:

$$\frac{\sigma_L}{\sigma_T} \sim Q^2 \tag{2.29}$$

which is in contrast to the data [31] [32]. In the open $q\bar{q}$ model, however, the following is obtained:

$$\frac{\sigma_L}{\sigma_T} = \frac{Q^2}{M^2}\left(\frac{\gamma}{\gamma+1}\right)^2, \tag{2.30}$$

where M is the invariant mass of the $q\bar{q}$ pair and γ is the anomalous dimension of the gluon, defined by:

$$xg(x, K^2) \sim x^{-\lambda}(K^2)^{\gamma}. \tag{2.31}$$

The differing behaviour of γ with changing Q^2 acts to suppress the rise of the ratio σ_L/σ_T at high Q^2. Using existing measurements of the gluon distribution in the proton, a good agreement with HERA data is obtained for the ratio in equation 2.29. Conversely, if high precision measurements of the ratio are made at HERA with greater luminosity, ρ electroproduction measurements can be used as a probe of the gluon density.

ρ' Electroproduction via Open $q\bar{q}$ Production

The open $q\bar{q}$ production model has been used to make predictions for the electroproduction of ρ excitations in the 1.4 GeV - 2.0 GeV mass region. The calculation is complicated somewhat by the presence of the $g(1690)$ $J^P = 3^-$ resonance in the mass region considered. The "hard" QCD pomeron can distort the initial $\gamma^* \to q\bar{q}$ system resulting in the possible production of non $J^P = 1^-$ states. Thus the diffractive production of the $g(1690)$ state is possible. To predict the production of the ρ excitations, the open $q\bar{q}$ cross-section in both the $J = 1$ and $J = 3$ states is integrated over the mass interval 1.3 GeV $< M <$ 1.8 GeV and the same set of proton parton densities as in the ρ predictions is used.

It is found from the calculations that, at the lowest Q^2 values considered, $Q^2 \approx 8$ GeV^2, the $\rho'(1^-)$ production rate is comparable with that of the ρ with the ρ cross-section falling more steeply with Q^2. The $\rho'(3^-)$ rate is predicted to be not insignificant, around 0.1 of that of the 1^- excitation. The Q^2 dependence of the ratio σ_L/σ_T is predicted to be much flatter than that for the ρ for both the 1^- and 3^- excitations, although the dependence for the 3^- state is somewhat dependent on the parameters in the model. This flatter distribution is due to the factor Q^2/M^2 in equation 2.30.

2.8.2 Colour Dipole Model of Vector Meson Electroproduction

Predictions for the electroproduction of light vector mesons are made in a model by Nemchik, Nikolaev, Predazzi and Zakharov. Within this model [47] hadrons and photons are treated as colour dipoles with transverse dipole separation, r, frozen during the interaction. The model predicts the vector meson production rate for both the perturbatively calculable high Q^2 and large meson mass range and for the kinematic region where Q^2 and the mass of the meson are small. The production rate is calculated via the colour dipole cross-section $\sigma(\nu, r)$ which is dependent on the energy, ν, and the dipole separation, r. The imaginary part of the vector meson production amplitude at $t = 0$ is given as:

$$Im(< V|\sigma(\nu,r)|\gamma^* >) = Im(\int_0^1 dz \int d^2r\sigma(\nu,r)\Psi_V^*(r,z)\Psi_{\gamma^*}(r,z))$$

The production amplitude is therefore dependent upon the colour dipole cross-section and the probability amplitudes $\Psi_V^*(r,z)$ and $\Psi_{\gamma^*}(r,z)$, representing the probabilities of finding a colour dipole of size r within the vector meson and the (virtual) photon respectively. z is the proportion of the total momentum (of the meson or the photon) carried by one of the quarks. This formalism is applicable both for the perturbative and non-perturbative regions. At high meson mass and high Q^2, the separation r is small. Here the probability amplitude $\Psi_V^*(r,z)$ can be identified with the constituent quark-antiquark quarkonium wave function. In the region where Q^2 is small and the meson mass is small, perturbative calculations are not possible. Due to the contribution from the final state meson wave function, the dominant contribution to the dipole cross-section comes from the region where the dipole separation r is close to the "scanning radius", r_s, in the meson, which is given by:

$$r_s \approx \frac{A}{\sqrt{(M_V^2 + Q^2)}},$$

where A is a scale parameter and is approximatley 6. This formula is in agreement with the decrease in size of the photon with Q^2 and the decrease in the dipole separation of mesons with mass. The contribution of the cross-section at large r depends upon both the dipole cross-section for large dipoles and the non-perturbative wave-functions of the vector mesons at large r. Both of these are poorly known and precise predictions from the model can not be made in this region.

The dependence upon the $q\bar{q}$ separation of the quarks in the final state meson leads to very interesting predictions on the production of the excited state mesons. This can be illustrated by taking the Particle Data Group ρ' picture of two mesons, the $\rho'(1450)$ and the $\rho'(1700)$ [48]. As mentioned earlier in this chapter, it is a natural assumption that one of these states is the 1D excitation of the 1S ρ and the other is a 2S excitation.

For 2S mesons, the following predictions for the ratio of production cross-sections with the 1S state are obtained:

• Transversely polarised mesons. At a sufficient Q^2, the production amplitude is dominated by small dipole sizes, less than the separation at the node of the 2S wavefunction (see figure 2.15). At very low Q^2 (< 1 GeV^2), an increase in Q^2 will result in a rapid increase in the ratio as the scanning radius decreases away from the node radius r_N. At higher Q^2, as the scanning radius decreases further, the ratio tends towards 1.

• Longitudinally polarised mesons. At low Q^2, the 2S production amplitude is dominated by larger size dipole radii, greater than that at the node in the wavefunction (see figure 2.15). At some Q^2 value, around 0.5 GeV^2, there comes a point where the negative contributions from above the node and the positive contributions from below the node cancel, resulting in the production amplitude tending towards zero. As Q^2 is further increased, the dipole sizes become comparable with those in the case of the transversely polarised mesons and a steep increase of the ratio $\rho'(2S)/\rho(1S)$ with Q^2 is expected.

Figure 2.16 shows the predicted evolution of the $\rho'(2S)/\rho(1S)$ ratio at a W of 100 GeV using HERA results on the relative contributions of longitudinally and transversely polarised mesons.

2.8.3 Hard Diffractive Electroproduction of Vector Mesons in QCD

Frankfurt, Koepf and Strikman make predictions on the electroproduction of vector mesons within the framework of QCD [49]. As in the model used by Ryskin et al. [25], the matrix element of the process can be expressed as a convolution of the wave function of the photon, taking into account all the kinematically allowed

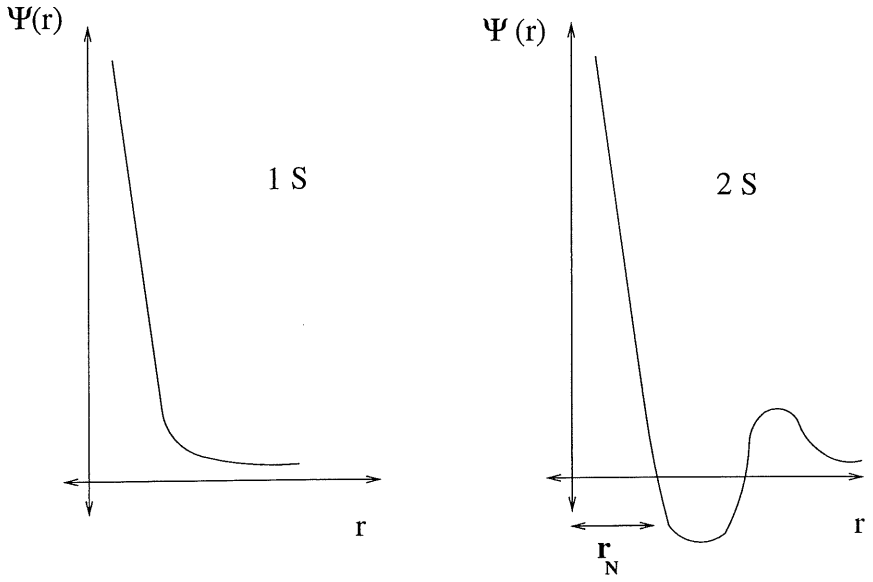

Figure 2.15: An illustration of the 1S and 2S constituent quark wavefunctions as a function of dipole separation, r. The node separation r_N is shown for the 2S wavefunction.

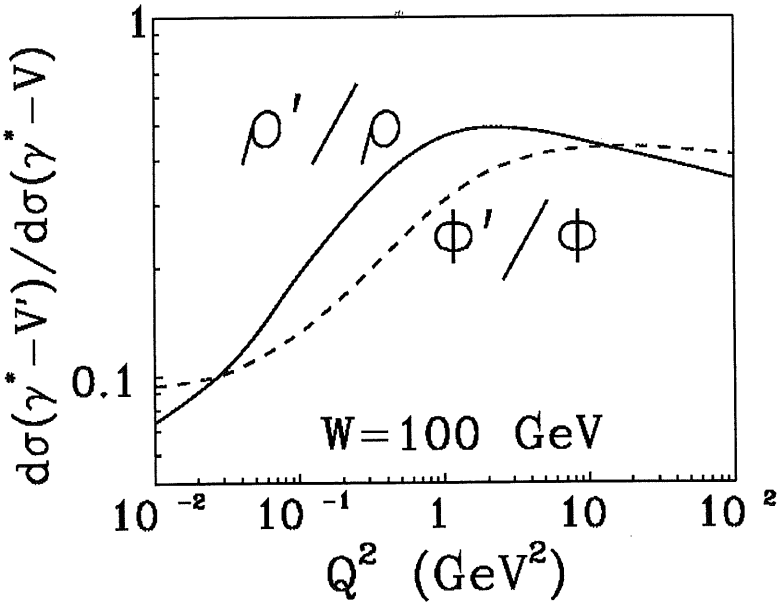

Figure 2.16: The predicted Q^2 evolution of the ratio of 2S to 1S meson cross-section amplitudes at $W = 100$ GeV.

intermediate hadronic states, the scattering amplitude of the hadronic state and the final state wavefunction of the vector meson. The resulting cross-section for longitudinally produced mesons at a t of 0 is:

$$\frac{d^L_{\gamma^* N \to VN}}{dt} = \frac{12\pi^3 \Gamma_{V\to e^+e^-} M_V \alpha_s^2(Q^2) T(Q^2) \eta_V^2 |(1 + i\frac{\pi}{2}\frac{d}{dlnx}) xg(x,Q^2)|^2}{\alpha_{EM} Q^6 N_C^2}$$

where $\Gamma_{V\to e^+e^-}$ is the decay width of the meson into an e^+ e^- pair and $xg(x,Q^2)$ is again the gluon distribution in the proton. The factor $T(Q^2)$ accounts for relative transverse motion of the $q\bar{q}$ pair and tends to 1 as Q^2 tends to infinity. The factor η_V is defined as

$$\eta_V = \frac{1}{2} \frac{\sigma \frac{dz d^2k_t}{z(1-z)} \Phi_V(z,k_t)}{\sigma dz d^2k_t \Phi_V(z,k_t)}$$

where $\Phi_V(z,k_t)$ is the light-cone wavefunction of the vector meson, depending upon the fraction of total momentum z and the transverse momentum k_t of one of the quarks in the meson. In the case of the excited state vector mesons, the model is applicable as long as the mass of the meson is much less than Q^2. To make predictions on the ratio of ρ' : ρ production, as a rough estimate the assumption is made that $\Phi_{V'}(z,k_t) = \Phi_V(z,k_t)$. The decay widths are taken from the Particle Data Group (PDG) listings [48]. The following predictions are obtained for the two PDG ρ' resonances:

$$\rho'(1450)/\rho \approx 0.45 - 0.95$$

$$\rho'(1700)/\rho \approx 0.22 \pm 0.05.$$

In view of the uncertainties in the measured widths of the resonances and the assumptions on $\eta_{V'}$, these numbers are considered good to within around a factor of two.

2.9 Monte Carlo Models

2.9.1 DIFFVM

The DIFFVM Monte Carlo is used to perform acceptance corrections for both the 4 π sample, attributed in part to the production of the ρ' resonance, and the 2 π

sample, attributed to the ρ resonance. DIFFVM is based upon the vector meson dominance model (VDM). In the case of the ρ resonance, events are generated according to the well measured nominal mass and width of the ρ. In the case of the ρ', the events are generated according to the measured parameters of the $\rho'(1450)$. To ensure that the mass distribution of the Monte Carlo events matches that of the data, the input invariant mass is reweighted to a mass of 1550 MeV. This reweighting has a negligible affect on the cross-section ratio measurement. In the Monte Carlo events, the assumption is made that all events undergo a $\rho' \to \rho\pi^+\pi^-$ decay.

In both cases, the input W and Q^2 distributions used are taken from those expected from previous HERA vector meson electroproduction results. In the case of the ρ, this is also the case for the $\cos\theta^*$ distribution. Where necessary, these distributions are reweighted to fit the data distributions after detector effects are simulated. Only a small amount of reweighting was required for all relevant distributions to be well matched. The comparisons of kinematic distributions in data and Monte Carlo are presented in chapter 4.

Chapter 3

HERA and The H1 Detector

3.1 HERA

The HERA particle accelerator is designed to store and collide 30 GeV electrons [1] and 820 GeV protons. The two storage rings are situated in the same tunnel, of circumference 6.3 km, and the two beams collide at two interaction points situated in the north and south experimental halls. These halls contain the H1 and Zeus experiments respectively. Bunches of protons and electrons cross every 96 ns. A schematic picture of HERA and the necessary pre-accelerators is shown in figure 3.1.

During the 1994 HERA running period, the electron beam was operated at an energy of 27.55 GeV with the proton beam at the nominal 820 GeV. HERA operated with 94 electron bunches and 90 proton bunches. Only 84 of these were colliding, the others, called 'pilot bunches', were used to study the interactions of the beams with residual gas in the beampipe ('beam-gas' interactions) and the beampipe itself ('beam-wall' interactions) for background purposes.

3.2 The H1 Detector

Figure 3.2 shows the components of the H1 detector. The detector is designed to enable the study of many of the different physics topics accessible in electron

[1] During 1994 running HERA used positrons and not electrons. In this thesis, the term electron is used generically to include both electrons and positrons

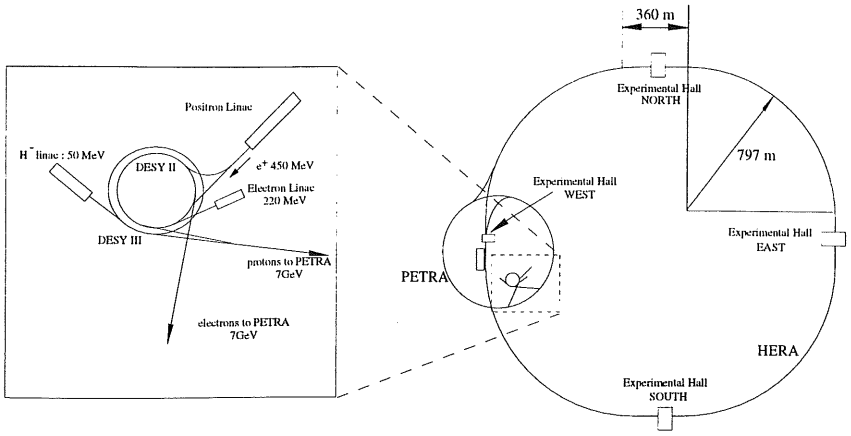

Figure 3.1: A schematic picture of HERA and the necessary pre-accelerators.

proton scattering. The detector is asymmetric due to the asymmetry of the incoming beam energies. The subdetectors in the the backward region of H1 are primarily designed for the accurate identification of the scattered electron and the reconstruction of its kinematics in low Q^2 (< 100 GeV^2) DIS events. Due to the much higher average particle multiplicity in the forward region, there are a larger number of subdetectors in this region.

The following are important features of the H1 detector:

- Accurate calorimetry in the central and forward regions to detect the scattered electron in high Q^2(> 100 GeV^2) DIS events and also for detecting neutral particles which are not detected by the tracking detectors. The high accuracy is also important for calculating the missing mass in Charged Current events involving the production of neutrinos.

- Tracking detectors are used to reconstruct the momentum of particles passing through the detector. This is done by measuring the curvature of the particles in a uniform magnetic field. Accurate tracking information is particularly important in the study of resonances and measurements of energy flow. Information from the trackers can also be used to reject background events.

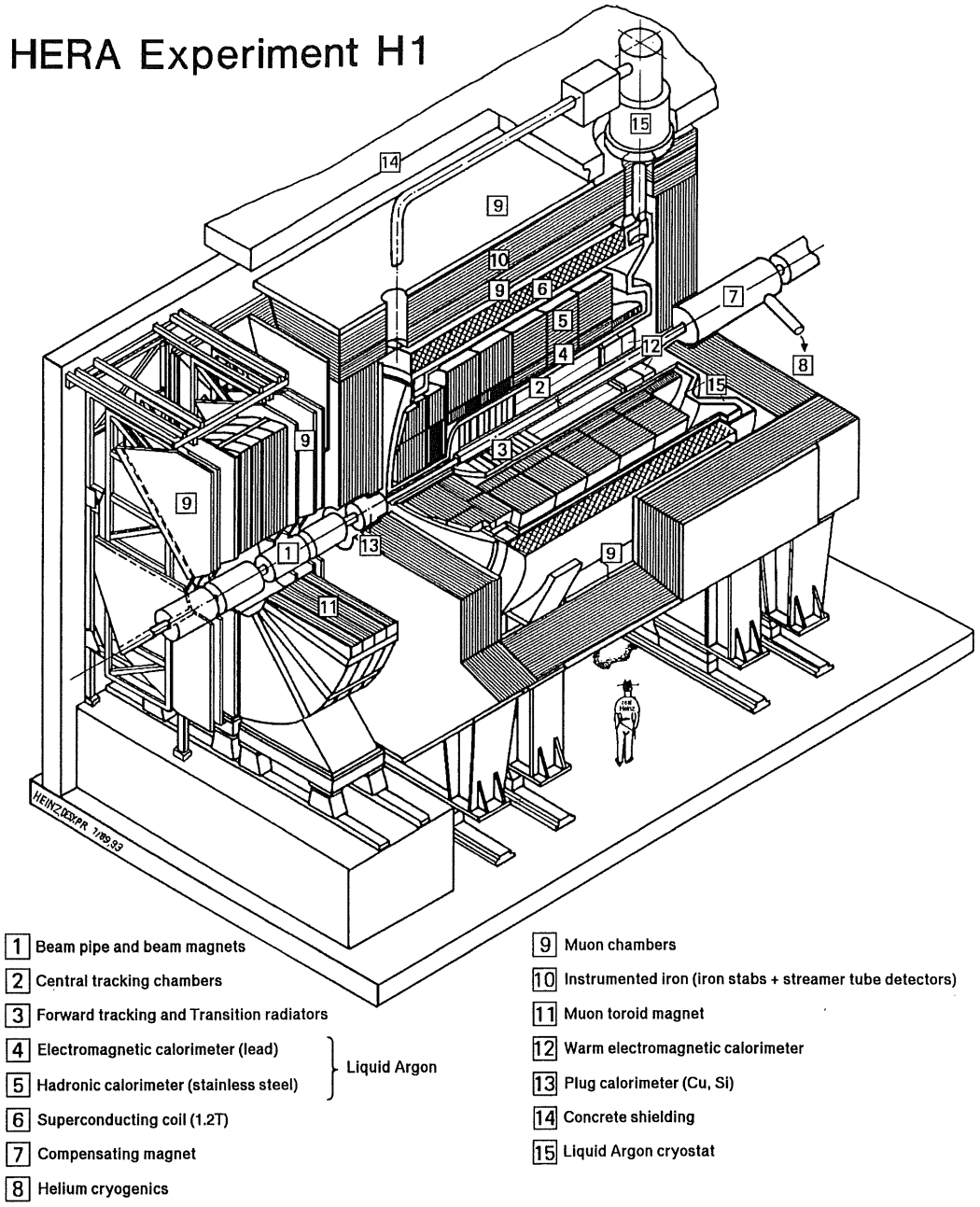

Figure 3.2: The H1 detector.

- H1 has both central and forward muon detectors. The detection of muons allows the identification of heavy flavour decays and also of possible exotics.
- Due to the high rate of collisions at HERA, efficient triggering is required to reject background at an early level and thus keep the dead-time of the detector as low as possible.
- Accurate luminosity measurement allows precise cross-section determinations.

3.3 The H1 Co-ordinate System

The spatial dimensions of detectors and trajectories are described in conventional H1 co-ordinates. Two different systems are used. Firstly, the cartesian co-ordinates (x,y,z) are defined with the z axis being in the direction of the incoming proton beam and the y axis vertically upwards from the origin at the nominal interaction point. The polar co-ordinates (r,θ,ϕ) are also used. Here the polar angle θ is measured with respect to the z axis and the azimuthal angle ϕ is defined with respect to the x axis. Figure 3.3 shows both these definitions.

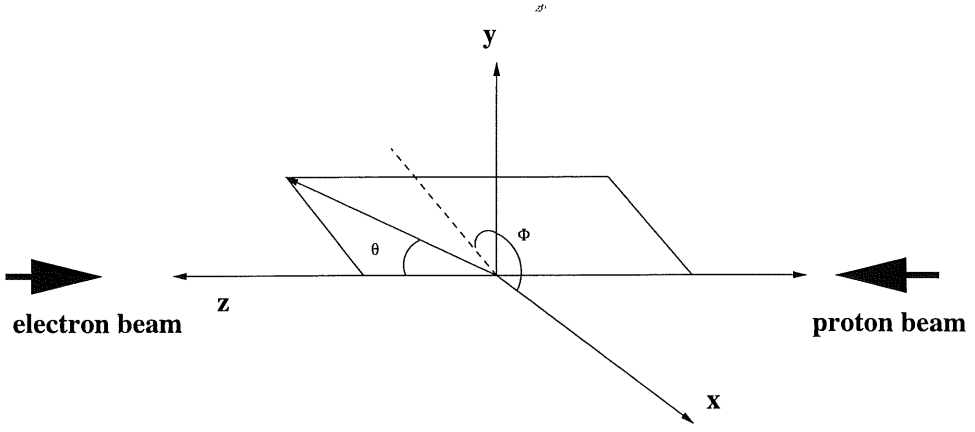

Figure 3.3: The H1 co-ordinate system.

3.4 Tracking at H1

The H1 tracking detectors consist of a combination of drift chambers and proportional chambers. The drift chambers are used primarily for accurate particle position and momentum reconstruction and the proportional chambers for event triggering. Figure 3.4 shows the H1 tracking detectors. The forward tracking detector (FTD) covers the angular range $5° < \theta < 25°$ and the central tracking detector (CTD) covers the angular range $25° < \theta < 155°$. The backward proportional chamber (BPC) covers the angular range $155° < \theta < 174°$ and is used for both triggering purposes and for providing good spatial resolution for tracks in the backward region. Here the efficiency of the central tracker degrades as tracks get closer to the beampipe. The tracking chambers in H1 are situated in a 1.15T magnetic field provided by a superconducting coil which surrounds the liquid argon calorimeter. This field is highly uniform in the tracking volume and varies at most by 2%. The radius of curvature of tracks in this field allows accurate particle momentum measurement.

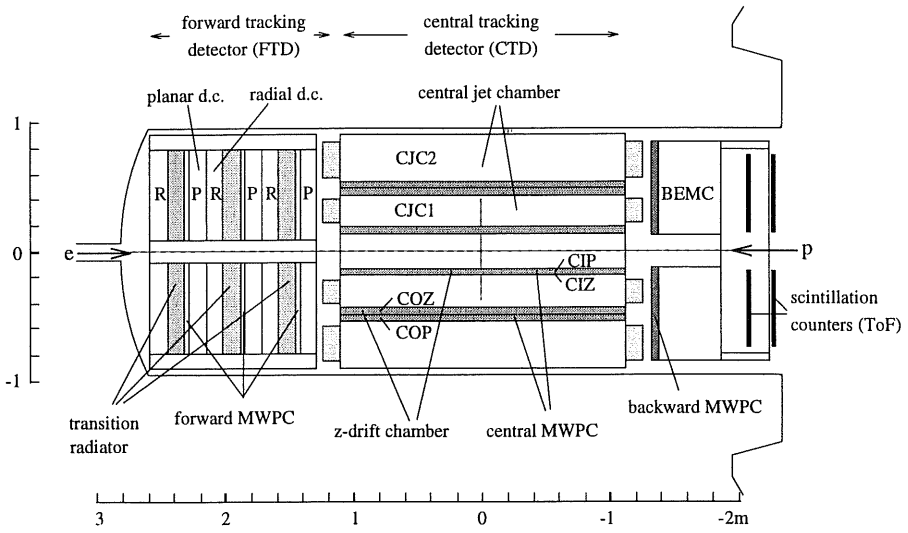

Figure 3.4: A view of the H1 tracking detectors.

3.4.1 Operation of Drift Chambers

Drift chambers consist of gas filled cells containing anode and cathode wires. The anode "sense" wires run through the interior of the cell at a high positive voltage.

The aim is to achieve a region of uniform electric field in the drift space of the chamber and a high field near the anode. This is typically done by placing cathode wires a few cm away from the sense wires and using field shaping wires close to the sense wires or conducting strips on the wall of the chamber. Hence, except for the region very close to the sense wires, the electric field is near uniform.

As a charged particle traverses a cell, it will ionise gas atoms. The electrons produced by this will then drift towards the sense wires and into the region of increased electric field. This high field induces an avalanche of electrons and ions. As the positive ions drift away from the sense wires, a current is induced in these wires which travels along them and is recorded by the read-out system. The spatial position of the track can be accurately determined (within a few hundred μm) using the drift velocity of the electrons in the gas, if the time at which the initial particle crossed the gas volume, t_0, is known. The distance along the sense wire at which the avalanche was induced can be determined by measuring the charge collected at each end of the wire. This method is known as charge division and is accurate to within a few percent of the wire length. For each wire that the particle passes close to, a three dimensional space point can be reconstructed and hence the path of the particle. This reconstructed path is known as a track.

3.4.2 Operation of Proportional Chambers

Multi-wire proportional chambers (MWPCs) work on the same basic ionisation principle as drift chambers. In MWPCs, the anode and cathode wires are much closer together resulting in overlapping avalanche regions and a very high electric field throughout the detector. Hence the drift time is very short, of the order of tens of nanoseconds. For this reason MWPCs are very useful for triggering purposes.

3.4.3 The Central Track Detector

The main track reconstruction in the CTD, shown in figure 3.5, is performed using two large concentric drift chambers, CJC1 and CJC2. To enable more accurate z-information a further two drift chambers, CIZ and COZ, are used. Finally, for triggering on charged tracks in the central region of H1, two MWPCs, CIP and

COP, are used. These six components make up the CTD.

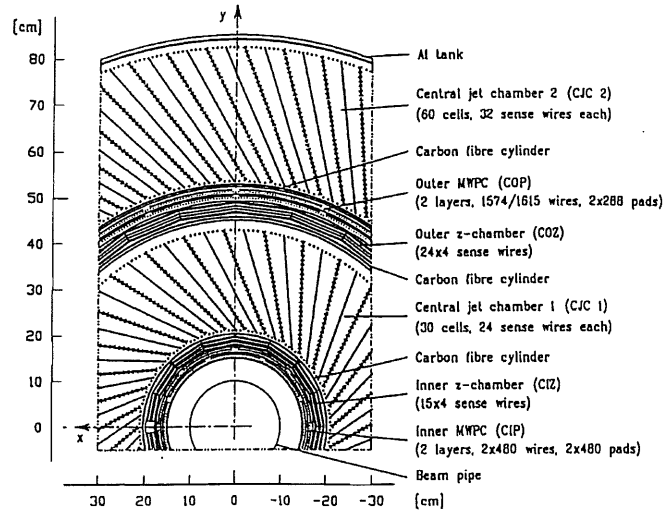

Figure 3.5: Cross-section through the H1 central tracking detectors in the x-y plane.

The Central Jet Chambers

The central jet chambers, CJC1 and CJC2, cover most of the volume of the CTD. The sense wires are placed parallel to the beam axis with adjacent cathode wire planes defining the cell boundaries. The cells are tilted at an angle of 30^o with respect to the radial direction. This ensures optimal track resolution and also ensures that high momentum tracks will traverse a sense wire plane in each jet chamber, thus reducing the left-right drift chamber ambiguity. CJC1 contains 30 cells in ϕ each containing 24 sense wires per cell. CJC2 has 60 cells each with 32 sense wires. As both ends of the sense wires are read out, charge division can be used to give a z-measurement. A space point resolution of 170 μm in the r-ϕ plane and a resolution of 1% of the sense wire length in z have been achieved in CJC1 and CJC2 [50]. Particle identification can be made using dE/dx, the energy loss per unit length of the track, which is dependent on the velocity of the particle.

The z Chambers

The inner and outer z-chambers, CIZ and COZ, are used to obtain a more accurate z position measurement. The z chamber drift cells contain four sense wires at the same z and at different radii and are positioned around the beam axis in a ring forming, in the case of the COZ, a 24-sided polygon containing 24 cells and, in the case of the CIZ, a 16 sided polygon composed of 15 drift cells. The drift time gives a measurement of the z position and charge division gives a measurement of the ϕ position.

The Central MWPCs

The central inner and outer proportional chambers, CIP and COP, are used to trigger on tracks which point to the nominal interaction region. Each chamber consists of two concentric layers with anode wires running parallel to the beam direction. Read out is via cathode pads. In the CIP, each pad is 36.6 mm long in z and one layer is rotated by half a pad with respect to the other to give increased ϕ resolution. In the COP a similar design is used with each pad having a length of 120 mm in z.

3.4.4 The Forward Track Detector

The FTD was designed to reconstruct tracks in the forward direction of H1. The FTD consists of three supermodules each containing planar drift chambers, an MWPC, a transition radiator and a radial drift chamber.

Planar Chambers

Each planar module consists of three planar drift chambers. Each of these contains four planes of sense wires at different z. Each planar drift chamber is rotated by 60^o in ϕ with respect to the next chamber. The sense wires are read out at one end only with the information from all three chambers needed to obtain an accurate x-y co-ordinate.

Forward MWPCs

The FMWPCs (Forward Multiwire Proportional Chambers) serve a similar purpose to the MWPCs in the CTD, namely triggering on charged tracks. Each module contains two anode wire planes and two cathode pad planes. Again, the cathode pads are read out. The radial size of the cathode pads varies with the radius of the chamber. The pads cover 45^o in ϕ except for the outermost pads which each cover 22.5^o. To improve the resolution in ϕ, the pads of subsequent chambers in a module are staggered by half a pad radius.

Radial Chambers

The radial chambers consist of wedge shaped drift cells. Each has 48 cells in ϕ. Each cell contains 12 sense wires strung radially resulting in the maximum drift time varying with the chamber radius. The sense wires are staggered around the central plane of each wedge to remove the left-right drift ambiguity. Field shaping wires are placed between the sense wires. As both ends of the sense wires are read out, the radial co-ordinate can be deduced from charge division. Particle identification using dE/dx can be performed using the drift chambers.

3.4.5 The Backward Multi-Wire Proportional Chamber (BPC)

The BPC is used both for triggering and space point reconstruction in the backward region of H1. It consists of four sets of anode wire planes and five sets of cathode pad planes. The anode wires are oriented at 45^o with respect to each other and these are read out. Accurate space point resolution using the BPC is essential in reconstructing electron kinematics. This is possible by using the coincidence of hits in three or four of the four anode planes in combination with the reconstructed event vertex. The precision of the electron scattering angle measurement attained using this method is 5 mrad.

3.5 Calorimetry at H1

With the exception of the luminosity calorimeters, all calorimeters in H1 are sampling calorimeters. These consist of a material which causes a particle to shower and a sensitive material in which the shower development is measured. The charge, or light in the case of the BEMC, collected in the sensitive region is dependent on the amount of energy deposited there and hence the energy of the initial particle.

Calorimetry works differently for electromagnetic and hadronic particles. When an electron or photon interacts with an absorber, further electrons and photons at lower energy are produced by bremsstrahlung and pair production. Such interactions result in the production of a shower of particles. When the produced particles have energy below some threshold, the "critical energy", their energy will be dissipated by ionization and excitation rather than the production of more particles. If the shower is fully contained, the energy of the incident particle can be determined by measuring the total ionization. The longitudinal development of an electromagnetic shower is dependent on the radiation length of the material it traverses, X_0. This is defined as the distance over which a high energy electron loses, on average, all but 1/e of its initial energy.

When a hadron interacts with matter, most of its energy is lost to inelastic nuclear collisions forming more hadrons which go on to cause a shower. The dimension of a hadronic shower is determined by the nuclear absorption length, λ_I, of the material, typically much larger than the radiation length. Therefore, for good shower containment, hadronic calorimeters are typically much larger than electromagnetic calorimeters. A large amount of the energy from a hadronic shower is lost in the break-up of nuclei and results in low energy photons which go undetected. Thus, most calorimeters provide a better response for electromagnetic particles than for hadrons.

There are four calorimeters in the main H1 detector, the Liquid Argon Calorimeter, the Backward Electromagnetic Calorimeter, the Tail Catcher and the Plug calorimeter. These are shown in figure 3.6.

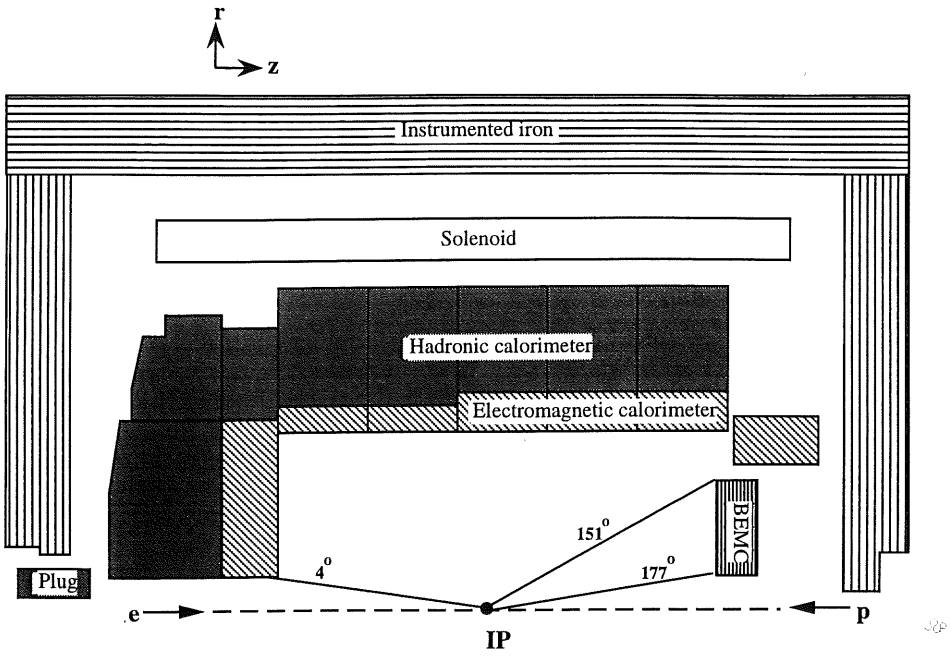

Figure 3.6: A view of the H1 calorimeters.

3.5.1 The Liquid Argon Calorimeter

The Liquid Argon Calorimeter provides calorimetry around the majority of the polar angle range of H1, $4^o < \theta < 153^o$. There are two sections to the calorimeter, the electromagnetic (EMC) and hadronic (HAC) sections. The design of the calorimeter required a stable response and good granularity for efficient shower separation. The liquid argon technique [51] was therefore used.

In the EMC, the absorber consistes of 2.4 mm thick lead plates. The gaps between these plates define the sampling liquid argon volume. Each gap contains a plane of copper readout pads to collect the charge produced by the shower. The total thickness of the EMC varies between 20 and 30 radiation lengths and the resolution is $\sigma_E/E \approx 12\%/\sqrt{E} \oplus 1\%$ [52].

In the HAC, the absorber consists of 19mm thick stainless steel plates with the sampling medium consisting of two gaps of liquid argon seperated by readout pads. The depth varies between 5 and 7 nuclear absorption lengths and the resolution is $\sigma_E/E \approx 50\%/\sqrt{E} \oplus 2\%$ [52].

Both sections of the calorimeter are highly segmented. Thus, electromagnetic and hadronic showers can be separated by using the different shower shapes and separate calibration corrections applied. The high level of segmentation also allows the simple identification of noise. There is an uncertainty in the absolute energy scale of the calorimeter. For 1994 data this was $\approx 3\%$ for the EMC and $\approx 5\%$ for the HAC [52].

3.5.2 The Backward Electromagnetic Calorimeter (BEMC)

The BEMC covers the angular range $151^o < \theta < 177^o$ and is designed primarily to measure the energy of the scattered electron in low Q^2 ($Q^2 < 100$ GeV^2) DIS events.

The absorber in the BEMC consists of 2.5mm of lead with the sampling medium being 4mm thick scintillator. There are in total 50 layers of scintillator and 49 layers of lead. The BEMC is segmented in $x-y$ into 88 stacks. The signal from the scintillators is read out via wavelength shifters at the sides of the stacks which feed into photodiodes at the rear of the detector.

The BEMC has a depth of 22.5 radiation lengths which corresponds to less than one nuclear absorption length. Hence, while electromagnetic showers are well contained in the detector, hadronic showers will only deposit typically around 45% of their energy in the BEMC.

The resolution of the BEMC for electromagnetic particles is $\sigma_E/E \approx 10\%/\sqrt{E}$ and for hadrons, when combining the BEMC output with that of the tail-catcher, is $\sigma_E/E \approx 80\%/\sqrt{E}$ [10].

Figure 3.7 shows a cross-section of the BEMC.

3.5.3 The Plug Calorimeter

The plug calorimeter is designed to cover the angular region between the beampipe ($\theta \approx 0.6^o$) and the edge of the liquid argon calorimeter ($\theta \approx 3^o$). It is used as a veto for diffractive events, in which a rapidity gap is expected in this region.

The plug consists of eight layers of silicon detectors alternating with layers of

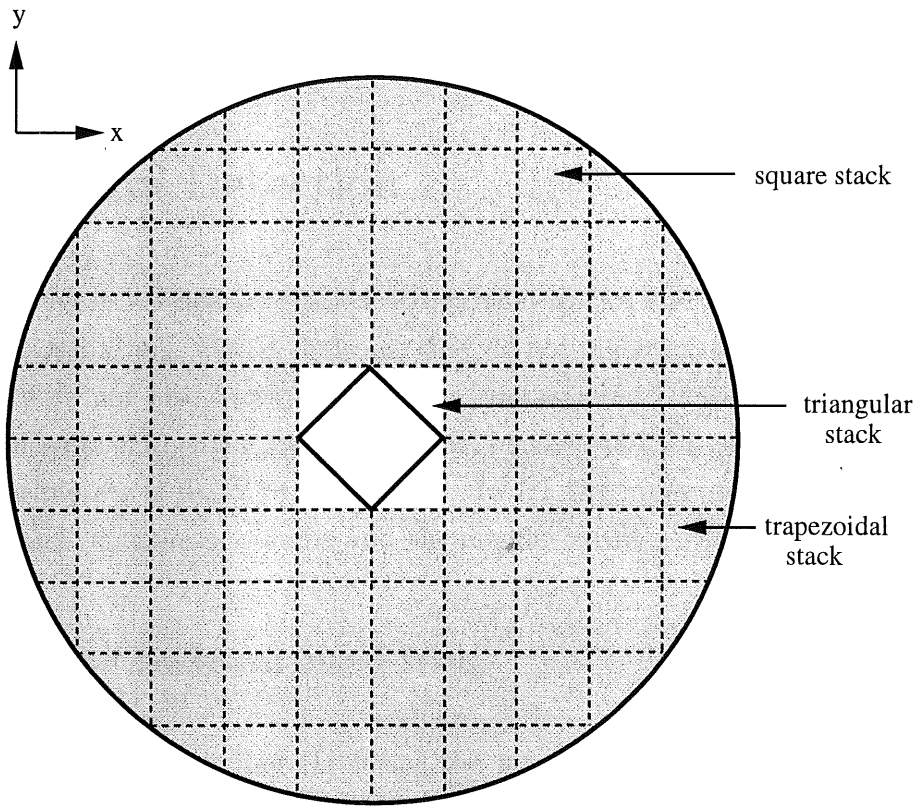

Figure 3.7: The stack structure comprising the BEMC.

copper. Due to a large energy leakage and a large amount of dead material in front of it, the plug has a hadronic energy resolution of $\sigma_E/E \approx 150\%/\sqrt{E}$ [53].

3.5.4 The Tail Catcher

Within the iron return yoke, there are sixteen layers of streamer tubes used primarily for muon detection. Eleven of these are equipped with readout pads and are used to measure the energy of hadrons which escape detection in the liquid argon calorimeter or the BEMC. The tail catcher has a resolution of $\sigma_E/E \approx 100\%/\sqrt{E}$.

3.6 Muon Detection

Because muons are heavier than electrons, they do not lose as much of their energy via bremsstrahlung. Unlike hadrons, they do not undergo strong interactions and therefore do not lose energy via nuclear interactions. Hence they can penetrate large amounts of material and any charged particle which has penetrated the main H1 calorimeters is likely to be a muon. In H1 the muon detectors are situated outside the calorimeter volume and the magnetic coil.

3.6.1 The Instrumented Iron

The iron yoke surrounding H1 forms the return yoke for the magnetic field of the H1 solenoid and is the main structural component of the detector. The iron is instrumented with 16 layers of Limited Streamer Tubes (LSTs) interleaved with 10 layers of iron. These form the central muon system which covers the polar angle range $6^o < \theta < 172^o$ and can reconstruct muons with energy above a threshold of about 1.2 GeV.

The LSTs are oriented in the z direction in the barrel and the x direction in the end-caps. Each LST consists of a 10 mm $\times$ 10 mm plastic tube with a single wire running through the middle. Five of the layers also have cathode strips perpendicular to the wires. The remaining 11 layers have cathode pads allowing calorimetric readout. Track reconstruction in the central muon system

uses primarily the wires and the strips. Information from the pads is used to solve ambiguities.

3.6.2 The Forward Muon System

The forward muon detector (FMD) covers the polar angle range $3^o < \theta < 17^o$ thus providing an overlap with the instrumented iron. The FMD consists of two sets of three planes of drift chambers either side of a toroidal magnet. Each plane consists of a double layer of 12 cm-wide cells, staggered by half a cell width to remove the problem of left-right drift ambiguities. On each side of the toroid there are two planes with drift cells arranged azimuthally, to measure θ accurately, separated by a plane with drift cells arranged radially to enable accurate ϕ reconstruction. The FMD can reconstruct muons with energies between 5 GeV and 200 GeV. Muons with too small energy will not reach the FMD and muons with too high an energy will result in too little bending by the toroidal magnet for accurate momentum reconstruction.

As well as reconstructing muons, the FMD has proved to be sensitive to interactions of forward going particles with the beam pipe and surrounding material. This makes the FMD useful in the identification of diffractive events where there is a large forward rapidity gap.

3.7 Scintillators

3.7.1 The Time-of-Flight and Veto Walls

The time-of-flight (ToF) and veto wall counters are used to distinguish between genuine *ep* interactions and beam-induced background. The backward ToF (BToF) consists of two scintillator planes at z = -1.95 m and z = -2.25 m which cover 127 $\times$ 127 cm in the $x - y$ plane. The forward ToF (FToF) is smaller and is situated at $z \approx 7$ m. If the proton beam interacts with gas in the beam pipe or the beam pipe itself, particles produced will hit the BToF at the same time as the proton beam passes. If a genuine *ep* interaction occurs, the produced particles will register in the BToF at the same time as the electron beam passes, 13 ns later. The FToF works in a similar way in detecting interactions of the electron

beam. Because of the good time resolution of the scintillators, $\sim$ 1 ns, timing of signals in the ToF detectors can be used, via the L1 trigger, to veto beam induced background. There are two veto walls, the inner wall at z=-6.5 m and 100 $\times$ 90 cm^2 in xy and the outer wall at z = -8.1 m and 5 $\times$ 4 m^2 in $x-y$. The veto wall detects penetrating particles associated with the proton beam.

3.7.2 The Proton-Remnant Tagger

The proton-remnant tagger (PRT) is a set of seven scintillators situated around and between the proton and electron beam pipes at z = 24 m. The PRT is designed to detect particles at very small angles produced in the dissociation of the proton. It therefore provides discrimination between diffractive events in which the proton is scattered elastically or inelastically. Each scintillator consists of two sheets of plastic scintillator connected to a photomultiplier. A signal is registered in a scintillator if a signal from both sheets arrives at a coincidence detector within a time window of 15 ns and the timing is consistent with that expected from the proton remnant.

3.8 The Luminosity System

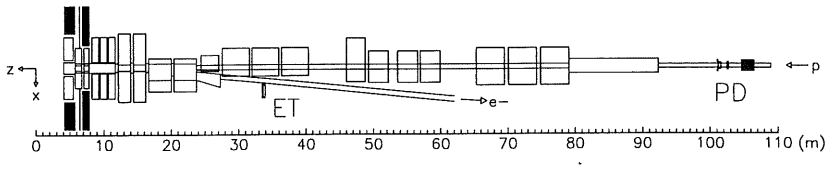

Figure 3.8: The dimensions of the H1 luminosity system.

To measure cross-sections for any process, the luminosity of the incident beams must be well known. In H1 the beam luminosity is measured using the Bethe-Heitler process, $ep \rightarrow ep\gamma$, the cross-section for which is known accurately [54]. The electron and photon are detected in coincidence by two systems of Čerenkov counters, the electron tagger (ET) and the photon detector (PD). Due to the

angular distribution of the scattered electron in this process, these detectors are situated near the beamline and far from the interaction point. Figure 3.8 shows the luminosity system. The ET is situated at z = -33.4 m and the PD is situated at z = -102.9 m.

To protect the PD from synchrotron radiation, it is preceded by a layer of lead. A water Čerenkov counter is also included to veto events in which a photon has converted in the lead. The largest background to the Bethe-Heitler process is bremsstrahlung from residual gas is the beam pipe. This background is measured using electron 'pilot' bunches, which only interact with beam gas, and corrected for in the luminosity measurement. This background was measured to be $\sim$ 10% for 1994 data taking. The statistical error on the luminosity measurement is negligible. The systematic error for 1994 data taking is estimated to be $\sim$ 1.5% [10].

As well as accurately measuring the luminosity, the luminosity system can be used to study photoproduction. For very low Q^2 events ($Q^2 < 0.01$ GeV^2) the electron is scattered at very low angles and can be detected in the electron tagger. The event kinematics can be reconstructed from the electron energy measurement.

3.9 Triggering at H1

Triggering is very demanding at HERA due to the short time between bunch crossings, 96 ns. In comparison to this time, the maximum drift times of the CJC chambers are $\sim$ 1 μs and the integration time of the calorimeter preamplifier is 1.5 μs. In all it takes around 1 ms to read out all the detectors in H1. This means that when an event is read out, the detector will miss any interactions during the next 10^4 bunch crossings. Therefore, very careful selection of which events to keep has to be made.

The H1 trigger consists of four levels. During 1994 running, only the first (L1) and fourth (L4) levels were operational. A pipelined read-out system is used so that all detector information is kept until a decision is made at L1. The decision signal L1KEEP is available around 24 bunch crossings after the original interaction. The individual detector pipelines are therefore between 27 and 35

bunch crossings in length to allow the full information from any event kept to be read out. Following an L1KEEP, the detector is unable to process further events for a period of 1-2 ms. To reduce this 'dead time' in subsequent years, two further levels of triggers, L2 and L3, are designed to abort the read-out after further selection criteria.

Information from most of the H1 detectors is available for the L1 trigger. Each signal passed from the various sub-detectors is called a 'trigger element'. Trigger elements include things like signals in the ToF detectors, a vertex reconstructed by the MWPCs, a signal in the central or forward muon systems or tracks in the CJC chambers. The BEMC trigger elements are described in more detail later. Many trigger elements, such as those from the ToF detectors or the z-vertex position from the MWPCs, are used to veto background due to non-ep interactions. It is important to identify the "t_0" of the bunch crossing for the event being considered to allow track reconstruction and accurate calorimeter energy measurements. Some detectors, the MWPCs and scintillators for example, have intrinsically good time resolution, less than the time between bunch crossings. Other detectors can have signals which extend over more than one bunch crossing. Therefore, to identify the correct t_0, these trigger elements are required to be in coincidence with trigger elements from the former class.

The central trigger logic (CTL) combines trigger elements to produce, in total, 128 'subtriggers' tailored for different physics analyses. Some subtriggers are used purely for monitoring the efficiency of the physics triggers. Also included is a random trigger which is used to study detector noise.

Events kept at L1 are then subject to the L4 'filter farm'. This consists of software running some of the subroutines of the off-line event reconstruction package H1REC [50]. This can reconstruct tracks and calorimeter clusters. The L4 farm applies cuts based on these reconstructed quantities to reject background events. It will also reject events which were triggered by noise in the L1 subtriggers by verifying the L1 decision on the basis of the reconstructed quantities. In total approximately 70% of events accepted at L1 are rejected at L4, mainly due to beam-gas and beam-wall interactions.

3.10 Simulation at H1

Computer simulation is a vital part of any H1 physics analysis. To produce a cross-section for any process the overall detector acceptance and efficiency must be known. This is nearly always estimated using Monte Carlo generated events subjected to the standard H1 simulation. The aim is that the generator produces distributions of particle momenta and directions as close as possible to those in the data used for the analysis and the simulation in turn produces output as close as is possible to the actual detector responses.

Monte Carlo events are generated in three stages:

- An event generator, particular to the process under study, is run to produce simulated events with particles distributed according to the kinematic distributions expected for the process.

- The resulting energy depositions of the particles in the various detector components are simulated, as are the signals these cause in the detector.

- The output from the second stage is reconstructed in the same way as the real data to give the resulting response of the detector components.

These three stages result in simulated events which can be subjected to the same analysis chain as the data.

Chapter 4

Event Selection

4.1 Introduction

This chapter describes the event selection procedure used to isolate the ρ' and ρ samples used for analysis.

The data used in this analysis were taken during the 1994 running period of the HERA *ep* collider using the H1 detector. After trigger requirements and off-line selection the data used correspond to a luminosity of ~ 2 pb^{-1}.

4.2 Trigger

4.2.1 The Level 1 Trigger

The first selection performed on events recorded by the H1 detector is the L1 trigger requirement. For events in which the scattered electron is found in the BEMC, the BEMC single electron trigger (BSET) is used [55].

The energy of each stack in the BEMC is determined from the sum of the signals in the wavelength shifters at the side of the stack. The stack energies are then compared to two thresholds, one just above noise levels (~ 1.3 GeV) and one used as a cluster seed (~ 2.3 GeV). The stacks with energy above the latter threshold are then combined with neighbouring stacks with energy above the lower threshold to form clusters.

The BSET trigger element used in identifying an electron candidate requires that the most energetic cluster formed is above a threshold energy of 7 GeV. The efficiency of the BSET trigger is around 100% for electrons with energy above 10 GeV in the main part of the BEMC. However, there are triangular BEMC stacks close to the beam pipe in which the BSET trigger efficiency is lower and not well simulated.

4.2.2 The Level 4 Trigger

Events which pass cuts at L1 are passed to the L4 filter farm. Here tracks and clusters are reconstructed using a fast version of the H1 reconstruction software, H1REC [50]. Subsequent selection is then applied to remove remaining background events. Algorithms are applied to the reconstructed quantities depending on which L1 subtrigger kept the events.

The main background removed at L4 is that in which the incoming proton beam interacts with beam-gas or the beam-wall. Here the tracks will point upstream of the detector and not towards the nominal interaction point. Several algorithms are applied at L4 to reject these events.

An additional background exists for events triggered by the BSET trigger. These 'single diode' events occur when a large proportion of the energy of the cluster is collected in a single wavelength shifter. These largely occur due to a photon originating from synchotron radiation hitting a photo-diode. To reject these events, the maximum fractional energy within a single diode is limited to 95%.

4.3 Event Reconstruction

Following selection at L4, remaining events are reconstructed fully using H1REC. As the results presented here are primarily derived from the measured quantities of the scattered electron and charged tracks, this section describes the reconstruction process used for the BEMC and the Central Tracking Detectors.

4.3.1 The BEMC

In the BEMC no noise supression is carried out at the cell level. The cell noise level follows a gaussian distribution. Any cell above a threshold of 3 σ deviation from the typical noise level (around 400 MeV) is classed as a cluster seed and all 8 neighbours of the seed are joined to form a cluster. Any cells in the overlap between clusters are classed as individual clusters.

4.3.2 The Central Tracking Detectors

Reconstruction of tracks in the central tracking detectors uses information from the CJCs and the z-chambers. The position along the wire is given by charge division at the ends of the wire. The time is measured from the leading edge of the pulses. Hence the drift co-ordinate can be evaluated.

Track finding involves several stages. Short track segments are found from triplets of hits on adjacent wires. Triplets with common hits are then joined to form chains of hits which are stored as track segments. Helix parameters are then measured and track segments with similar parameters are merged. The most likely combinations are formed first and segments already assigned to a track are then not re-assigned. Hits which are not assigned to a track are examined and assigned to the nearest track with which they are compatible. Finally, hits for which the measured and expected drift times are incompatible are then rejected. Very short track candidates are rejected unless they start in the first few wires of a ring to guard against cases where the hits from one particle cause the reconstruction of two tracks in the CJC.

4.4 Off-line Event Selection

After selection criteria are applied on-line by triggering requirements, further cuts are applied off-line to try and isolate genuine ρ' and ρ events from the remaining background. Thus two event samples are selected, one for each type of meson, to enable the cross-section ratio to be computed.

4.4.1 Run Selection

Only runs taken with the following conditions are used for this analysis:

- Any run in which one of the main H1 detector components was not working is excluded.

- Any run in which the BSET trigger was pre-scaled is excluded.

4.4.2 Electron Selection

Electron selection is required to remove background due to photoproduction. Here the exchanged photon is quasi-real ($Q^2 \approx 0$) and the electron, due to the small momentum transfer, passes down the beampipe. In some cases it is possible for other processes to mimic the electron cluster in the BEMC. Thus the following selection is used for both samples to ensure a good electron is found:

- The energy of the most energetic cluster in the BEMC is required to be greater than 12 GeV. This cluster is then considered to be an electron candidate. This reduces the likelihood of a photoproduction event passing the selection criteria.

- The radius of the BEMC cluster is required to be less than 5 cm. This reduces the background which occurs due to hadronic particles causing clustering in the BEMC in photoproduction events. Hadronic showering will lead to larger cluster radii.

- The centre of gravity of the cluster is required to be within 5 cm of the extrapolation of the electron trajectory determined by the reconstructed event vertex and a hit in the BPC. Typically, there may be multiple hits reconstructed in the BPC. In events where this is the case, the hit closest to the centre of the cluster is used to reconstruct the event kinematics. This criterion ensures that the same particle causes the cluster and the BPC hit and removes events which are triggered due to $\pi^0 \rightarrow \gamma\gamma$ decays which will not produce BPC hits.

- To ensure that the electron is well contained in the BEMC it is required to be at an angle $\theta > 156°$.

No selection is included to exclude the triangular BEMC stacks near to the beam pipe. Here the BSET trigger efficiency is not well simulated. Those events with the electron tagged in these stacks are included to greatly increase the statistics used for the cross-section ratio measurement. Here the trigger efficiency cancels and is not required to be accurately known.

Figures 4.1 and 4.2 show the electron energy and polar angle distributions for the selected events in both samples. In each case a Monte Carlo comparison normalised to the observed number of events is shown.

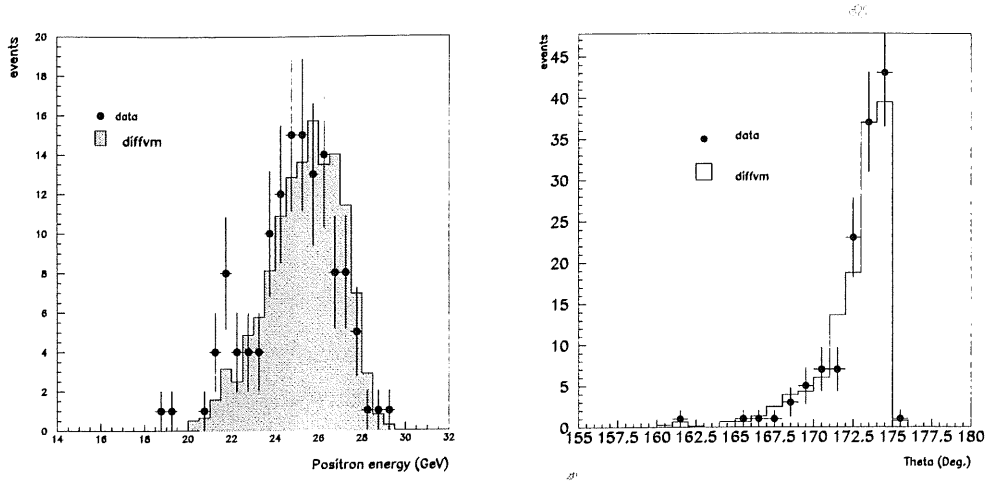

Figure 4.1: Reconstructed electron energy and polar angle distributions for selected ρ' events with Monte Carlo comparisons.

4.4.3 z Vertex Requirement

The event vertex is determined from the reconstructed tracks. In practice, the position of the vertex in the x-y plane is stable over a number of runs and determined from high momentum tracks. The z position of the vertex, however, varies event by event. Using the well constrained x-y position, tracks are fitted in the r-z view to find the z position of the vertex. The z vertex position follows a gaussian distribution around the nominal position due to the size of the proton bunches. Figure 4.3 shows the distribution of the z position of the reconstructed event vertex for both the selected event samples, each with a Monte Carlo comparison using DIFFVM. During 1994 running, the nominal z vertex

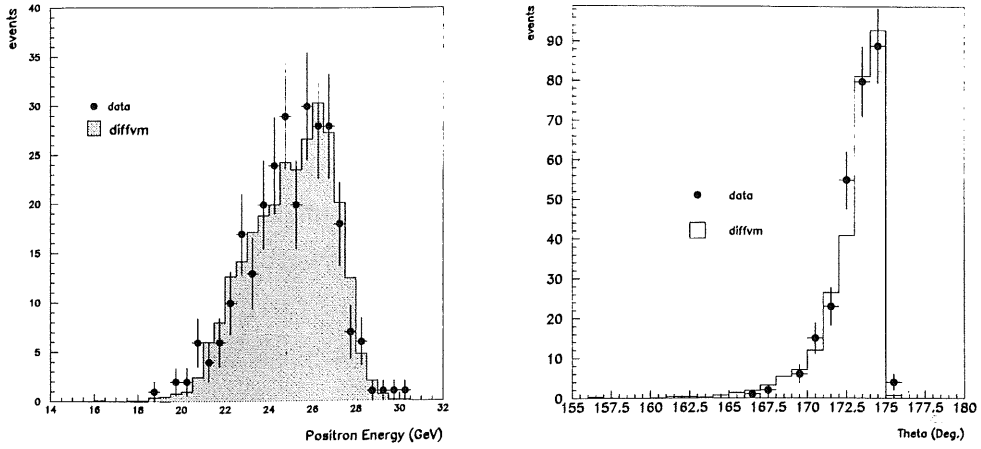

Figure 4.2: Reconstructed electron energy and polar angle distributions for selected ρ events with Monte Carlo comparisons.

position was around $z = 5$ cm. If any significant beam-gas background remained in the sample, a flat distribution in z-vertex would be observed for these events. Figure 4.3 shows that any remaining such background is negligible.

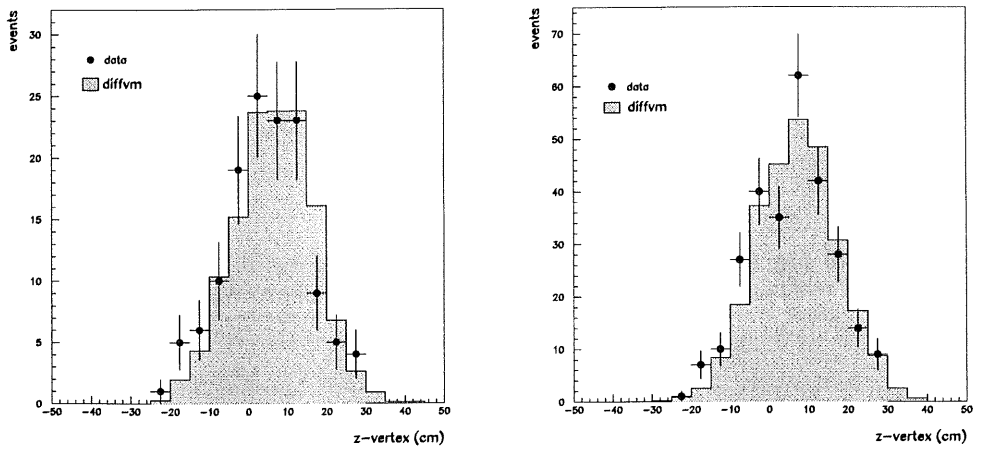

Figure 4.3: z-vertex distribution of selected events for a) the ρ' sample and b) the ρ sample with DIFFVM Monte Carlo comparisons

4.4.4 Longitudinal Momentum Balance Requirement

As an additional background constraint, the quantity $\delta = \sum_i E_i - P_{zi}$, reconstructed from the scattered electron and charged tracks in the event, is required to be in the range 45 GeV $< \delta <$ 65 GeV. This quantity is conserved in the interaction and should be twice the incoming electron momentum. For events where a particle is lost in the beam-pipe in the electron direction, this will not be the case. Figure 4.4 shows the distribution in δ of the events in each sample accepted by all other cuts with a Monte Carlo comparison. The data peak at around 55 GeV as expected. However, there are some events which fall somewhat below this value. This is most probably due to a particle going undetected in these events. This can happen, for example, when the incoming electron radiates a photon, which escapes down the beam pipe, and hence loses some of its energy.

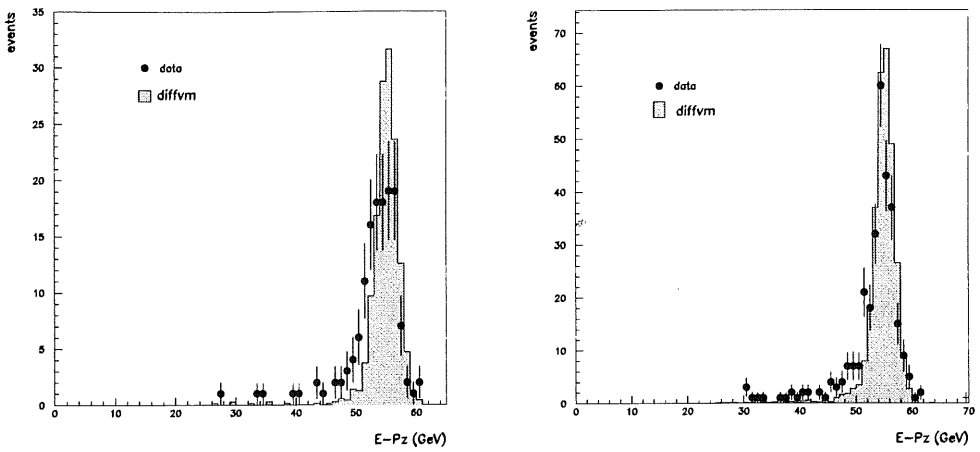

Figure 4.4: δ distribution of selected events for a) the ρ' sample and b) the ρ sample with DIFFVM Monte Carlo comparisons

4.4.5 Forward Selection

As we wish to study the quasi-elastic meson production mechanism we need to discard those events in which the proton dissociates. To do this the information from the forward detectors is used in a now well established technique. When particles are produced in the forward region, at angles outside the acceptance of

the Liquid Argon Calorimeter, they can collide with dead material, for instance the beam pipe, and scatter secondary particles into the forward detectors. Thus, by requiring little or no activity in the forward detectors, events in which the proton dissociates can be rejected. The following selection has been found to be efficient in rejecting these events, [56] :-

• Events where two or more hit pairs are reconstructed in the pre-toroid layers of the forward muon detector are rejected. The FMD suffers slightly from noise, mainly in the electronics of the readout system. By requiring pairs of hits in a layer, randomly distributed noise hits will not lead to an event being rejected.

• Events where there are any hits in the first three layers of the proton remnant tagger are rejected. The proton remnant tagger suffers very little from noise and hence the requirement of no hits can be used.

4.4.6 Treatment of the Hadronic Final State

Events in which there are only four charged tracks in the central detector are required as candidate ρ' events. Thus the following selection is applied to the remaining sample:

• An algorithm is applied to the liquid argon cluster information to remove energy deposits due to noise. This is done by removing clusters with energy below a threshold limit of 300 MeV in the central region of the calorimeter unless they are within 30 cm of any other cluster above 100 MeV. For the forward region of the calorimeter the thresholds are raised to 700 MeV and 500 MeV respectively due to these cells suffering more noise.

• The remaining CJC and liquid argon information from each event is then categorised as a mixture of tracks and clusters. This is done by first removing the clusters associated with the tracks. The track vectors are extrapolated into the calorimeter and then any clusters within a cylinder of radius 40 cm around the track are removed.

• The charged primary vertex fitted hadronic tracks in the final state are required to have the correct multiplicity, four for the ρ' sample and two for the ρ sample. The summed charge of these tracks is required to be zero. All tracks are

required to be within a theta range of $20^o < \theta_{track} < 160^o$ and have a minimum p_t of 100 MeV. These cuts ensure that the tracks are in a region in which the track reconstruction efficiency is well understood and well described by Monte Carlo. The methods of estimating the efficiency for reconstructing tracks using these cuts are described in chapter 6. Figures 4.5 and 4.6 show the p_t and θ_{track} distributions of the tracks in the two selected samples with, in each case, a DIFFVM comparison normalised to the number of observed events.

• After application of the noise removing algorithm and track-cluster matching any events with additional liquid argon clusters above an energy threshold of 100 MeV are removed to get rid of events containing neutral particles.

• As a further veto on events with additional neutrals, the magnitude of the reconstructed t of the event is required to be less than 0.6 GeV^2. Thus events with a large amount of missing transverse momentum are rejected.

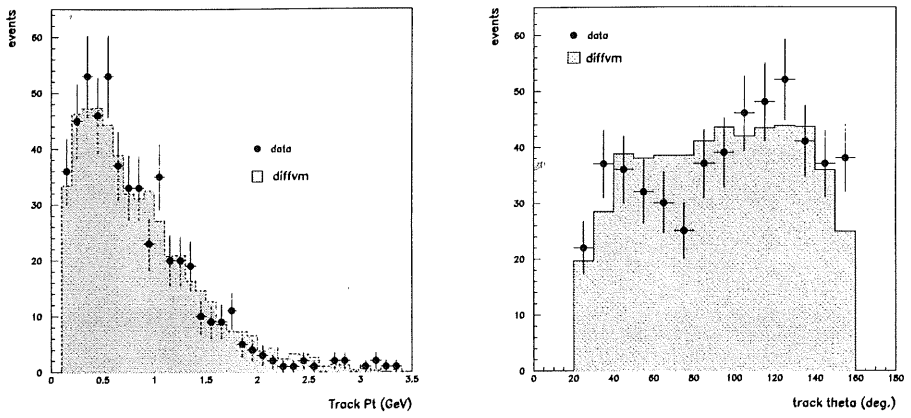

Figure 4.5: a) track p_t and b) track θ for tracks in the selected ρ' sample with DIFFVM comparison.

4.4.7 Invariant Mass Requirements

When computing the cross-section ratio, the ρ' and ρ samples are limited to invariant mass values around the nominal masses of the resonances. This is required to restrict the measurement to mass regions where the resonance signal dominates over background. The invariant masses are obtained from the final

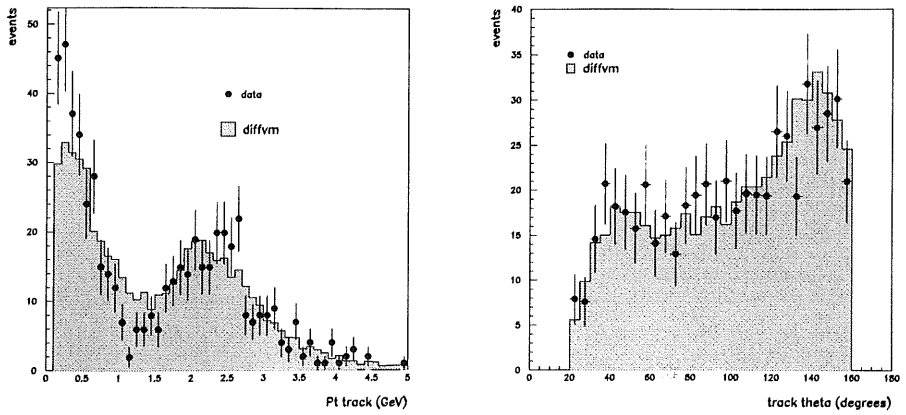

Figure 4.6: a) track p_t and b) track θ for tracks in the selected ρ sample with DIFFVM comparison.

state system, the 4 tracks in the case of the ρ' sample and the 2 tracks for the ρ sample. The masses are required to be in the ranges $1.2 < M_{\rho'} < 1.9$ GeV and $0.6 < M_{\rho} < 1$ GeV respectively. As an additional requirement for the 2 track sample, to exclude any background due to diffractive ϕ production, the invariant mass of the two tracks when treating both particles as kaons is required to be in the range $m_{K^+K^-} > 1.04$ GeV.

4.4.8 Kinematic Reconstruction

The relevant kinematics can be reconstructed in H1 from the measured scattered electron energy E' and polar angle θ_e using the following equations:

$$Q_e^2 = 4EE' \cos^2 \frac{\theta_e}{2}$$

$$y_e = 1 - \frac{E'}{E} \sin^2 \frac{\theta_e}{2}$$

where E is the incident beam energy. However, in exclusive vector meson production it is more accurate to use the quantities θ_e and the polar angle of the meson, γ. This method is known as the double angle method and leads to the following formulae for Q^2 and y [57]:

$$Q_{da}^2 = 4E^2 \frac{\sin\gamma \cdot (1 + \cos\theta_e)}{\sin\gamma + \sin\theta_e - \sin(\gamma + \theta_e)}$$

and

$$y_{da} = \frac{\sin\theta_e \cdot (1 - \cos\gamma)}{\sin\gamma + \sin\theta_e - \sin(\gamma + \theta_e)}.$$

Figures 4.7 and 4.8 show the resolution in Q^2 and y obtained from Monte Carlo simulation using the double angle method. As a comparison, the resolution obtained using the electron method is also shown.

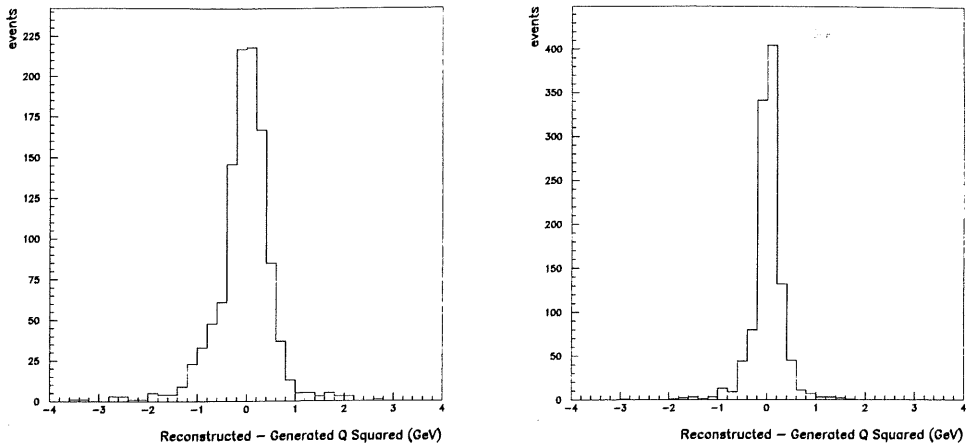

Figure 4.7: Resolution in Q^2 obtained from Monte Carlo for a) the electron method and b) the double angle method

W can be evaluated using y from the following formula:

$$W_{da} = \sqrt{s y_{da}}$$

where s is the total squared centre of mass energy.

To reconstruct t, it is approximated to be the square of the missing transverse momentum in the event, in essence the square of the transverse momentum transfer to the proton. This makes the reasonable approximation that the longitudinal component of the momentum transfer to the proton is negligible. Thus t can be reconstructed using the following formula:

$$t \approx (p_{tp})^2 = (\overline{p_e} + \overline{p_m})_t^2$$

where p_{tp} is the transverse momentum of the proton and $\overline{p_e}$ and $\overline{p_m}$ are the three-momenta of the electron and the meson system respectively. The momentum

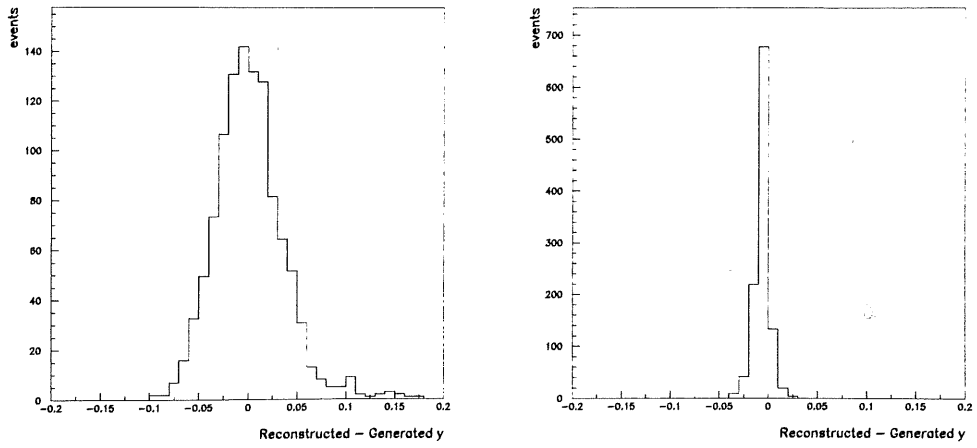

Figure 4.8: Resolution in y obtained from Monte Carlo for a) the electron method and b) the double angle method

of the meson is determined from the reconstructed tracks and the momentum of the electron from Q^2_{da} and y_{da}, giving a more accurate value than the direct measurement from the BEMC.

Figure 4.9 shows the resolution in t from Monte Carlo for both the double angle and electron method.

4.4.9 Kinematic Cuts

Finally, to define the kinematic range in which the measurement is made the following kinematic cuts are applied:

- $Q^2_{da} > 4$ GeV^2
- 35 GeV $< W_{da} <$ 140 GeV.

These cuts ensure that the events are in a kinematic region in which the relevant detectors are well understood and well modelled by Monte Carlo. Figures 4.10 and 4.11 show the smeared acceptance as a function of W_{da} and Q^2_{da} for the two samples, estimated using the DIFFVM Monte Carlo. The drop in acceptance at the edges of the accepted W range is due to the acceptance for reconstruct-

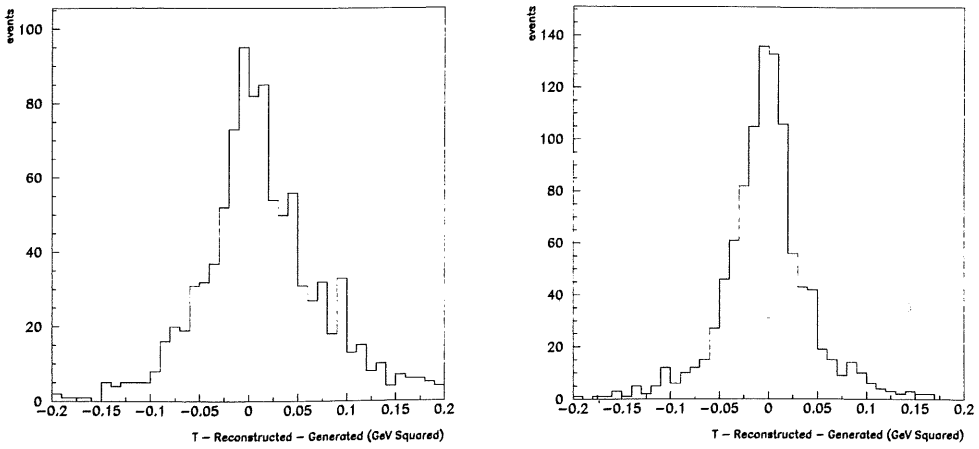

Figure 4.9: Resolution in t obtained from Monte-Carlo for a) the electron method and b) the double angle method

ing the required tracks in the θ_{track} range specified by the cuts. The drop in acceptance at Q^2 below around 10 GeV^2 is mainly due to the lower efficiency for reconstructing an electron in the BEMC at low θ_e. This drop in acceptance is also partly due to the lower track p_t at lower Q^2 due to the produced tracks balancing the electron in p_t.

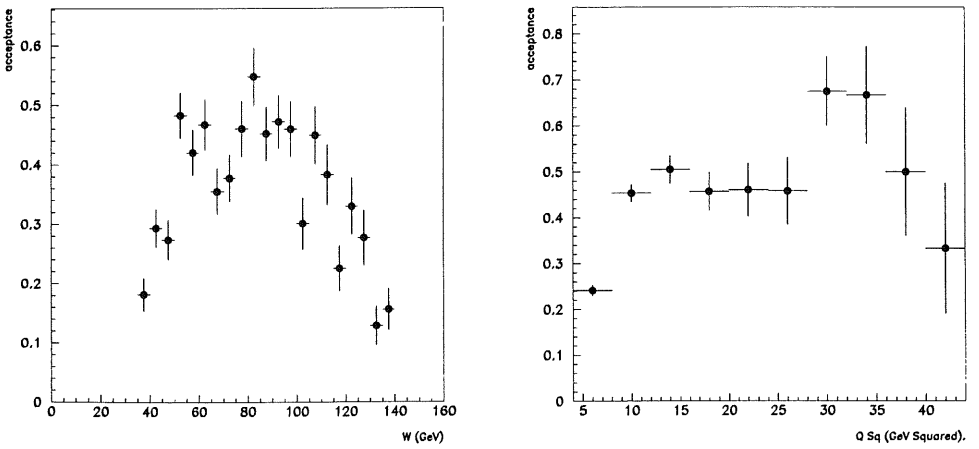

Figure 4.10: Acceptance as a function of a) W and b) Q^2 for the ρ' sample

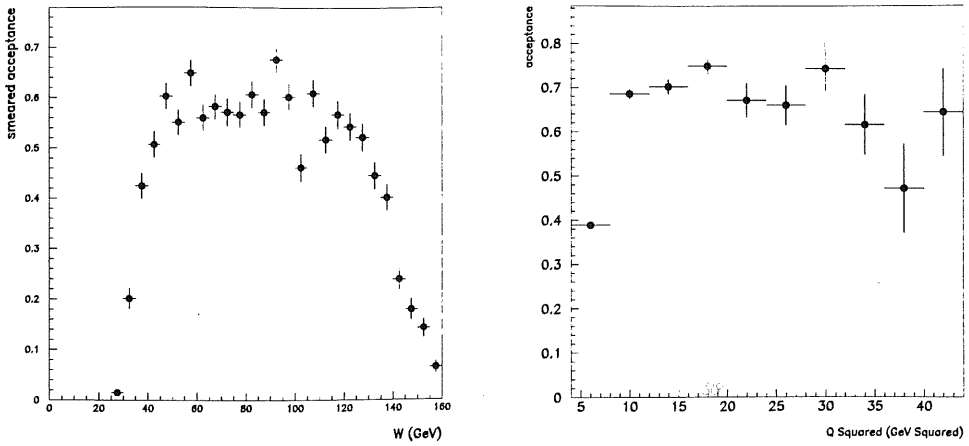

Figure 4.11: Acceptance as a function of a) W and b) Q^2 for the ρ sample

Figures 4.12 and 4.13 show the uncorrected W_{da} and Q^2_{da} distributions of the events selected using all other cuts with, in each case, a comparison with the same distribution from the DIFFVM Monte Carlo. In all cases the Monte Carlo distributions are normalised to the number of events in the data. The input Monte Carlo distributions $\frac{d\sigma}{dW} \sim W^{0.5}$ and $\frac{d\sigma}{dW} \sim (Q^2)^{-2.5}$ provide good agreement with the data.

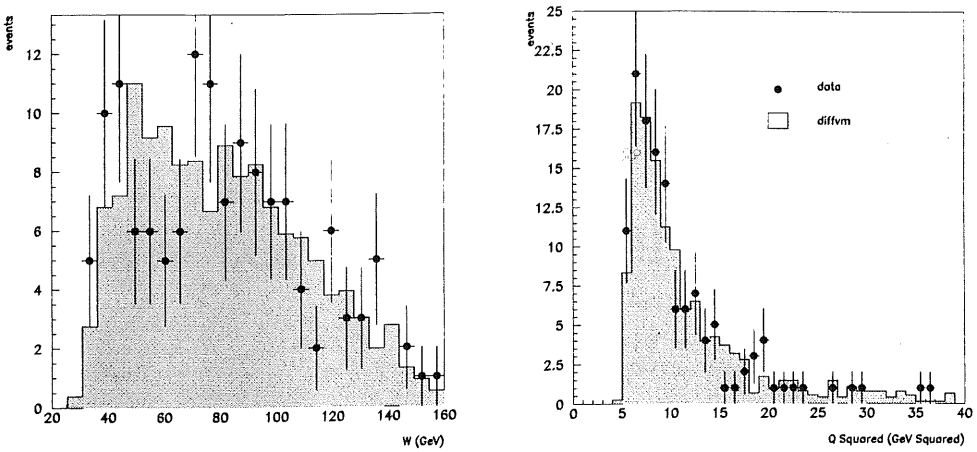

Figure 4.12: a) W and b) Q^2 distributions for selected ρ' events with Monte Carlo comparisons.

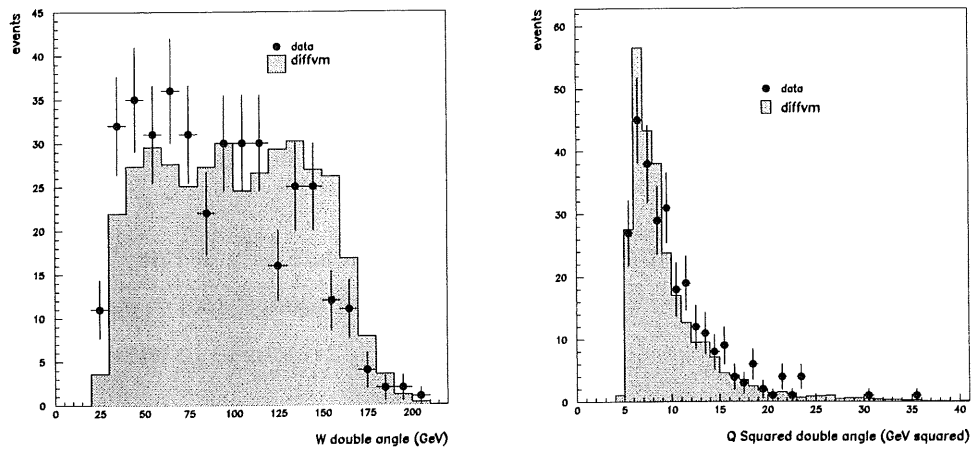

Figure 4.13: a) W and b) Q^2 distributions for selected ρ events with Monte Carlo comparisons.

Chapter 5

Characteristics of Selected Events

5.1 Introduction

This chapter describes the properties of the two samples of events selected using the criteria described in the previous chapter. The aim of this aspect of the analysis is to demonstrate that the samples exhibit the properties typical of diffractive vector meson production and study the observed distributions. This is particularly interesting in the case of the 4 π sample as ρ' production has not previously been studied at the Q^2 and W ranges accessible at HERA.

5.2 4-track Sample

5.2.1 Mass Distribution

Figure 5.1 shows the uncorrected 4 π invariant mass distribution of the events selected as ρ' candidates with a DIFFVM model comparison normalised to the same number of events.

From figure 5.1 an enhancement is clearly seen at a 4 π invariant mass of around 1.5 GeV. Due to presence of additional events at higher mass the spectrum can not be attributed simply to production of a single resonance and some non-resonant background must be present within the sample.

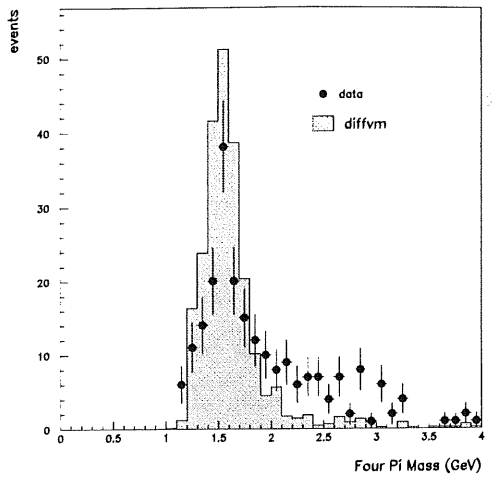

Figure 5.1: Invariant 4 π mass distribution of the the candidate ρ' events with a DIFFVM comparison normalised to the same number of events

5.2.2 Background Subtraction

To examine the resonance signal within the 4 π sample, an estimation of the background present is required. One way in which this can be done is described by Aston et al. [38] in $\gamma p \rightarrow \pi^+ \pi^- \pi^+ \pi^-$. In their analysis, the number of events is much larger than that available here and hence a more accurate estimate of the levels of the various backgrounds is possible. The background estimation is based upon three important assumptions:

- The signal is attributed to a single resonance at around 1500 MeV mass. At the time of the above analysis, the ρ' was thought to exist as a single resonance, the $\rho'(1600)$.

- The background contributions do not interfere with either the signal or each other. There is no justification for this assumption. However, the alternative results in so many parameters for the fitted distributions that no meaningful information can be extracted.

- Two alternative assumptions were made for the decay mode of the ρ':

$$\rho' \to A_1\pi^+ \to \rho\pi^+\pi^- \to \pi^+\pi^-\pi^+\pi^-$$

and

$$\rho' \to \eta\pi^+ \to \rho\pi^+\pi^- \to \pi^+\pi^-\pi^+\pi^-.$$

For each ρ' decay hypothesis, the possible 2 π and 3 π distributions and the angular decay distribution are fitted simultaneously in 100 MeV bins of mass to estimate the relative amounts of the following contributions in each bin:

- ρ' signal following the assumptions on the decay mode.
- $\rho\ \pi^+\ \pi^-\ p_t$ limited phase space.
- $\rho\ \pi^+\ \pi^-$ phase space.
- 4 π p_t limited phase space.
- 4 π phase space.

Thus, plotting the number of signal events extracted in each bin of 4 π mass gives an estimation of the signal.

In the 4 π sample under study here, we do not have enough events for an analysis similar to that above. Therefore, the following two methods are used to estimate the quantity of background in the sample:

- Assume the same contributions are present in the 4 π sample as in the above analysis and that they follow the same invariant 4 π mass distributions as found in the γp analysis. Allow the relative normalisation of each contribution to vary.
- Allow for the background using a free parameter quadratic.

The parameterisations of the mass spectrum shown later in this chapter are based upon the above assumptions for the background mass distributions. The two alternatives are used to provide an estimation of the systematic errors both in the resonance parameters extracted and the cross-section ratio measurement. The lack of a fully satisfactory background estimate provides by far the highest

contribution to systematic errors, as is shown in chapter 6.

5.2.3 Observed Resonance Parameters

To extract information on the observed 4 π sample two hypotheses are chosen:

• The peak observed in the 4 π mass spectrum of observed events can be attributed to the production of a single resonance and a quantity of non-resonant background. This allows comparison of the data characteristics to previous observations of ρ' production, where the picture of a single resonance was assumed.

• The peak observed can be attributed to the production of two resonances, the $\rho'(1450)$ and the $\rho'(1700)$ as listed by the Particle Data Group [48]. The observed shape of the mass spectrum is then attributed to the interference between the two resonances, constructively interfering in the region around the observed data mass peak.

In both the above pictures, the background assumptions outlined in the previous section are taken.

All fits are performed using the MINUIT [58] fitting package using a maximum likelihood method.

Single Resonance Fits

Figure 5.2 shows the 4 π mass distribution fitted using a combination of the following contributions:

• Fixed width Breit-Wigner distribution describing the ρ' signal. This contribution is parameterised as

$$\frac{dN}{dm_{4\pi}} = \frac{m_{4\pi} m_{\rho'} \Gamma_{\rho'}}{(m_{\rho'}^2 - m_{4\pi}^2)^2 + m_{\rho'}^2 \Gamma_{\rho'}^2} \tag{5.1}$$

where $m_{\rho'}$ and $\Gamma_{\rho'}$, the mass and width of the resonance, are allowed to vary as free parameters in the fit. The relative normalisation of this contribution is also allowed to vary.

• Background contributions. The three major contributions found from the photoproduction ρ' data [38] are used to estimate the background. These are the $\rho\pi\pi$ p_t limited phase space, 4 π phase space and 4 π p_t limited phase space distributions. The shapes of these distributions are fixed at those extracted in the photoproduction analysis and the relative contributions are allowed to vary. The χ^2/number of degrees of freedom for this fit is 4.962/11.

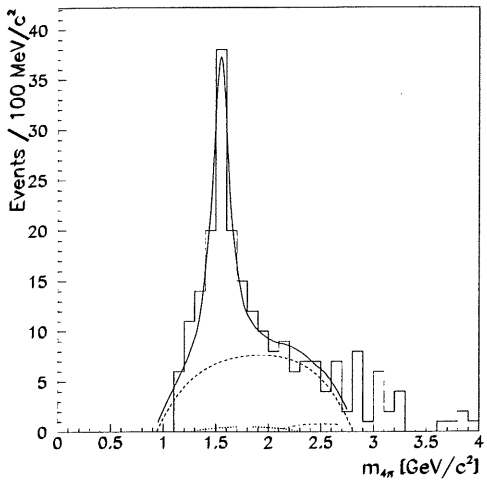

Figure 5.2: 4 π mass spectrum fitted using signal and background contributions. The dashed line shows the contribution from $\rho\pi\pi$ p_t limited phase space, the dotted line that from 4 π phase space and the dot-dashed line that from 4 π p_t limited phase space. The fit is explained in the text.

To estimate the systematic errors on both the resonance parameters and the background contributions, the range of $m_{4\pi}$ mass in which the fit is performed is varied. The fitting range allows for a variation in the relative background samples with the $\rho\pi\pi$ p_t limited phase space and the 4 π phase space distributions accounting for nearly all the background under the peak. This is what was found in the photoproduction analysis [38]. Figure 5.3 shows the 4 π mass distribution fitted using a general free parameter quadratic background and fitting the spectrum up to a 4 π mass of 3 GeV. The χ^2/number of degrees of freedom for the fit shown here is 25.37/15. This is dominated by the contribution from the data points at around 2.8...3 GeV. The background parameterisation used in figure 5.3 is used in estimating the systematic errors on the fitted parameters and the background contribution.

Using the fitting procedures and assumptions described above, the following

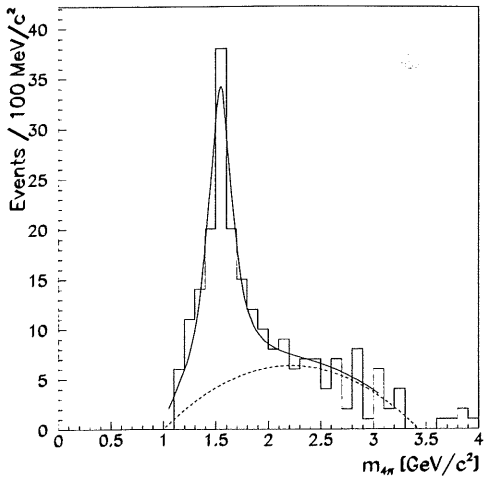

Figure 5.3: 4 π mass spectrum fitted using signal and background contributions. The dashed line shows the fitted background contribution. The fit is explained in in the text.

resonance parameters are extracted when treating the signal as a single resonance

$$m_{\rho'} = 1.54 \pm 0.02_{stat.} \pm 0.01_{syst.} GeV$$

$$\Gamma_{\rho'} = 0.19 \pm 0.05_{stat.} \pm 0.05_{syst.} GeV.$$

The systematic errors come from using the two alternative background parameterisations and, in each case, varying the range of the fit. The resonance mass is quite insensitive to the choice of background and range of the fit. The width, however has a larger systematic error. This is because the fitted width is strongly dependent upon the fitted quantity of background under the peak. A smaller background contribution leads to a larger width of the resonance.

Two Resonance Fits

As described in detail in chapter 3, the ρ' peaks in previous data have been interpreted as the interfering combination of two ρ' resonances, resulting in the extraction of the parameters of the $\rho'(1450)$ and the $\rho'(1700)$ [42]. To attempt to fit the 4 π mass spectrum as a combination of the two resonances, the resonance

contribution to the mass spectrum is fitted as

$$|BW(m_{\rho'(1450)}, \Gamma_{\rho'(1450)}) + \alpha e^{i\beta} BW(m_{\rho'(1700)}, \Gamma_{\rho'(1700)})|^2$$

where

$$BW(m_{\rho'}, \Gamma_{\rho'}) = \frac{m_{4\pi} m_{\rho'} \Gamma_{\rho'}}{(m_{\rho'}^2 - m_{4\pi}^2)^2 + m_{\rho'}^2 \Gamma_{\rho'}^2} \tag{5.2}$$

for each ρ' resonance. α is the relative contribution of the $\rho'(1700)$ and β the relative phase. The relative normalisation of the resonance contribution is allowed to vary and the same background contributions are used as in the single resonance fits.

Figures 5.4 and 5.5 show the 4 π mass spectrum fitted using the 2 assumptions on the background shape. The χ^2/number of degrees of freedom for each fit is 8.923/11 and 29.27/15 respectively. Again, fitting to 3 GeV in the second fit results in a large increase in χ^2.

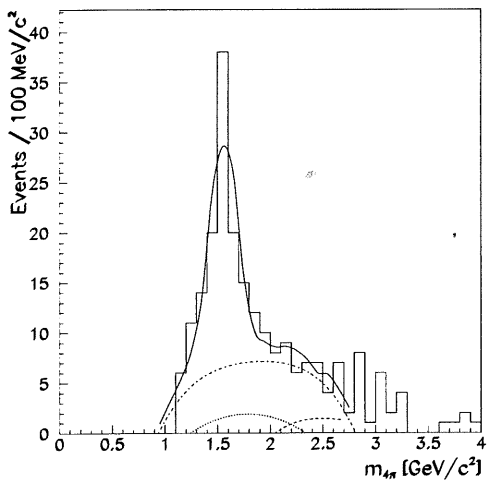

Figure 5.4: 4 π mass spectrum fitted using 2 interfering ρ' resonances and background contributions. The dashed lines show the fitted background contributions. The fit is explained in in the text.

It is found that the mass spectrum can adequately be described using the two interfering ρ' resonances. The following parameters are extracted:

$$\alpha = 0.69 \pm 0.12_{stat.} \pm 0.07_{syst.}$$

$$\beta = 2.8 \pm 0.4_{stat.} \pm 0.4_{syst.}$$

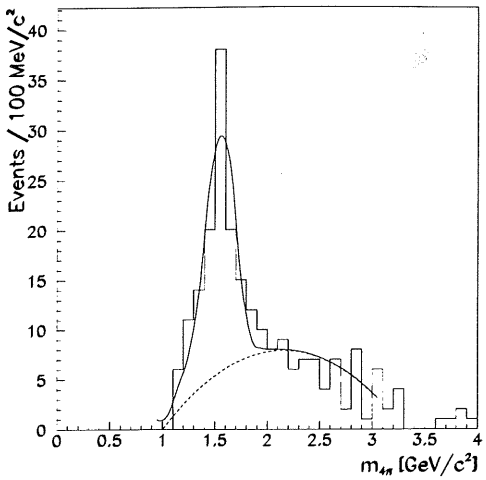

Figure 5.5: 4 π mass spectrum fitted using 2 interfering ρ' resonances and background contributions. The dashed line shows the fitted background contribution. The fit is explained in in the text.

showing that a larger contribution from the $\rho'(1450)$ is preferred. The fits favour a phase difference of around π radians, 180°, showing that, as expected, the two resonances need to be out of phase to produce the destructive interference around the two resonance masses. The relative contributions of the resonances and the observed phase difference are consistent with those seen in fitting previous ρ' data [42]. The background quantities observed in the 2 resonance fits are consistent with those observed in the single resonance fits.

5.2.4 Decay Mode

In previous observations of ρ' resonances, significant decay branching ratios to $\rho\pi^+\pi^-$ have been observed. Therefore, in attributing the enhancement in the mass spectrum of Figure 5.1 to a ρ' resonance, we would expect to see significant ρ production in the decay products. A problem occurs in trying to isolate any ρ meson produced in the 4 π sample. Assuming a ρ meson is produced in a given event and then decays via $\rho \rightarrow \pi^+\pi^-$, it is not known which π^+ and π^- are from the decay of the ρ. Hence there are 4 possible $\pi^+\pi^-$ combinations in each event and, assuming only one ρ produced per event, only one of these corresponds to a produced ρ. Figure 5.6 shows the 2 π invariant masses of the possible $\pi^+\pi^-$

combinations for the selected ρ' events. All 4 possible combinations are plotted for each event. For a comparison of what might be expected purely from phase space, also plotted are the $\pi^+\pi^+$ and $\pi^-\pi^-$ 2 π invariant mass combinations for each event. As there are only 2 of these combinations, each contributes 2 histogram entries to enable a direct comparison.

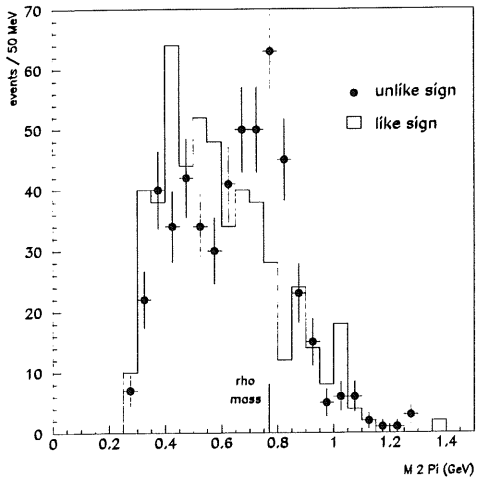

Figure 5.6: 2 π invariant mass distributions of unlike sign 2 π combinations for events in the 4 π sample. As a comparison, like sign combinations are shown normalised to twice the number of entries.

From Figure 5.6 it is clear that there is a significant excess of entries in the unlike sign combinations at invariant mass values around the ρ mass. To quantify this excess precisely is difficult as the ρ is a broad resonance (the width of the ρ is 150 MeV) and hence in many events there are more than one ρ candidates per event. Figure 5.7 shows a scatter plot of the invariant mass of one $\pi^+\pi^-$ combination plotted against the invariant mass of the $\pi^+\pi^-$ combination recoiling against it. Hence there are two contributions for each event.

From Figure 5.7 two clear bands around the ρ mass can be seen on each axis showing again the significant ρ signal in the decay products.

5.2.5 t Distribution

The following selection cuts are required to extract the t distribution of the 4π event sample:

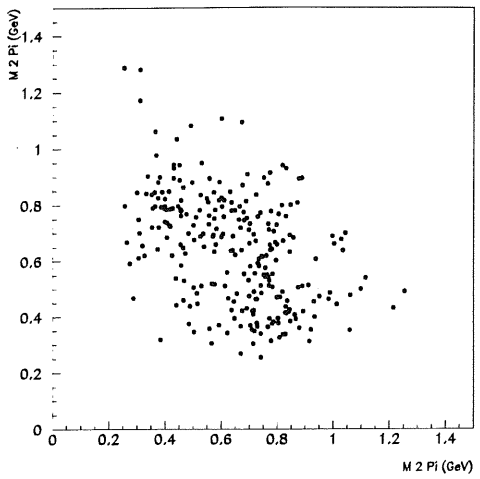

Figure 5.7: Scatter plot of the invariant masses of the possible π^+ π^- combinations for the selected ρ' events.

- The minimum Q^2_{da} cut is raised to 8 GeV^2.

- Events in which the electron is detected in the triangle regions of the BEMC, in which the BEMC trigger efficiency is not well known or modelled, are excluded from the distribution.

These ensure that acceptance corrections are well understood. For the cross-section ratio measurement, the electron triggering efficiencies and acceptance corrections for the two samples cancel and are therefore not required to be so well determined.

As described in chapter 2, diffractive processes are intrinsically peripheral, the momentum transfer from the struck proton is small. To establish the observed 4 π events as elastic ρ' production, we would expect to see a steep exponential $|t|$ distribution, as is seen in high Q^2 elastic ρ and ϕ electroproduction data [31] [32] [35].

Figure 5.8 shows the $|t|$ distribution for the sample of events selected using the selection procedure outlined in chapter 4. The fit is performed in the region $0 < |t| < 0.6$ GeV^2. In this region the Monte Carlo statistics are sufficient to establish that the acceptance is flat in $|t|$ and hence no attempt to correct the t distribution for detector effects is necessary. To do this accurately, a greater

understanding of the background processes would be required. No background subtraction is used on the sample in figure 5.8, the backgrounds are accounted for in fitting the distribution, as described below.

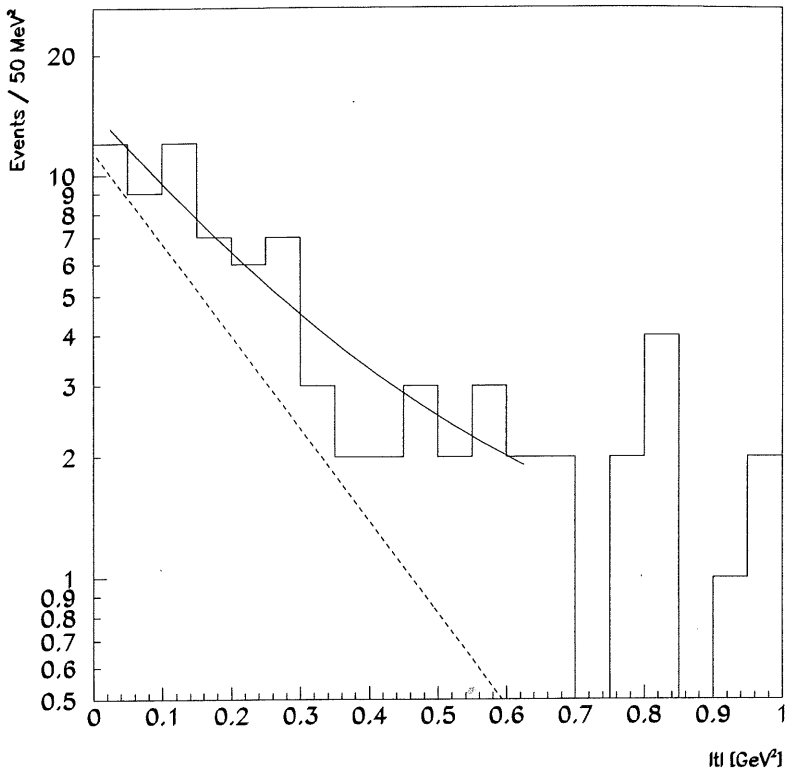

Figure 5.8: Distribution in $|t|$ for selected events in the 4 π sample. The fit is described in the text. The dotted line shows the fitted contribution for the ρ' signal.

The fit shown in figure 5.8 includes three contributions:

- An exponential term accounting for the elastic ρ' contribution. The normalisation and slope are left as free parameters.

- An exponential term accounting for the proton dissociative contribution to the sample. To estimate the relative normalisation, it is assumed that the ratio of proton dissociative to elastic events in the sample is the same as that found in analyses of ρ production in 1994 H1 data [31] [35]. This is a fair assumption assuming factorisation of the process at the proton-pomeron and photon-pomeron vertices. The fixed slope parameter used for this contribution is set at -2.5. This

value was measured in proton dissociative ρ events [35]. The systematic error on the fit parameters takes into account variations in both the normalisation and slope of the proton dissociative contribution.

- An exponential term accounting for the non-resonant background contribution. The slope of this contribution is fixed at -0.15, consistent with the t distribution of non-diffractive event samples. The normalisation of this contribution is fixed at the proportion of events estimated to be non-resonant background from the fits to the 4 π mass spectrum.

The relative normalisation and slope parameters are varied within errors to give an idea of the systematic error on the resonance slope parameter. The slope is found to be

$$b = 5.3 \pm 1.7_{stat.} \pm 0.6_{syst.} GeV^{-2}$$

which, within errors, is consistent with the slope parameters extracted in ρ electroproduction in this study, see later in this chapter, and in previous studies at HERA [31] [32].

5.3 2-track Sample

5.3.1 Mass Spectrum

Figure 5.9 shows the 2 π invariant mass distribution for the sample of 2 track events obtained using the selection described in chapter 4. In addition to the outlined selection, any remaining background due to the production of ϕ and ω mesons is estimated using information from DIFFVM Monte Carlo files simulating the production of all 3 resonances and subtracted on a bin by bin basis. The resonances are assumed to be produced according to the SU(3) ratios $\rho : \phi : \omega = 9 : 1 : 2$ and the total number of combined Monte Carlo events is normalised to the number of data events.

A large enhancement attributed to the $\rho(770)$ resonance is observed. The fit superimposed onto the distribution consists of a combination of a free parameter relativistic Breit-Wigner distribution, allowing for a momentum dependent width, and an additional function allowing for the contribution from non-resonant

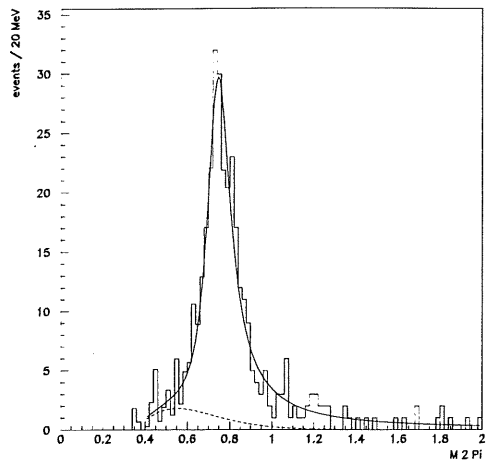

Figure 5.9: Invariant 2 π mass distribution for the candidate ρ events. The solid line shows the result of the fit explained in the text. The dashed line shows the fitted contribution from remaining non-resonant background in the sample.

background. The Breit-Wigner function has the following form:

$$\frac{dN(m_{\pi\pi})}{dm_{\pi\pi}} = \frac{m_{\pi\pi}\ m_\rho\ \Gamma(m_{\pi\pi})}{(m_\rho^2 - m_{\pi\pi}^2)^2 + m_\rho^2\ \Gamma^2(m_{\pi\pi})}, \tag{5.3}$$

where $\Gamma(m_{\pi\pi})$ is the mass dependent width:

$$\Gamma(m_{\pi\pi}) = \Gamma_\rho\ \frac{q*^{\,3}}{q_0*}\ \frac{2}{1 + (q^*/q_0^*)^2}. \tag{5.4}$$

Here, m_ρ and Γ_ρ are the mass and width of the ρ resonance, q^* is the pion momentum in the 2 π rest frame and q_0^* is this momentum when $m_{2\pi} = m_\rho$.

The following distribution is used to account for the remaining non-resonant background:

$$\frac{dN}{dm_{\pi\pi}} = \alpha_1\ (m_{\pi\pi} - 2m_\pi)^{\alpha_2}\ e^{-\alpha_3 m_{\pi\pi}}. \tag{5.5}$$

Here, m_π is the pion mass and α_1, α_2 and α_3 are free parameters in the fit. This distribution includes a threshold term and exponential fall off and has been shown to provide a good description of this background for a sample of ρ events in a similar kinematic range in 1994 H1 data [31]. To provide an estimation of the error on the non-resonant background subtraction, a simple straight-line background contribution is used as an alternative to the above distribution.

The following values are obtained for the mass and width of the resonance using the fit outlined above:-

$$\bullet m_\rho = 0.751 \pm 0.010_{stat.} \pm 0.01_{syst.}$$

$$\bullet \Gamma_\rho = 0.138 \pm 0.016_{stat.} \pm 0.01_{syst.}$$

where the systematic errors are estimated using alternative forms for the non-resonant background.

An interesting feature of the 2 π spectrum is the lack of a significant ρ' signal. No precise measurements of the ρ' branching ratios have been made. The ρ' has been seen to decay into $\pi^+ \pi^-$ in photoproduction and $e^+ e^-$ scattering. The lack of any significant signal in figure 5.9 and the increased acceptance for the two particle decay suggests that the branching ratio to $\pi^+ \pi^-$ is very small in comparison to the 4 π decay mode.

5.3.2 t Distribution

Figure 5.10 shows the fitted distribution in $|t|$ for the ρ sample. The same additional cuts are applied to this sample as to the sample used to measure the ρ' t distribution. The same fitting procedure is applied with three exponential terms, one for the resonance signal, one for the proton dissociation background and one for the non-resonant background.

The slope parameter for the ρ contribution is found to be

$$b = 7.3 \pm 1.0_{stat.} \pm 0.6_{syst.} GeV^{-2}$$

5.3.3 cosθ^* Distribution

Figure 5.11 shows the distribution in cos(θ^*) for the events in the ρ sample. The same additional selection cuts are used for this distribution as are used for the t distribution. This is because the cosθ^* distribution is correlated to Q^2 and hence it is necessary to work in a region in which the acceptance is well understood.

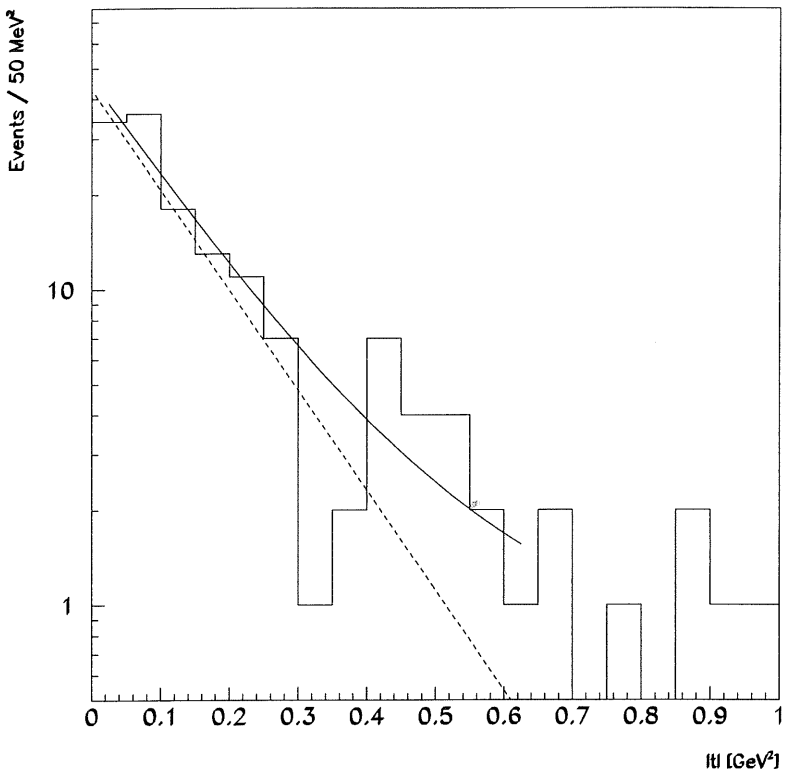

Figure 5.10: Distribution in $|t|$ for selected events in the 2 π sample. The fit shown is described in the text. The dotted line shows the fitted contribution for the ρ signal.

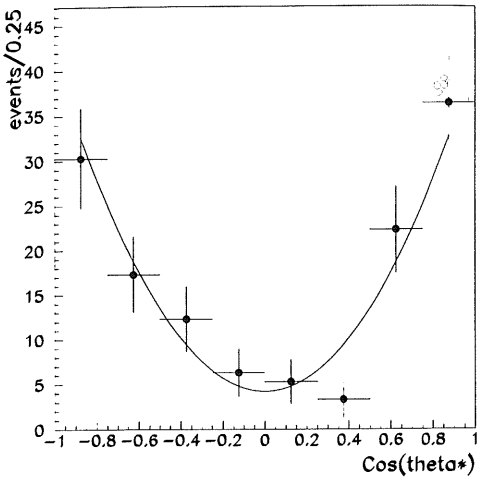

Figure 5.11: Distribution in $\cos(\theta^*$ for the events in the ρ sample. Non-resonant background is subtracted. The fit is described in the text.

Following this cut, the ρ Monte Carlo shows that the acceptance is flat in $\cos\theta^*$ and hence no acceptance correction is applied. The non-resonant background is subtracted on a bin-by-bin basis using the estimation of the amount of this background from the fits to the 2 π mass spectrum. The assumption is made that this contribution is flat in $\cos\theta^*$. The distribution is fitted using the following form, as in equation 2.27:

$$A(3r_{00}^{04} - 1)\cos^2\theta^* + (1 - r_{00}^{04}),$$

where A is the overall normalisation and r_{00}^{04} is the spin density matrix element which specifies the probability that the meson is longitudinally polarised. The χ^2/number of degrees of freedom of the fit is 11.59/6.

The following result is obtained:

$$r_{00}^{04} = 0.83 \pm 0.05_{stat.} \pm 0.03_{syst.}$$

at an average Q^2 of around 13 GeV^2. The systematic error comes from varying the background contribution within the estimated errors. This result is consistent with other results on light vector meson production and is consistent with SCHC with the virtual photons being dominantly longitudinally polarised as Q^2 increases.

5.4 Conclusions

Characteristics of the observed 2 π and 4 π events have been studied. The 4 π mass distribution shows a peak at around 1.5 GeV which can be attributed to a single ρ' resonance with mass $1.54 \pm 0.02_{stat.} \pm 0.01_{syst.}$ GeV and width $0.19 \pm 0.05_{stat.} \pm 0.05_{syst.}$ GeV. Alternatively, the peak can be described by an interfering combination of the two Particle Data Group listed ρ' resonances, the $\rho'(1450)$ and the $\rho'(1700)$, with the larger contribution coming from the $\rho'(1450)$ with a phase difference of around 180°. In each case a significant amount of non-resonant background is required below the peak. There is evidence for significant ρ production in the decay products when looking at the possible opposite sign 2 π mass combinations of the events. Looking at the distribution in $|t|$, the b slope for the ρ' signal is measured to be $b = 5.3 \pm 1.7_{stat.} \pm 0.6_{syst.}$ GeV^{-2}, consistent with b slopes measured in other vector meson electroproduction analyses.

The 2 π sample demonstrates all the characteristics of ρ electroproduction. The mass and width of the observed signal are consistent with the nominal ρ mass and width. The b slope is measured as $b = 7.3 \pm 1.0_{stat.} \pm 0.6_{syst.}$ GeV^{-2}. The distribution in $\cos(\theta^*)$ is found to be consistent with s-channel helicity conservation.

Chapter 6

Measurement of the ρ'/ρ Cross-Section Ratio

6.1 Introduction

The ratio of the cross-sections for ρ' and ρ production at high Q^2 is presented in this chapter. A ratio measurement is made for two reasons:

- As described in chapter 4, a looser selection procedure may be used hence greatly increasing the available statistics.

- In comparison to previous results made at much lower Q^2 values, the relative evolution of the two cross-sections is of theoretical interest.

The cross-section ratio measured and presented here is defined as follows:

$$R_{\rho'/\rho} = \frac{\sigma(ep \to e\rho'(\pi^+\pi^-\pi^+\pi^-)p)}{\sigma(ep \to ep\rho; m_{2\pi} < 1.5)} \tag{6.1}$$

This measurement is defined purely in the $\rho' \to \pi^+\pi^-\pi^+\pi^-$ decay mode. No factor is included for the branching ratio to this mode as this is not known. The measurement is also limited to the region $m_{2\pi} < 1.5$ GeV. This is because corrections applied for the tail of the ρ resonance become very uncertain at high masses and model dependent assumptions are then required.

To provide a valid comparison with low Q^2 and photoproduction ρ and ρ'

data, the assumption is made that the ρ' is treated as the production of a single resonance. The implications of using this assumption in the measurement are described in the subsequent sections.

In the following, the methods used to determine all the contributions entering the final measurement are presented. Following this, the methods of estimating the systematic errors on the final measurement, along with the final estimations for each contribution, are given. Finally, the measurement is presented.

6.2 Determination of the Cross-Section Ratio

The ratio of cross-sections is determined using the following equation:

$$\frac{\sigma_{ep\to e\rho'(\pi^+\pi^-\pi^+\pi^-)p}}{\sigma_{ep\to e\rho p}} = \frac{(N^{\rho'} - N^{\rho'}_{BACK})}{(N^{\rho} - N^{\rho}_{BACK})} \cdot \frac{A^{\rho}}{A^{\rho'}} \cdot \frac{T^{\rho'}}{T^{\rho}}$$

where :

- $N^{\rho'}$ - The number of events in the ρ' sample in the 4 π mass range $1.2 < M_{4\pi} < 1.9$ GeV. This limits the measurement to a region of 4 π invariant mass where there are sufficient Monte Carlo statistics to enable acceptance corrections to be applied.

- $N^{\rho'}_{BACK}$ - The estimated number of non-resonant background events in the ρ' sample in the 4 π mass range $1.2 < M_{4\pi} < 1.9$ GeV.

- N^{ρ} - The number of events in the ρ sample in the 2 π mass range $0.6 < M_{2\pi} < 1$ GeV. Again, this mass region allows sufficient Monte Carlo statistics to allow acceptance corrections to be made.

- N^{ρ}_{BACK} - The estimated number of non-resonant background events in the ρ sample in the 2 π mass range $0.6 < M_{2\pi} < 1$ GeV.

- $A^{\rho'}$ - Acceptance correction applied for the ρ' sample. This is estimated using the ρ' Monte Carlo and compensates for all detector inefficiencies and the effects of limited acceptance.

- A^{ρ} - Acceptance correction applied for the ρ sample.

• $T^{\rho'}$ - Correction applied to correct for the tail of the ρ' outside the mass range used, assuming a single resonance hypothesis.

• T^{ρ} - Correction applied to correct for the tail of the ρ outside the mass range used assuming the nominal mass and width of the ρ resonance. As explained earlier, this correction is only made up to a 2 π mass of 1.5 GeV because of model uncertainties at higher masses.

There are no terms included in the above equation for the following:

• Luminosity. Both the ρ' and ρ samples are determined from the same 1994 data sample. Hence the total luminosity of the run ranges from which the data is taken is the same for both samples and cancels in the cross-section ratio.

• Background due to proton dissociation. As the process under study, for the purposes of comparison with theory and previous data, is quasi-elastic ρ' and ρ production, some correction is required within each sample to account for the proton dissociation background. When computing the ratio of the two cross-sections, it is assumed that the proportion of events in the two samples due to this background will cancel, i.e. factorisation is assumed.

The subsequent sections detail how each of the above contributions are determined.

6.3 Number of Events

After the selection procedure outlined in chapter 4, the following number of events are obtained in the relevant mass ranges:

• $N^{\rho'}_{1.2GeV<m_{4\pi}<1.9GeV} = 130$

• $N^{\rho}_{0.6GeV<m_{2\pi}<1.9GeV} = 274$

6.4 Estimation of Remaining Backgrounds

The remaining non-resonant background present in the two event samples is estimated from the fits to the 4 π and 2 π mass spectra. The following results are obtained:

$$N^{\rho'}_{BACK} = 46 \pm 14$$

and

$$N^{\rho}_{BACK} = 30 \pm 10,$$

where, in each case, the errors are estimated by using alternative descriptions for the backgrounds.

6.5 Estimation of Acceptance Corrections

For both the ρ' and ρ samples, the acceptance corrections, $1/A^{\rho'}$ and $1/A^{\rho}$, are applied to correct for those events which are produced in the kinematic range studied but not reconstructed due to geometric and detector effects. The acceptance is estimated by using DIFFVM files generated within the kinematic bounds outlined in chapter 4. These events are then passed through the H1 detector simulation, H1SIM, to produce the expected detector response for the kinematic properties of those events. The acceptance is defined as follows:

$$A = \frac{N_{rec}}{N_{gen}}$$

where N_{rec} is the number of events reconstructed within the studied kinematic range after the same selection procedure, that outlined in chapter 4, is applied as that applied to the data. N_{gen} is the number of events generated within the studied kinematic range.

The *smeared* acceptance is used so that events which are generated outside the kinematic range studied but are reconstructed within are included in N_{rec} and likewise, due to the selection procedure, events generated within the studied range which are reconstructed outside are not included.

The smeared acceptance takes into account the following effects:

- The fraction of produced mesons with all decay products within the required p_t and θ ranges.

- The fraction of events in which the scattered electron satisfies the requirements on its direction and energy.

- The fraction of events in which the requirements on the signals in the forward detectors are satisfied.

The simulation of the detectors does not include noise effects. Due to the requirement on the data that there should be little or no activity in the forward detectors or liquid argon calorimeter, events in which there is noise in these detectors will be rejected. Chapter 4 outlines the procedure used to isolate noise clusters in the liquid argon calorimeters. To estimate the losses remaining due to noise, detector noise is added to the Monte Carlo events. This noise is estimated using random trigger events. These events have no real activity in the detector and hence the fraction which fail the requirements on liquid argon and forward detector activity give a good estimate of the effects of noise.

When computing the acceptance corrections for the two sample, as they are divided in the overall ratio measurement, the following contributions will cancel:

- Triggering efficiency for the BEMC trigger.

- Overall efficiency for reconstructing an electron in the BEMC within the required energy and angle.

- Efficiency of the forward detectors for rejecting events in which the proton dissociates.

- Acceptance correction for events which are rejected due to detector noise.

The above contributions are estimated separately using the Monte Carlo but no systematic error contribution to the final total acceptance correction is included. Because of the nature of the final states in the two samples, one contribution which will not cancel is the efficiency for reconstructing 4 and 2 tracks, respectively, in the CJC. The following section outlines how these track reconstruction efficiencies are estimated.

6.5.1 Track Reconstruction Efficiency

The efficiency for reconstructing low p_t tracks in the CJC has been studied using K^0_s decays into π^+ π^- [59]. These decays occur isotropically in the K^0_s rest frame, with at least one relatively fast ($p_t > 400$ MeV) pion. These events are used to produce a graph of efficiency against p_t. The efficiency is found to rise from zero to its maximum value between 90 and 140 MeV and remain constant thereafter. The Monte-Carlo detector simulation does not accurately reproduce this behaviour. The reconstruction efficiency in the simulation is above 90% down to a track p_t of around 80 MeV. To increase the limited statistics of, in particular, the ρ' sample, a data p_t cut of 100 MeV is used. Hence the Monte Carlo cannot be accurately used to estimate the track reconstruction efficiency contribution to the acceptance corrections.

Based upon the results of [59], the reconstruction efficiency of tracks in the range $100 < p_t < 140$ MeV is taken to be 0.85 ± 0.02 and that for tracks with p_t above 140 MeV is taken to be 0.98 ± 0.02. To provide a more accurate estimation of the track reconstruction efficiency than could be gained from Monte Carlo, the following formula is used to compute the overall track reconstruction efficiency for the ρ' events:

$$T^{\rho'}_{eff} = f_0 \eta^4_{high} + f_1 \eta_{low} \eta^3_{high}, \tag{6.2}$$

where $T^{\rho'}_{eff}$ is the average track reconstruction efficiency for reconstructing the 4 tracks, η_{low} is the average efficiency for reconstructing tracks in the range $100 < p_t < 140$ MeV and η_{high} is the average efficiency for reconstructing a track with p_t above 140 MeV. η_{low} and η_{high} are taken from [59] and are those values outlined above. f_0 is the proportion of events with all 4 tracks satisfying the condition $p_t > 140$ MeV and f_1 is the proportion of total events with 1 track below this limit. No events are found in either the data or the Monte Carlo to have more than 1 track with a p_t value less than 140 MeV. The average track efficiency for the ρ sample is estimated using:

$$T^{\rho}_{eff} = f_0 \eta^2_{high} + f_1 \eta_{low} \eta_{high}, \tag{6.3}$$

where the same terms apply.

The value of f_1 for the ρ' sample is estimated to be 0.10 ± 0.02 from Monte

Carlo. The error comes from the necessary slight reweighting of the track p_t distribution in the Monte Carlo. The data is in good agreement with this value. The total correction factor, corresponding to the average track reconstruction efficiency for the ρ' sample, is estimated to be 0.91 ± 0.08.

For the ρ sample, the value of f_1 is estimated from Monte Carlo to be 0.05 ± 0.02. Again, this is in agreement with the data. The average track reconstruction efficiency for the ρ sample is estimated to be 0.95 ± 0.04.

Combining the estimated track reconstruction efficiency with the other detector effects, estimated using the Monte Carlo files, the total acceptance for the ρ' is estimated to be:

$$A^{\rho'} = 0.36 \pm 0.04$$

and that for the ρ:

$$A^{\rho} = 0.55 \pm 0.04.$$

The errors include the track efficiency errors estimated above, the error resulting from the Monte Carlo statistics used and the effects of reweighting the Monte Carlo kinematic distributions. No error is included for those detector effects which will cancel in the ratio.

6.6 Tail Corrections

The tail corrections for the two resonances are calculated from the resonance parameters measured from the fits to the 4 π and 2 π mass spectra. The tail correction for the ρ' is calculated using the assumption of a single resonance and the tail correction for the ρ is made up to a mass of 1.5 GeV. The following results are obtained:

$$T^{\rho'} = 1.15 \pm 0.05$$

and

$$T^{\rho} = 1.18 \pm 0.02,$$

where the errors come from varying the masses and widths according to the errors obtained from the fits to the mass spectra.

6.7 Systematic Errors

The individual contributions to the systematic error on the cross-section ratio are as follows:

- Uncertainty on the ρ' background subtraction - 17%.
- Uncertainty on the ρ background subtraction - 4%.
- Uncertainty on the ρ' acceptance correction - 11%.
- Uncertainty on the ρ acceptance correction - 2%.
- Uncertainty on the ρ' tail correction - 4%.
- Uncertainty on the ρ tail correction - 2%.

The total systematic error is estimated to be 21%.

6.8 Result

The following result is obtained:

$$R_{\rho'/\rho} = 0.51 \pm 0.08_{stat.} \pm 0.11_{syst.}$$

at an average Q^2 of 11 GeV^2 and an average W of 80 GeV.

Chapter 7

Comparison with QCD Models

A small number of ρ' measurements have been made in photoproduction and low Q^2 leptoproduction experiments at low energy.

Figure 7.1 shows the Q^2 evolution of the cross-section ratio $R_{\rho'/\rho}$ combining the result of this thesis with previous measurements made at lower energy. Two photoproduction experiments have reported $R_{\rho'/\rho}$ results using fixed target data. The first (Atiya et al. [40]) studied ρ' production on a C target exposed to 50 GeV photons at Fermilab. This ratio is computed using a ρ cross-section from a compilation of results. Only a statistical error is reported for the ρ' measurement and only statistical errors are plotted on figure 7.1. The second fixed target photoproduction experiment (Aston et al. [38]) uses the OMEGA spectrometer at CERN, exposed to photons of energy 20 - 70 GeV. The cross-section ratio is not measured directly but can be computed as $0.07 \pm 0.03 \pm 0.03$ using the ρ cross-section measurement made by the same experiment in the same kinematic range [60].

In leptoproduction, only two experiments quote results on ρ' production. At low energy (11.5 GeV electron beam at Cornell), Killian et al. [61] quote estimates for ρ' and ρ production without errors. From these results, the ratio can be estimated to be about 0.13 at an average Q^2 of around 1 GeV^2. The CHIO Collaboration (Shambroom et al. [62]) have published uncorrected $R_{\rho'/\rho}$ measurements at muon beam energies of 100 and 150 GeV, corresponding to W values of 11 and 14 GeV, and an average Q^2 of around 0.4 GeV^2. These are 0.06 and 0.13 respectively with statistical errors of the order of 20%.

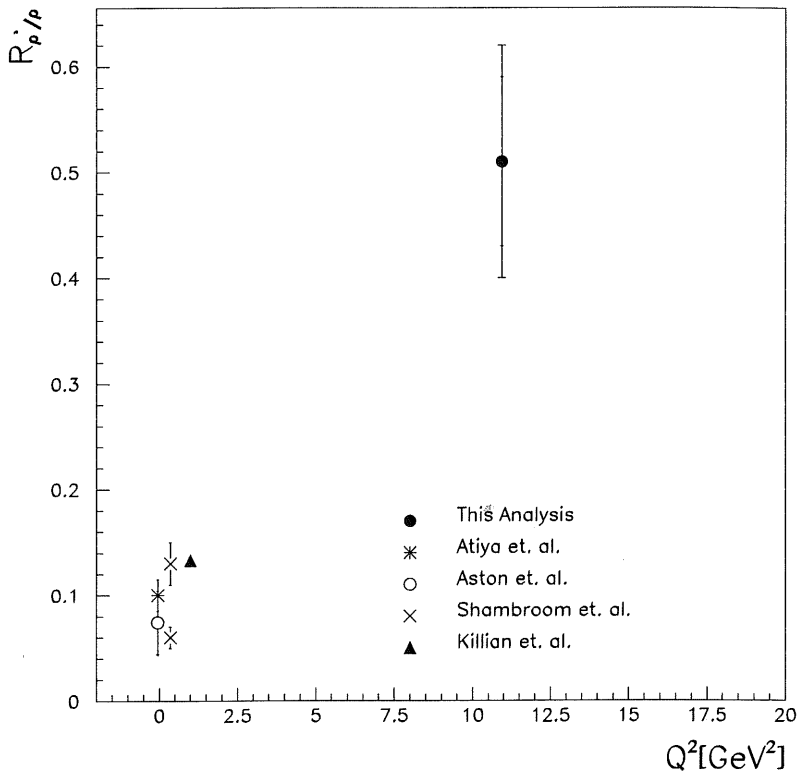

Figure 7.1: The ratio $R_{\rho'/\rho}$ as a function of Q^2 combining the measurement made in this thesis with previous low energy results.

Despite the large errors on the measurement presented in this thesis, a clear rise of the cross-section ratio with Q^2 is observed. This is predicted in the models by Martin et al. [63], Nemchik et al. [47] and Frankfurt et al. [49]:

• Martin et al. Within this model the combination of both the 2S and 1D states including both the longitudinally and transversely polarised mesons is predicted to be produced at a comparable rate to the ρ at a Q^2 of around 8 GeV^2 with the ρ cross-section falling more steeply with Q^2. Production of the $g(1690)$ resonance is predicted to be non-negligible. Within the available statistics, the observed 4 π mass spectrum is adequately fitted without requiring this additional contribution. One differing prediction of this model in comparison to the others is the much flatter distribution of the ratio of longitudinally to transversely polarised meson cross-sections for the excited states. The low statistics do not allow the extraction of any angular decay distributions for the observed ρ' events. This would allow the extraction of this ratio.

• Nemchik et al. Within this model predictions are made for the cross-section ratio for the 2S ρ' meson to the ρ for a combination of the longitudinally and transversely polarised contributions. At a Q^2 of around 10 GeV^2 and a W of 100 GeV, this ratio is predicted to be around 0.3. In the picture of the two interfering ρ' resonances, if we assume that the $\rho'(1450)$ is the 2S excitation and provides a larger contribution to the ρ' signal observed, the prediction of this model is consistent with the measured value of the ratio.

• Frankfurt et al. Within this model, predictions are made separately for the $\rho'(1450)$ and $\rho'(1700)$ for longitudinally polarised mesons. The model predicts that the final state will be dominated by longitudinally polarised mesons. In the limit where the squared masses of the mesons are much smaller than Q^2, the ratios for the $\rho'(1450)$ and $\rho'(1700)$ are 0.45 - 0.95 and 0.22 $\pm$ 0.05 respectively. Because of the uncertainties in the model, these numbers are quoted as good to around a factor of 2. The measurement made is therefore consistent with the predictions of this model.

Table 7.1 gives a summary of the predictions of the 3 models.

The measured cross-section ratio $R_{\rho'/\rho}$ is consistent within errors with the predictions from the three alternative QCD models. Because of the low statistics of the analysis, coupled with the large systematic error due to uncertainties in the

	Quantity Predicted	Q^2 (GeV^2)	Value
Martin et al.	$(\rho'(1450) + \rho'(1700) + \mathrm{g}(1690)) : \rho$ for σ_L and σ_T	8	1
Nemchik et al.	$\rho'(2S) : \rho$ for σ_L and σ_T	10	~ 0.3
Frankfurt et al.	$\rho'(1450) : \rho$ for σ_L	Q^2 much greater than m_V^2	0.45 - 0.95
Frankfurt et al.	$\rho'(1700) : \rho$ for σ_L	Q^2 much greater than m_V^2	0.22 ± 0.05

Table 7.1: Summary of the predictions of the 3 QCD based models for the ratio of cross-sections ρ'/ρ

non-resonant background, no firm conclusions on the structure of the observed resonance peak are possible. The only conclusion to be drawn is that the observed mass spectrum is consistent with the picture of the two ρ' resonances. No detailed extraction of the relative contributions of the two resonances is possible. The lack of statistics also means that it is impossible to extract an angular decay distribution. This would give the relative contributions of longitudinally and transversely polarised mesons and resolve the discrepancy between the model of Martin et al. and the other QCD based models. It would be very interesting to measure the cross-section ratio in the intermediate Q^2 region between the available photoproduction measurements and the measurement presented here. This would differentiate between the model of Nemchik et al., where the node in the 2S wavefunction leads to a very striking Q^2 dependence around 1 GeV^2, and the other models where no such effect is predicted. Future ρ' measurements at HERA should allow such measurements to be made.

All three of the QCD based models discussed in chapter 2 and above use a pomeron composed of two gluons. The measurements described in chapter 2 made in the framework of Regge theory suggest that the momentum of the pomeron is largely carried by gluons. Given the agreement between the QCD models' predictions and the data, it is hoped that future measurements will clarify the links between the two approaches.

7.1 Future measurements at HERA

The future running of the HERA collider should allow significant improvements in the precision of all *ep* physics results. At the start of the 1995 running period, the BEMC calorimeter in the H1 detector was replaced by the SPACAL (Spaghetti Calorimeter) which consists of separate electromagnetic and hadronic sections to allow a much better hadronic resolution than was possible with the BEMC. One advantage of the SPACAL is that it allows access to lower values of Q^2 than the BEMC, down to around 1 GeV^2. At the start of 1998 running an additional calorimeter was added to the H1 detector. This VLQ (Very Low Q^2 calorimeter) sits in the region behind the SPACAL and covers an angular range right down to the beam pipe. Initial background problems have occurred with the triggering of the VLQ but it is hoped that, once these problems have been resolved, the VLQ will tag electrons at very low angles and cover the Q^2 region between a fraction of a GeV right up to the bottom Q^2 range of the SPACAL. The VLQ will allow physics measurements to be made in the Q^2 region between photoproduction, where only comparisons with soft phenomenological models can be made, and the region where hard QCD behaviour sets in. In terms of vector meson analyses, this region is very interesting as, for example, ρ production measurements have shown behaviour expected from Regge theory in photoproduction and characteristics expected from QCD based models at higher Q^2. For ρ' production, this intermediate region will allow differentiation between the three QCD based models described above. The stark differences in the expected Q^2 evolution of the ratio $R_{\rho'/\rho}$ occur in this low Q^2 region. This coverage, coupled with the improvements in the reliability of the HERA machine, will result in a much better level of statistics over a bigger range of Q^2 and W resulting in a better picture of ρ' electroproduction.

Chapter 8

Summary

This thesis presents the first study of ρ' production at high Q^2. The properties of the observed events are consistent with those seen at previous experiments. Within the available statistics, the signal can be adequately treated as a single resonance with mass $m_{\rho'} = 1.54 \pm 0.02_{stat.} \pm 0.01_{syst.}$ GeV and width $\Gamma_{\rho'} = 0.19 \pm 0.05_{stat.} \pm 0.05_{syst.}$ GeV. Alternatively, the signal is also consistent with the interfering combination of two ρ' resonances, $\rho'(1450)$ and $\rho'(1700)$, listed by the Particle Data Group within this mass region. In this case the fitting favours a larger contribution of the $\rho'(1450)$ with the two resonances out of phase. A large decay mode $\rho' \to \rho\pi^+\pi^-$ is favoured by the data. The b slope of the distribution in t is measured to be $5.3 \pm 1.7_{stat.} \pm 0.6_{syst.}$ GeV^{-2}, consistent with other vector meson electroproduction results.

To make a comparison with ρ production over the same kinematic range, a ρ signal is studied. This shows typical ρ behaviour with the mass and width measured to be $m_\rho = 0.751 \pm 0.01_{stat.} \pm 0.01_{syst.}$ GeV and $\Gamma_\rho = 0.138 \pm 0.016_{stat.} \pm 0.010_{syst.}$ GeV, respectively. The b slope of the t distribution is measured to be $b = 7.3 \pm 1.0_{stat.} \pm 0.6_{syst.}$ GeV^{-2}. The cosθ^* distribution matches that expected from s-channel helicity conservation (SCHC) with r^{04}_{00}, the spin density matrix element specifying the probability that the meson is longitudinally polarised, measured to be $0.83 \pm 0.05_{stat.} \pm 0.03_{syst.}$.

The ratio of cross-sections $R_{\rho'/\rho}$ is measured to be $0.51 \pm 0.08_{stat.} \pm 0.11_{syst.}$ at an average Q^2 of 11 GeV^2 and average W of 80 GeV. This is higher than that in photoproduction and very low Q^2 measurements. This rise is predicted

in a number of QCD based models. Future measurements at HERA with more statistics over a larger range of Q^2 will allow more stringent tests of these models.

References

[1] D. H. Perkins. Introduction to high energy physics (3rd. ed.). *Addison Wesley Publishing*, 1987.

[2] R. P. Feynman. *Phys. Rev. Lett.*, 23:1415, 1969.

[3] M. Gell-Mann. A Schematic Model of Baryons and Mesons. *Phys. Lett.*, 8:214–215, 1964.

[4] Jr. C. G. Callan and David J. Gross. High-Energy Electroproduction and the Constitution of the Electric Current. *Phys. Rev. Lett.*, 22:156–159, 1969.

[5] J. D. Bjorken. Asymptotic Sum Rules at Infinite Momentum. *Phys. Rev.*, 179:1547–1553, 1969.

[6] Guthrie Miller et al. Inelastic Electron - Proton Scattering at Large Momentum Transfers. *Phys. Rev.*, D5:528, 1972.

[7] M. Derrick et. al. A Detailed Study of the Proton Structure Function in Deep Inelastic Muon-Proton Scattering. *Nucl. Phys. B*, 259:189–265, 1985.

[8] G. Altarelli and G. Parisi. Asymptotic Freedom in Parton Language. *Nucl. Phys.*, B126:298, 1977.

[9] V. N. Gribov and L. N. Lipatov. Deep Inelastic e p Scattering in Perturbation Theory. *Sov. J. Nucl. Phys.*, 15:438, 1972.

[10] S. Aid et al. A Measurement and QCD Analysis of the Proton Structure Function F_2 (x, Q^2) at HERA. *Nucl. Phys.*, B470:3–40, 1996.

[11] C. F. von Weizsacker. Radiation Emitted in Collisions of Very Fast Electrons. *Z. Phys.*, 88:612–625, 1934.

[12] E. J. Williams. Nature of the High-Energy Particles of Penetrating Radiation and Status of Ionization and Radiation Formulae. *Phys. Rev.*, 45:729–730, 1934.

[13] C. Adloff et al. Low Q^2 Jet Production at HERA and Virtual Photon Structure. *Phys. Lett.*, B415:418, 1997.

[14] P. D. B. Collins. An Introduction to Regge Theory and High Energy Physics. *Cambridge University Press*, 1977.

[15] C. Adloff et. al. Diffraction Dissociation In Photoproduction at HERA. *Z.Phys.*, C74:221–236, 1997.

[16] M.Derrick et. al. Observation of Events with a Large Rapidity Gap in Deep Inelastic Scattering at HERA. *Phys. Lett. B*, 315:481–493, 1993.

[17] T. Ahmed et. al. Deep Inelastic Scattering Events With a Large Rapidity Gap at HERA. *Nucl. Phys. B*, 429:477–502, 1994.

[18] A. Donnachie and P.V.Landshoff. Total Cross Sections. *Phys. Lett. B*, 296:227–232, 1992.

[19] T. Ahmed et al. First Measurement of the Deep Inelastic Structure of Proton Diffraction. *Phys. Lett.*, B348:681–696, 1995.

[20] C. Adloff et al. Inclusive Measurement of Diffractive Deep Inelastic ep Scattering. *Z. Phys.*, C76:613, 1997.

[21] C. Adloff et. al. Thrust Jet Analysis of Deep Inelastic Large Rapidity Gap Events. *Eur. Phys. J.*, C1:495–507, 1998.

[22] C. Adloff et. al. Hadron Production in Diffractive Deep Inelastic Scattering. *Phys. Lett. B*, 428:206–220, 1998.

[23] B. Waugh. Charm Production in Diffractive Deep Inelastic Scattering at HERA. *PhD Thesis*, University of Manchester, 1997.

[24] J. J. Sakurai. Vector Dominance and High-Energy Electron Proton Inelastic Scattering. *Phys. Rev. Lett.*, 22:981 – 984, 1969.

[25] A. D. Martin M. G. Ryskin, R. G. Roberts and E. M. Levin. Diffractive j / psi Photoproduction as a Probe of the Gluon Density. *Z. Phys.*, C76:231, 1997.

[26] S.Brodsky et. al. Diffractive Leptoproduction of Vector Mesons in QCD. *Phys. Rev. D*, 50:3134–3144, 1994.

[27] K. Schilling, P. Seyboth, and Gunter E. Wolf. On the Analysis of Vector Meson Production by Polarized Photons. *Nucl. Phys.*, B15:397–412, 1970.

[28] S. Aid et al. Elastic Photoproduction of Rho0 Mesons at HERA. *Nucl. Phys.*, B463:3–32, 1996.

[29] M. Derrick et al. Study of Elastic Rho0 Photoproduction at HERA Using the ZEUS Leading Proton Spectrometer. *Z. Phys.*, C73:253, 1997.

[30] M. Derrick et al. Measurement of Elastic Omega Photoproduction at HERA. *Z. Phys.*, C73:73, 1996.

[31] S. Aid et al. Elastic Electroproduction of ρ^0 and j / ψ Mesons at Large Q^2 at HERA. *Nucl. Phys.*, B468:3–36, 1996.

[32] M. Derrick et al. Exclusive Rho0 Production in Deep Inelastic Electron - Proton Scattering at HERA. *Phys. Lett.*, B356:601–616, 1995.

[33] P. Amaudruz et. al. Transverse Momentum Distributions for Exclusive ρ^0 Muoproduction. *Z. Phys C*, 54:239–246, 1992.

[34] J.J.Aubert et. al. Exclusive ρ^0 Production in Deep Inelastic Muon Proton Scattering. *Phys. Lett. B*, 161:203, 1985.

[35] C. Adloff et. al. Proton dissociative rho and elastic phi electroproduction at hera. *Z. Phys.*, C75:607, 1997.

[36] M. Derrick et. al. Measurement of the Reaction $\gamma^* p \rightarrow \phi p$ in Deep Inelastic Scattering at HERA. *Phys. Lett. B*, 380:220–234, 1996.

[37] A. Cordier et al. Study of the e+ e- → pi+ pi- pi+ pi- Reaction in the 1.4-GeV to 2.18-GeV Energy Range. *Phys. Lett.*, 109B:129, 1982.

[38] D. Aston et al. The Reaction gamma p → p pi+ pi- pi+ pi- for Photon Energies from 25-GeV to 70-GeV. *Nucl. Phys.*, B189:15, 1981.

[39] M. Atkinson et al. A Spin Parity Analysis of the omega pi0 Enhancement Photoproduced in the Energy Range 20-GeV to 70-GeV. *Nucl. Phys.*, B243:1, 1984.

[40] M. S. Atiya et al. High-Energy Photoproduction of rho-prime (1600). *Phys. Rev. Lett.*, 43:1691, 1979.

[41] A. Quenzer et al. Pion Form-Factor From 480-MeV to 1100-MeV. (Talk). *Phys. Lett.*, 76B:512, 1978.

[42] A. Donnachie and H. Mirzaie. Evidence for Two rho-prime (1600) Resonances. *Z. Phys.*, C33:407, 1987.

[43] M. Atkinson et al. Study of eta pi+ pi- States in the rho-prime (1600) Mass Region Photoproduced in the Reaction gamma p $\rightarrow$ eta pi+ pi- p at Photon Energies of 20-GeV to 70-GeV. *Z. Phys.*, C30:531, 1986.

[44] G. Penso and Tran N. Truong. Current Algebra Calculation of e+ e- $\rightarrow$ 4 pi+- and Determination of rho-prime (1600) Parameters. *Phys. Lett.*, 95B:143, 1980.

[45] S. Godfrey and N. Isgur. Mesons in a Relativized Quark Model with Chromodynamics. *Phys. Rev.*, D32:189, 1985.

[46] M. G. Ryskin A. D. Martin and T. Teubner. The QCD Description of Diffractive Rho Meson Electroproduction. *Phys. Rev.*, D55:4329–4337, 1997.

[47] E. Predazzi J. Nemchik, N. Nikolaev and B Zakharov. Colour Dipole Phenomenology of Diffractive Electroproduction of Light Vector Mesons at HERA. *Z. Phys.*, C75:71–87, 1997.

[48] The Particle Data Group (R.M.Barnett et. al.). Review of Particle Properties. *Phys. Rev. D*, 54:1, 1996.

[49] W.Koepf L.Frankfurt and M.Strikman. Hard Diffractive Electroproduction of Vector Mesons in QCD. *Phys. Rev. D*, 54:3194–3215, 1996.

[50] T. Ahmed et al. *DESY 93-177 Physics*, 1995.

[51] W.J. Willis and V. Radeka. *Nucl. Inst. and Meth.*, A120:21, 1974.

[52] B. Andrieu et al. *Nucl. Inst. and Meth*, A350:499, 1994.

[53] R. Martin. A Measurement of The Structure Function of the Proton, F_2 (x, Q^2) at Low Bjorken-x. *PhD Thesis*, Liverpool University, 1994.

[54] H. Bethe and W. Heitler. *Proc. Roy. Soc.*, A146:83, 1934.

[55] I. Abt et al. The H1 Detector at HERA. (Updated version). *Nucl. Instrum. Meth.*, A386:310, 1997.

[56] A. Mehta. Measurement of the Diffractive Proton Structure Function and Calibration of the Forward Muon Detector at H1. *PhD Thesis*, University of Manchester.

[57] C. Hoeger. Measurement for x, y, Q^2 in Neutral Current Events. *Proceedings of The HERA Workshop*, 1:43–56, 1991.

[58] F.James. MINUIT: Function Minimisation and Error Analysis. *CERN Program Library Long Writeup*, D506, 1994.

[59] W.Erdmann. Untersuchung der Nachweiswahrscheinlichkeiten und Messgenauigkeiten von Teilchenspuren in der zentralen Spurenkammer von h1. *Diploma thesis, University of Hamburg*, 1994.

[60] D. Aston et. al. Photoproduction of Rho and Omega on Hydrogen at Photon Energies of 20-GeV to 70-GeV. *Nucl. Phys. B*, 209:56, 1982.

[61] T. J. Killian et. al. Observation of Meson Resonances in Electroproduction. *Phys. Rev. D*, 21:3005, 1980.

[62] W. D. Shambroom et. al. Diffractive Production of Vector Mesons in Muon Proton Scattering at 150-GeV and 100-GeV. *Phys. Rev. D*, 26:1, 1982.

[63] M. G. Ryskin A. D. Martin and T. Teubner. Diffractive Electroproduction of Rho Meson Excitations. *Phys. Rev.*, D56:3007–3010, 1997.